ALMA MATER STUDIORUM · UNIVERSITÀ DI BOLOGNA

Scuola di Scienze

Corso di Laurea Magistrale in Fisica del Sistema Terra

On the Mediterranean Conveyor Belt System

Relatore:

Prof. Nadia Pinardi

Presentata da:

Federica Borile

Correlatore:

Prof. Paola Cessi

Sessione I

Anno Accademico 2015/2016

Learn from yesterday, live for today, hope for tomorrow,

the important thing is not to stop questioning.

Albert Einstein

Abstract

English version

The Mediterranean Sea is a semi-enclosed sea, connected to the Atlantic Ocean through the Gibraltar Strait and subdivided in two different regions by the Sicily Strait. The geographical extension of the basin, the surface heat flux, and the water inflow from the Gibraltar Strait are some of the basic factors determining its horizontal and vertical circulation.

The ocean circulation is forced by the combined effects of wind stress and buoyancy fluxes: in the Mediterranean Sea strong salinity and temperature zonal gradients contribute to maintain the zonal-vertical circulation, also called the zonal conveyor belt, while meridional-vertical cells, also called meridional overturning circulation (MOC), are equally forced by winds and deep water mass formation in three regions, the Gulf of Lyon, the southern Adriatic and the Cretan Sea areas.

The objective of this thesis is to study how these cells combine together to form the Mediterranean conveyor belt system. This has never been attempted before so the conclusions are necessarily preliminary.

The largest part of the thesis is devoted to the diagnostic study of the circulation from available data sets. Recently a long term reanalysis has become available from 1987 to 2013 and we have used to study the water mass structures first and the Mediterranean Conveyor Belt System.

In the first part we discuss the vertical zonal and meridional circulation by reconstructing the Wüst (1961) Mediterranean vertical salinity and temperature structures in an attempt to evaluate the water mass structure consistent with modern data. Our results confirm that Wüst depicted vertical circulation from scarce data is reproduced by the past 27 years observations.

The structure of both meridional and zonal circulations was discussed using velocity vertical streamfunctions with two different methods. The first one, so-called *eulerian*, allowed us to observe vertical structures that were already reported in the literature except for the Aegean and Western Mediterranean Sea which were mapped for the first time by this study. Recent studies in the Atlantic Ocean have shown that gyres and eddies have an important influence in the isopycnal vertical circulation.

This is called the *residual* circulation which was computed in this study for the first time.

A possible interpretation of horizontal connection between the meridional and zonal cells was discussed using horizontal streamfunction.

In the last part of the thesis we have been developing an idealized numerical model to study the vertical circulation in the Mediterranean Sea. We used the University of Bologna SURF model with the NEMO code and idealized coastline and surface forcing. At present we are running a test simulation considered as reference for future studies, where we will investigate the behavior of the Mediterranean vertical circulation.

Abstract
Italian version

Il Mar Mediterraneo è un bacino semi-chiuso, connesso all'Oceano Atlantico tramite lo stretto di Gibilterra e costituito al suo interno da due regioni comunicanti attraverso lo stretto di Sicilia. L'estensione geografica del bacino, il calore scambiato con l'atmosfera e il flusso d'acqua in ingresso allo stretto di Gibilterra sono alcuni dei fattori fondamentali che determinano la circolazione orizzontale e verticale al suo interno.

La circolazione oceanica è indotta dagli effetti combinati dello sforzo del vento e dai flussi di galleggiamento: nel Mar Mediterraneo intensi gradienti zonali di salinità e temperatura mantengono la circolazione verticale lungo la direzione zonale, anche chiamata *zonal conveyor belt*, mentre le celle meridionali, ovvero le *meridional overturning circulations* (MOC), sono forzate in egual misura dai venti e dalla formazione di acqua profonda in tre regioni, il Golfo di Lione, la regione meridionale del Mar Adriatico ed il Mar di Creta.

L'obiettivo di questa tesi è lo studio di suddette celle, indagando come esse interagiscono tra loro formando il sistema di trasporto di masse d'acqua che caratterizza il Mar Mediterraneo. Il fatto che ciò non sia stato mai studiato prima d'ora, rende le conclusioni necessariamente preliminari.

La maggior parte della tesi è dedicata allo studio diagnostico della circolazione a partire dai dati disponibili. Recentemente una rianalisi è stata prodotta in riferimento al periodo dal 1987 al 2013, ed è stata qui utilizzata per studiare in primo luogo le strutture delle masse d'acqua e poi il sistema di trasporto nel Mediterraneo (i.e. *Mediterranean Conveyor Belt System*).

Nella prima parte della tesi, la circolazione verticale in direzione zonale e meridionale viene discussa utilizzando le strutture di salinità e temperatura nel Mediterraneo pubblicate da Wüst (1961) al fine di valutare coerentemente tali strutture con i dati attualmente a disposizione. I nostri risultati confermano che la circolazione verticale ottenuta da Wüst per mezzo di dati scarsi viene riprodotta anche dalle osservazioni degli ultimi 27 anni.

La descrizione delle strutture di circolazione è stata effettuata attraverso un'analisi delle streamfunction verticali di velocità, ottenute seguendo due diversi metodi.

Il primo metodo, chiamato *euleriano*, ha permesso di osservare le celle di circolazione presentate in letteratura, ad eccezione delle immagini relative al Mediterraneo Occidentale ed al Mar Egeo che sono state sviluppate per la prima volta nel corso di questo studio. Il secondo metodo si basa su recenti studi effettuati nell'Oceano Atlantico, i quali hanno dimostrato la grande influenza di giri e vortici nel trasporto della proprietà di galleggiamento delle masse d'acqua; tale componente della circolazione è chiamata *residua*, ed è stata calcolata nel Mar Mediterraneo per la prima volta in questo studio.

Una possibile interpretazione della connessione orizzontale tra le celle meridionali e la cella zonale è stata qui proposta analizzando la streamfunction euleriana orizzontale.

Nell'ultima parte della tesi abbiamo sviluppato un modello numerico per studiare la circolazione verticale nel Mar Mediterraneo. E' stato adoperato il modello rilocabile SURF prodotto dall'Università di Bologna sulla base del codice NEMO, inserendo linee di costa idealizzate e forzanti superficiali climatologici. Attualmente stiamo eseguendo un esperimento di prova che sarà di riferimento per studi futuri, in cui si intende analizzare il comportamento della circolazione verticale nel Mar Mediterraneo.

Contents

CONTENTS

Chapter 1

Introduction

The Mediterranean Sea is a semienclosed basin connected to the global ocean through the narrow Strait of Gibraltar, which is 300 m deep. It is composed of two sub-basins of comparable size separated by the Strait of Sicily, which are the Eastern Mediterranean (EMED) and the Western Mediterranean (WMED).

The two sub-basins are characterized by similar large-scale dynamical features despite their different geographical arrangements: the WMED has a triangular shape, it is narrow on the west side (the Alboran Sea) and wide in the center, where the Sardinia and Corsica islands divide the Algerian basin from the Tyrrhenian Sea. The EMED has a complex geographical distribution: it is composed of two marginal seas in its northern part, the Adriatic and Aegean Seas, connected to the rest of the basin by shallow straits.

Every year the Mediterranean Sea loses buoyancy to the atmosphere through both an excessive evaporation over precipitation of about 0.7 m/yr and a negative heat budget of 7 W/m^2 (Garrett et al., 1993; Castellari et al., 1998). This steady-state balance is achieved at multidecadal time scales, while at seasonal and interannual time scalses heat can be stored and partially lost by single wintertime events.

The relationship between the surface buoyancy flux over the entire basin and the water flux exchange at the Strait of Gibraltar has been amply documented (Cessi and Pinardi, 2014). At the Gibraltar strait, water flows are separated vertically, with warmer and fresher (15°C and 36.2 psu) Atlantic Water entering the Mediterranean in the top layer, while colder and saltier waters (13.5°C and 38.4 psu) exit below (Lascaratos and Nittis, 1998). The outflowing water mass is composed of two water types: the Western Mediterranean Deep Water and the Levantine Intermediate Water (LIW) (Bryden and Stommel, 1982).

1.1   The Mediterranean Sea circulation

Despite its relatively small size, the Mediterranean Sea is governed by a large-scale circulation both in the horizontal and vertical directions, and it is driven by three major forcing interacting with each other (Pinardi and Navarra, 1993):

- the thermal and evaporative fluxes at the air-sea interface drive the overturning circulation and control water mass formation processes with variable timescales (between seasonal and decadal);

- the inflow-outflow transport at Gibraltar Strait is the mechanism controlling the overall basin water budget on decadal timescales;

- the wind stress forces the circulation at sub-basin spatial scales with a strong seasonal variability.

Thermal and wind effects might act on the same spatial scales, the former inducing water transformation processes and the latter causing the spreading of the newly-formed water mass (Pinardi and Navarra, 1993). Following both spreading and mixing of vertical processes, Wüst proposed (1961) four different core masses:

1. the near-surface water of Atlantic origin, between 0 and 75 m depth,

2. the intermediate water, between 200 and 600 m,

3. the deep water, between 1500 and 3000 m,

4. the bottom water, at depths to 4200 m.

Since the Strait of Sicily is only 300 m deep, down to this depth the Mediterranean circulation meanders over the entire basin, while deep motion is limited within the sub-basin where is has been forced.

Pinardi et al. (2015) analysed the horizontal circulation structures and proposed an exhaustive description of the Mediterranean dynamical pattern at the surface and between 200-300 m depth, shown in the following pages on Figure 1.1 and Table 1.1. Figure 1.1 demonstrates that time-mean circulation in the Mediterranean Sea is made up of both boundary and open ocean intensified jets at the border of cyclonic and anticyclonic gyres. The basin circulation has a double gyre structure due to the wind stress sign: the northern areas are characterized by cyclonic circulations, while the southern areas typically have anticyclonic motion. In addition, as for the North Atlantic case, deep and intermediate water formation processes contribute to force the cyclonic northern gyres, while the southern gyres store intermediate-mode waters which compose the permanent thermocline of the basin.
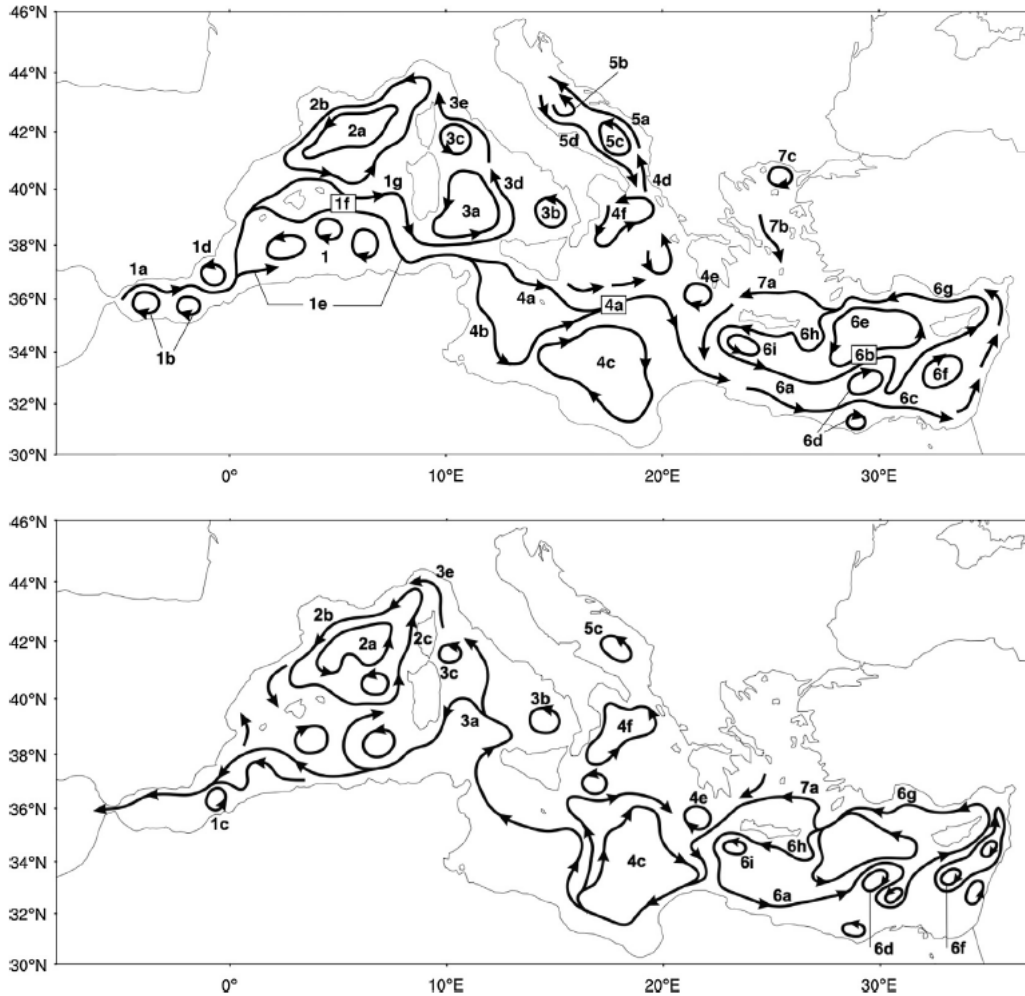
Figure 1.1: The schematic of the mean surface circulation structures as deduced from the 1987-2007 reanalysis mean flow field (labels explanation on Table 1.1). *Top figure:* surface circulation. *Bottom figure:* 200-300 m average circulation. Reproduced from Pinardi et al. (2015).

Hereafter we describe the main water masses paths in the surface and intermediate layers. The Atlantic Water Current characterizes the surface mean flow in the Mediterranean Sea, spreading eastward along the African coast as is modified by air-sea interactions. As a result, it becomes Modified Atlantic Water (MAW) which usually occupies the upper 100 m layer and is characterized by a higher salinity (38-38.3 psu) than Gibraltar inflow waters due to evaporation and mixing (Demirov and Pinardi, 2007). Numerical model simulations (Speich et al., 1996) and laboratory experiments (Gleizon et al., 1996) have demonstrated a conjunction of the Gibraltar Strait regime, the general pattern of the Atlantic Flow in the Alboran Sea, and the circulation of the underlying Mediterranean water.

On the other hand, intermediate waters are mainly Levantine Intermediate Water, which originates in the Levantine basin but can be found all around the Mediterranean Sea. Its large-scale distribution is described in Figure 1.2 (Pinardi and Masetti, 2000); several branchings currents spread LIW all around the basin, even though the main

pattern moves westward and northward. The most important paths bring the LIW to the northern Adriatic Sea and in the Gulf of Lyon, where it contributes to deep convection events, taking part in deep water formation processes.
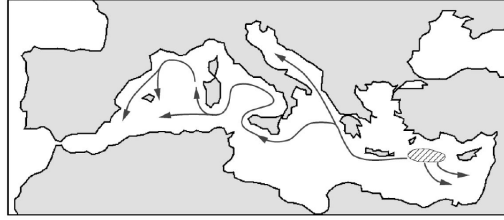

Figure 1.2: LIW dispersal pathways as synthetised from recent modeling and observational studies. Reproduced from Pinardi and Masetti (2000).

Currents systems	Components
System 1	1a: Atlantic Water Current
	1b: Western and Eastern Alboran Gyres
	1c: Almera-Oran front
	1d: Almera-Oran cyclonic eddy
	1e: Algerian Current segments
	1f: Western Mid-Mediterranean Current
	1g: Southern Sardinia Current
System 2	2a: Gulf of Lyon Gyre
	2b: Liguro-Provencal-Catalan Current
	2c: Western Corsica Current
System 3	3a: South-Western Tyrrhenian Gyre
	3b: South-Eastern Tyrrhenian Gyre
	3c: Northern Tyrrhenian Gyre
	3d: Middle Tyrrhenian Current
	3e: Eastern Corsica Current
System 4	4a: Atlantic-Ionian Stream
	4b: Sicily Strait Tunisian Current
	4c: Syrte Gyre
	4d: Eastern Ionian Current
	4e: Pelops Gyre
	4f: Northern IonianCyclonic Gyre
System 5	5a: Eastern South-Adriatic Current
	5b: Middle Adriatic Gyre
	5c: South Adriatic Gyre
	5d: Western Adriatic Coastal Current
System 6	6a: Cretan Passage Southern Current
	6b: Mid-Mediterranean Jet
	6c: Southern Levantine Current
	6d: Mersa Matruh Gyre System
	6e: Rhodes Gyre
	6f: Shikmona Gyre System
	6g: Asia Minor Current
	6h: Ierapetra Gyre
	6i: Western Cretan Cyclonic Gyre
System 7	7a: Cretan Sea Westward Current
	7b: Southward Cyclades Current
	7c: North Aegean Anticyclone

Table 1.1: Nomenclature for the surface and intermediate depth circulation structures described in Figure 1.1. Reproduced from Pinardi et al. (2015).

1.1.1 The Mediterranean circulation variability

Pinardi et al. (2015) stated that Mediterranean circulation time variability peaks at the seasonal and interannual time scales, as indicated by observations (Larnicol et al., 2002; Poulain et al., 2012) and numerical simulations (Demirov and Pinardi, 2002; Molcard et al., 2002).

Seasonal variability

According to Pinardi and Masetti (2000) the seasonal variability can be strictly related to changes in heat and momentum fluxes, as it involves mainly:

- the surface water mass formation cycle (Hecht et al., 1988),

- the seasonal reversal of currents in different portions of the basin (Tziperman and Malanotte-Rizzoli, 1991),

- the strength of mesoscale flow fields (Ayoub et al., 1998),

- the winter geographical location of deep and intermediate convection sites (Leaman and Schott, 1991; Artegiani et al., 1997).

Both surface water mass properties and large scale circulation are strongly related to the seasonal cycle amplitude in the external forcing of the circulation. Moreover the circulation climatological seasonal structure and the water masses properties can be justified by space and time arrangement of the meteorological forcing over the basin. The surface atmospheric flow field is characterized by two subregional wind regimes:

- winter Westerlies winds interact with the local orography,

- in summer there is a strong land-sea temperature contrast.

Nonetheless, wind stress curl, topography, and viscous boundary effects contribute equally to the potential vorticity balance (Pinardi and Navarra, 1993). Figure 1.3 shows a schematic of the wind-driven circulation in wintertime, simplifying the patterns of Figure 1.1. Notice the clear division of cyclonic gyres to the north and anticyclonic gyres to the south.

Interannual variability

The interannual variability of the basin can be analysed by investigating the main circulation patterns and the changes at 30 m depth, approximately at the bottom of the Ekman layer. The intermediate variability is punctuated by events mainly forced by winter atmospheric anomalies strong enough to shift the timing of the seasonal cycle (Korres et al., 2000).
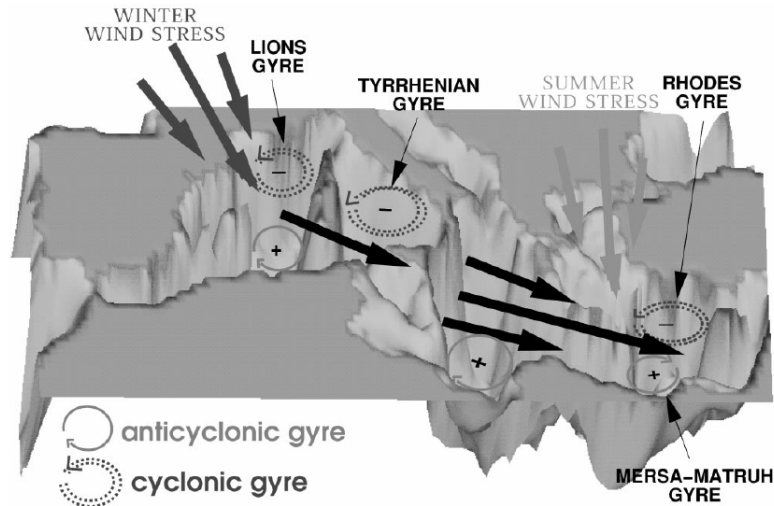
Figure 1.3: Schematic of the wind-driven circulation in wintertime conditions. The thick arrows indicate the direction of winter surface wind stress field. Sverdrup-induced wind-driven gyres are drawn, consistently with vorticity input from the two jets sides. Reproduced from Pinardi and Masetti (2000).

The largest changes happen in the Eastern Mediterranean, where the Northern Ionian Reversal phenomenon (NIR) has occurred as the largest decadal variability event in the past 20 years (Pinardi et al., 2015).

The atmospheric momentum and heat fluxes, as well as wind stress variance are found to be the main driving forces of interannual timescale circulation variability, which is larger in the Eastern than in the Western Mediterranean. Nevertheless interannual variability has a component which is related to the mesoscale field, too. In fact, various studies demonstrate that interannual variability aspects involve the following processes:

- intermediate and deep water mass formation rate (Nittis and Lascaratos, 1998),

- large variations in volume transport between basins at the Straits (Astraldi et al., 1995),

- sudden switches in the deep water mass formation areas for the EMED (Roether et al., 1996)

- changes in the flow direction in several regions (Hecht et al., 1988; Artale et al., 1994),

- abrupt changes in LIW characteristics (Hecht, 1992).

Relative to the seasonal case, interannual variabilities are more difficult to explain since several mechanisms may contribute, e.g. meteorological anomalies with immediate or delayed effects, and internal nonlinear ocean dynamics which introduce chaotic elements into the redistribution of water masses.

1.2   Water mass formation processes

The water mass formation events occur in a few selected regions, characterized by weak stratification and exposed, in winter, to intense buoyancy loss to the atmosphere. Under these conditions, a violent deep-reaching convection mixes surface waters to great depth, setting and maintaining the properties of the abyss.

In the global ocean case, convection in few sites feeds the thermohaline circulation, which is the circulation of the ocean responsible for roughly half of the poleward transport required by the atmosphere-ocean global system (Marshall and Schott, 1999). In the Mediterranean Sea, this type of formation gives rise to four overall important water masses, characterized by their reference depth and geographical location given by:

1. the Levantine Intermediate Water (LIW),

2. the Cretan Deep Water (CDW),

3. the Eastern Mediterranean Deep Water (EMDW),

4. the Western Mediterranean Deep Water (WMDW).

The correspondent formation areas are the Rhodes Gyre, the Aegean and Cretan seas, the Adriatic Sea, and the Gulf of Lyon, as shown in Figure 1.4.
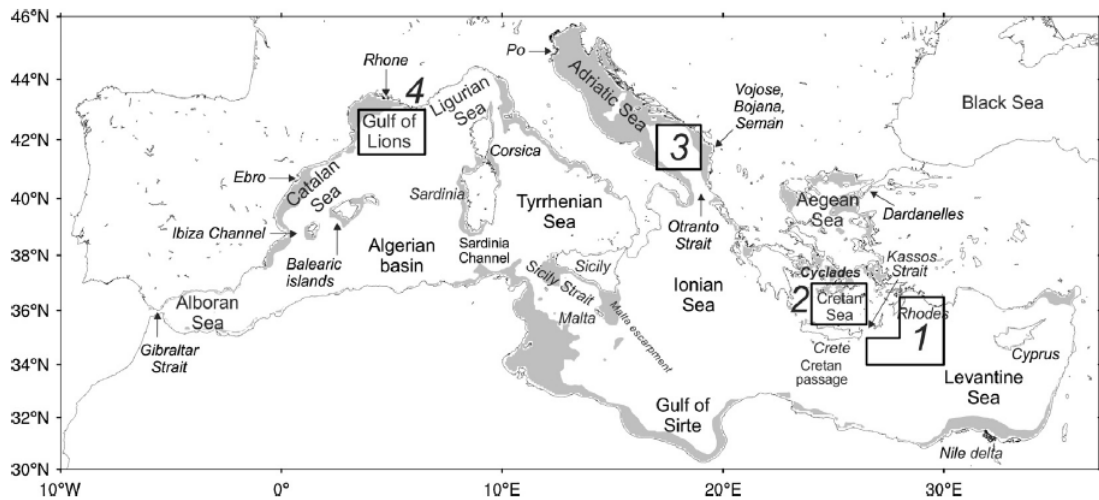

Figure 1.4: Mediterranean basin geometry and nomenclature for major seas and areas. The four boxes represent the regions of intermediate and deep water mass formation. Reproduced from Pinardi et al. (2015).

Pinardi et al. (2015) studied a reanalysis dataset from 1987 to 2007 in the Mediterranean area, finding that maxima water mass formation rates (hereafter defined in Sv) are always reached during February and March. They demonstrated that every year the formation rate changes according to different atmospheric conditions and water properties, and larger deep and intermediate events occur periodically, with

7

frequency of three to six years. The only exception was the CDW formation, which had maximum rate between 1991 and 1994, and then decayed (Figure 1.5).
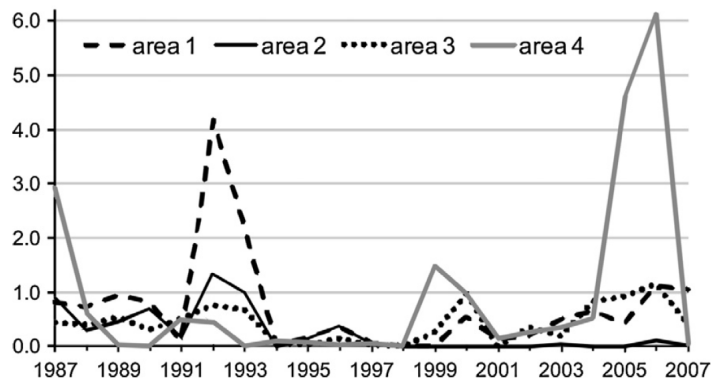

Figure 1.5: WMF rates (Sv) for the months of February and March and for the four regions indicated in Figure 1.4, as a function of time. Reproduced from Pinardi et al. (2015).

Although the Mediterranean has a limited extension, the deep and intermediate water mass formation events behave similarly to the global ocean case, enhancing the vertical circulation cells over the entire basin. Hereafter we summarize the principal information about the four open-ocean convection sites in the Mediterranean Sea, describing their spatial and temporal variability. More quantitative information will be discussed in chapter 3.

1.2.1 Western Mediterranean Deep Water formation

The most intensively studied site is the Gulf of Lyon in the northern WMED, where the Mediterranean Ocean Convection experiment (MEDOC) in 1970 observed a rapid (in a day or so) mixing of the water column down to 2000 m, as required for the WMDW formation. In the following years Stommel et al. (1971) measured the intensity of vertical currents associated with convective elements, of the order of 10 cm/s. Later the quantitative investigation of the Gulf of Lyon proceeded, and Schott and Leaman (1991) proposed the first acoustic doppler current profiler (ACDP) experiment, and found the existence of small-scale plumes during an intense cooling phase, fixing the horizontal dimension at just around 1 km.

Finally, recent studies about convective process and WMDW formation in this area identified three different phases (Figure 1.6, taken from Marshall and Schott (1999)):

- the *preconditioning* phase happens on the large-scale (order of 100 km) in the Gulf of Lyon when the stratification weakens but remains positive. A gyre-scale cyclonic circulation causes a clear isopycnal doming, bringing weakly stratified waters of the interior close to the surface. Such condition happens wintertime, as very weakly stratified waters mass beneath the surface are exposed directly to the surface forcing (Swallow and Caston, 1973);
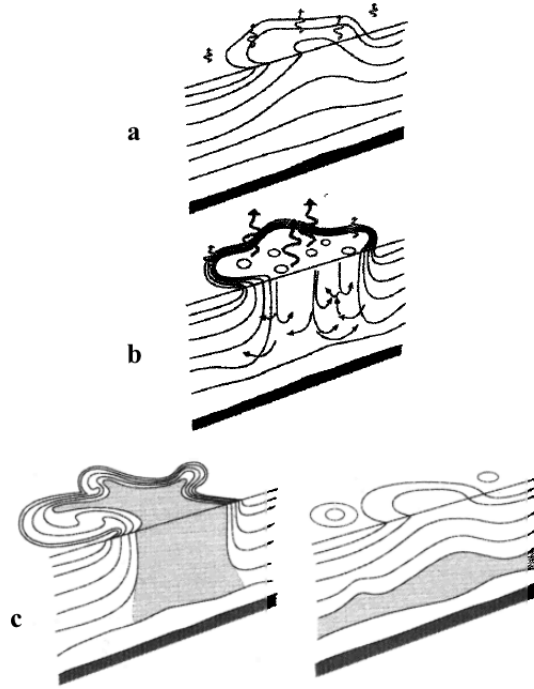
Figure 1.6: Schematic diagram of the three phases of open ocean deep convection: (a) preconditioning, (b) deep convection, and (c) lateral exchange and spreading. Buoyancy flux through the sea surface is represented by curly arrows, and the underlying stratification/outcrop is shown by continuous lines. The volume of fluid mixed by convection is shaded. Reproduced from Marshall and Schott (1999).

- the *deep convection* or *violent mixing* phase occurs when convection is observed in the centre of convective patch, leading to intense mixing and to a deepening of the mixed layer. Sinking occurs in plumes (on scale of the order of 1 km) in which the dense water sinks at vertical speed up to 10 cm/s (Schott and Leaman, 1991; Merckelbach et al., 2010);

- the *lateral exchange* or *sinking/spreading* phase occurs when the mixed water sinks and spreads horizontally. The spreading of dense water happens through the action of eddies of horizontal scale around 10 km, thought to be generated at the edge of the convective patch (Gascard, 1978; Testor and Gascard, 2006). This phase often occurs concurrently with the violent mixing phase, as demonstrated by Schott and Leaman (1991).

When the strong forcing ceases, vertical heat fluxes on convective scale trigger a horizontal transfer associated with eddies on geostrophic scale. Then, in the following weeks and months, this horizontal motion allows the reoccupation of the convection site by the stratified fluid of the periphery.

It has been demonstrated that the region of cyclonic circulation in the Gulf of Lyon, centered on the $\sigma_0 = 28.8 \, kg/m^3$ isopycnal dome, lies along the path of two cold and dry winter winds, namely the Tramontane and the Mistral (Marshall and Schott, 1999). The best geographical correspondence happens during the coldest

days of January, and the maximum erosion of buoyancy at the surface occurs at mid-February.

Legg and McWilliams (2001) showed that even in the case of horizontally homogeneous surface forcing the deep convection area tends to localize in areas with relatively small horizontal extensions in the central part of mesoscale vortices. Wu and Haines (1998) found that the LIW advection contributes to the salt budget of the newly formed deep waters.

1.2.2   Eastern Mediterranean Deep Water formation

Moving eastward, the second site of deep water formation is the Southern Adriatic Sea, where EMDW forms and spreads out into the Ionian Sea. Three factors define the necessary prerequisites to deep convection: the sub-basin scale cyclonic circulation, the presence of highly saline and dense water in the intermediate layer (due to LIW influence), and winter outbreaks of cold and dry continental air (Manca et al., 2002).

Dense water is formed in wintertime in the northern part of Adriatic Sea, so-called *shelf* water formation, and in the middle of the southern Adriatic (*open ocean* water formation). In winter, waters from the northern region of the basin move towards the southern Adriatic, where mixing with the incoming LIW take place and deep convection is induced (Castellari et al., 2000). Dense water so formed reaches values around 1029.20 kg/m^3, exits through the Otranto strait and flows along the western boundary of the Ionian basin (Artegiani et al., 1997).

EMDW thermohaline properties have changed over the last three decades mainly due to the effect of the so-called Eastern Mediterranean Transient (EMT) (Roether et al., 1996). During this climatological event, the main source of the EMDW switched from the Adriatic Sea to the Aegean Sea for the period of 1989-1995 (Klein et al., 1999, 2000; Manca et al., 2003). Starting from 1989, the advection of salty Levantine Surface Water (LSW) inside the Aegean Sea, combined with suitable atmospheric conditions, caused an intense deep water formation event and a consequent massive overflow of deep water, the CDW, from the Cretan Sea to the EMED (Gertman et al., 2006). The estimated rate of overflow was about 1.2 Sv, which is four times the estimated typical outflow from the Adriatic Sea (Roether et al., 1996; Lascaratos et al., 1999).

Theocharis et al. (1999) supposed that this intense deep water formation process has been forced by the increase of deep-water density ($\sigma_0 > 29.20$) in the southern Aegean and by the subsequent rise of the isopycnal surface 29.20 above the sill of the Cretan Arc straits. Other authors, instead, supposed that these waters had been formed in the northern Aegean, and the formation process could have been triggered by a combination of two factors: a dry and cold winter and a low water outflow from the Black Sea. Trying to summarize these opinions, Gertman et al. (2006) concluded that both phenomena lead to the intensification of the Aegean Sea conveyor belt, which was the process that had transformed the LSW ingressing into the Aegean

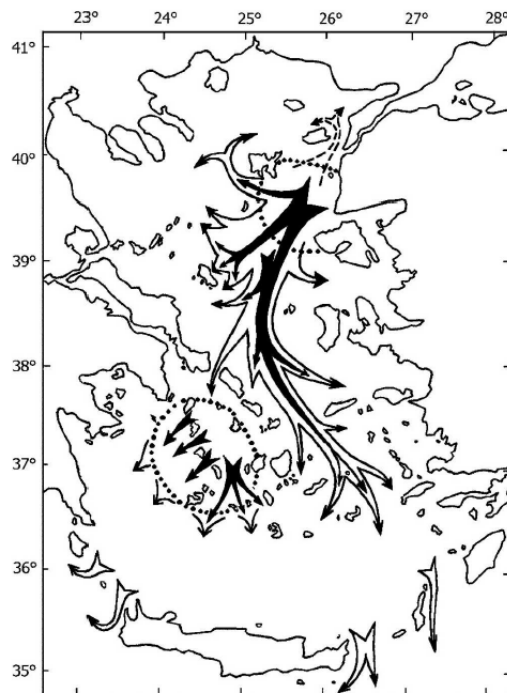Sea into an outflowing higher-density waters that spread into the deep layers of the EMED (Figure 1.7).

Figure 1.7: Regions of intermediate water and deep-water formation (dotted areas) and propagation pathways in the Aegean Sea. Reproduced from Gertman et al. (2006).

1.2.3 Eastern Mediterranean Intermediate Water formation

The last water formation site present in the Mediterranean is located in the Levantine Sea; in this area the convection event only reaches the intermediate layers, but has a duration of 2 months (February and March), and its estimated annual-average formation rate is 1.2 Sv (Lascaratos and Nittis, 1998). The newly formed water mass spreads over the entire Mediterranean basin and can be detected from salinity values around 39.1 psu between 200 m and 400 m (Lascaratos and Nittis, 1998). Various hypotheses have been presented in relation to the LIW formation mechanism and site: Ovchinnikov (1984) suggested that LIW forms at the center of the cyclonic Rhodes Gyre, since the cooling of the saline and cold center of the gyre increases the surface density and the water mass so formed sinks isopycnally to the periphery. Even if Ovchinnikov opinion is the most accreditate interpretation, others proposed a wider region of water-mass formation (for example Morcos (1972) Brenner et al. (1991)).

1.3 The Mediterranean Sea three-dimensional circulation

According to deep and intermediate water mass formation, the three-dimensional circulation in the Mediterranean Sea is organized as shown in Figure 1.8, taken from Pinardi and Masetti (2000).

Following the same distinction used in water mass formation processes, we define three major overturning circulation cells:

- an open zonal vertical circulation belt, which covers the entire extension of the basin and moves from surface to intermediate layers. Its manifestation on the surface is the eastward Atlantic Water (AW) motion, and the lower branch has LIW components. The main forcing factors are the Gibraltar fresh water inflow and the LIW formation in the Levantine Sea;

- a meridional overturning cell in the WMED, which is driven by the annual Gulf of Lyon deep convection. Its lower branch meanders southward to Algerian basin;

- a meridional overturning cell in the EMED, which is forced by deep water mass formation to the northern part of the sub-basin. Due to EMT climatical event, its main source area has changed during the last decades in connection with the deep water formation rate in the Adriatic and the Aegean Seas. Note that Figure 1.8 has been published in 2000, when the Aegean contribution to meridional overturning belt was still unclear; therefore Aegean water mass formation has not been shown.

Considering meridional overturning, the LIW presence in the three convection areas (Gulf of Lyon, Adriatic Sea and Aegean Sea) could control, or at least affect, the preconditioning phase of deep water formation events (Wu and Haines, 1996). Thus the LIW branching connects meridional and zonal conveyor belts, while Eastern and Western Mediterranean meridional overturning cells can interact, even if on long timescales (Pinardi and Masetti, 2000). Williams and Stratford (1998) suggested that the zonal cell has decadal timescales, while the meridional overturning cells could have a longer timescales, on the order of 50-80 years.

The overturning interannual variability in the Mediterranean Sea has been studied in theoretical, idealized as well as realistic modeling, but recent studies show that other sources could control internal variability. Although air-sea interaction remains the principal driving force in the Mediterranean circulation, purely oceanic processes might prove to be crucial in determining what equilibrium state will be reached by vertical circulation. This is the case of feedbacks between the rate of deep water formation and the strength of overturning circulation (Welander, 1982; Lenderink and Haarsma, 1994; Yin and Sarachik, 1995; Rahmstorf, 1996). An example is the
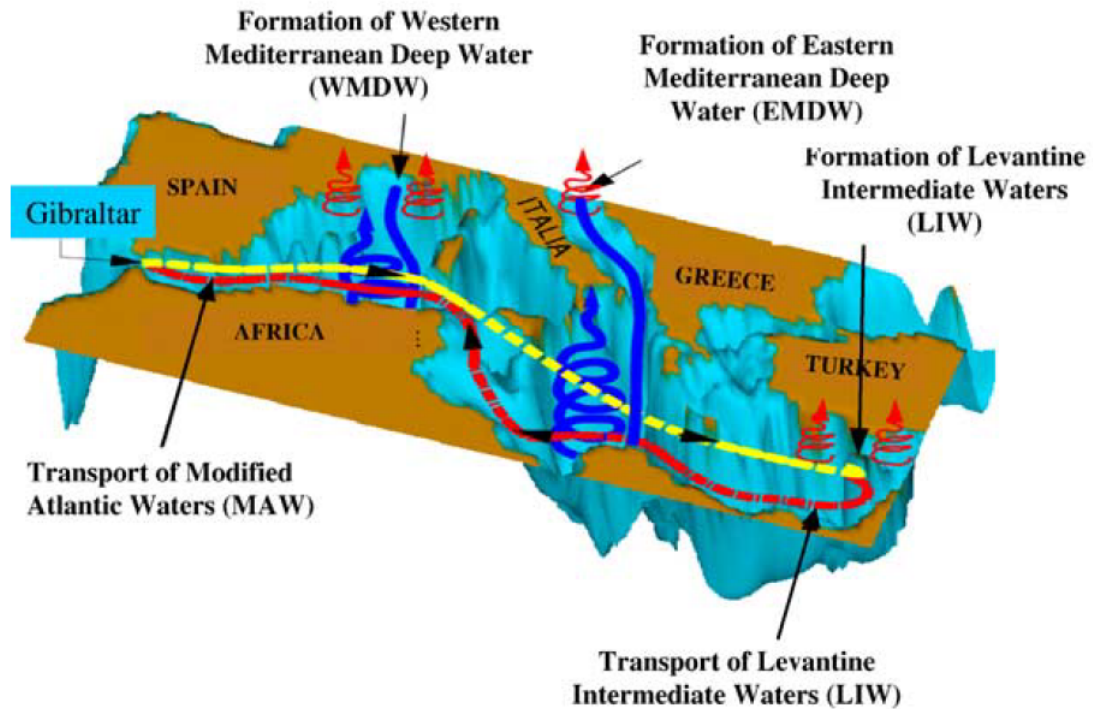
Figure 1.8: Scale of the basin-scale circulation in the Mediterranean Sea (after Pinardi and Masetti (2000)). The major conveyor belt systems is indicated by lines with different colour. Yellow colour indicates the AW stream which is the surface manifestation of Mediterranean zonal conveyor belt. Red colour indicates the mid-depth LIW recirculation branch of the thermohaline zonal circulation. Blue lines indicate the meridional cells induced by deep waters. LIW branching from the zonal conveyor belt connects meridional and zonal conveyor belts. Reproduced from Demirov and Pinardi (2007).

EMT event, which is related to an advection-convection feedback mechanism rather than to atmospheric causes (Pisacane et al., 2006).

Pisacane et al. (2006) found that the eastern basin is sensitive to switching from a restoring boundary condition on salinity to a freshwater flux. They ran two numerical experiments differing in the formulation of the surface boundary condition of salinity:

1. in Exp1 restoring boundary conditions were applied to both temperature and salinity,

2. in Exp2 the authors switched mixed surface boundary conditions, by prescribing the virtual Exp1 salt flux and maintaining the same momentum and heat fluxes as in Exp1.

They described the dynamic response to surface forcing of the two Mediterranean sub-basins, and demonstrated that both sub-basins exhibit a more pronounced variability when mixed boundary conditions are applied. In conclusion, a spectral analysis confirmed that the EMED oscillates between two different patterns (weakening/strengthening of thermohaline circulation), which could be qualitatively related to the density difference of water masses formed in the Adriatic and in the Aegean Seas.

1. Introduction

Amitai et al. (2016) found two steady states of Adriatic overturning circulation, with and without active source of deep water. They varied the model restoring temperature, and obtained the following three results:

- under present-day-like atmospheric conditions, the EMED overturning circulation in an ocean general circulation model has multiple equilibra. The meridional overturning circulation (MOC) is made up of two steady states: an active state of Adriatic Sea (dense water outflowing from Otranto Strait), and a passive state of Adriatic (entering waters are denser than the leaving ones). In particular, the passive Adriatic MOC state is a result of an initialized colder Aegean state that is kept forced by minor temperature anomaly over the Aegean;

- under present-day atmospheric conditions the EMED overturning circulation exhibits decadal variability and abrupt transients, similar to the ones reported by Pisacane et al. (2006);

- Adriatic and Aegean Seas are united by a close relationship: changes over one sea induce variations in the other as well due to a horizontal advection.

Last by not least, Amitai et al. (2016) pointed out that when none of the seas produce dense enough water, the Levantine basin deep layers are not ventilated and an *anoxic period* is enabled, meaning that these layers become depleted in oxygen and peculiar sedimentation occurs at the bottom (Rohling, 1996).

1.4   Thesis objectives

The aim of this thesis is to understand how meridional and zonal overturning circulations combine together to form the Mediterranean conveyor belt system. Our approach is a diagnostic study of the vertical circulation in the Mediterranean Sea according to the reanalysis dataset produced by the Copernicus Marine Environment Monitoring Service for the period from 1987 to 2013.

This study is innovative as the interpretation of horizontal connection between the vertical meridional and zonal cells has never been attempted before.

In the first part we discuss the water mass structures in the Mediterranean Sea, evaluating the correspondence of temperature and salinity vertical structures proposed by Wüst in 1961 with the ones obtained with modern data.

Velocity and density fields are used to evaluate both volume and buoyancy transport along the vertical meridional and zonal cells, focusing on regions where vertical cyclical forcing occurs, which are the Gulf of Lyon, the Adriatic, the Aegean and the Levantine Seas.

We illustrate the fundamental forcing which have driven overturning circulation during the considered period, specifying where eddy-induced velocity may contrast or reinforce the main water volume transport.

In the last part of this thesis we propose a framework setting for a future model analysis of the conveyor belt: we define both geographical structure of the domain and climatological boundary conditions which are necessary to reproduce the above mentioned vertical circulation over the whole basin.

1. Introduction

Chapter 2

Diagnostic studies of the water mass structures

The following chapter illustrates reanalysis is and how it can lead to a better understanding of ocean circulation. In the first section we focus on reanalysis description and we mention the data validation (Simoncelli et al., 2015). In the second section we calculate and discuss monthly climatologies of scalar fields.

2.1 Reanalysis dataset

Reanalysis is a 3D retrospective reconstruction of the ocean state obtained through a data assimilative numerical experiment. It improves on traditional analysis by integrating fields produced by a numerical model with observational data referred to a specific temporal and spatial domain. Therefore, the reanalysis method aims at merging together simulation and observations, using a data assimilation scheme, in order to provide an optimized ocean reconstruction in the period of interest. Reanalysis includes observations retrospectively and produces a homogeneous dataset on a uniform grid.

Several methods have been used to produce large-scale reanalysis, taking ocean observations either from satellite altimetry (Fu et al., 1994) or in situ data, but only a few reanalyses use both datasets until today (Stammer et al., 1991). An example is the CMCC Global Ocean Physical Reanalysis System (C-GLORS), which simulates circulation and tracers fields of the ocean in the last decades using by the ocean model NEMO, at 1/4° resolution with 50 vertical levels. A similar approach was used by Adani et al. (2011) to investigate the Mediterranean Sea area: this effort was challenging because observational datasets are scarcer at regional levels, and higher resolution models are required to represent the dynamics correctly.

In this thesis, we use the second reanalysis of the Mediterranean area produced by the Copernicus Marine Environment Monitoring Service (hereby named MED REA). This product provides daily mean fields over 27 years, from 1987 to 2013.

Although MED REA and C-GLORS have in common the same NEMO model and OceanVar assimilation scheme, they differ in the spatial domain: the first focuses on the Mediterranean basin while the second considers the entire global ocean. With a view to refining the final product quality, great improvements on reanalysis applications have been done especially on oceanographic studies of long-term variability phenomena and of climate change.

In the following subsections we analyze the reanalysis product, focusing on model setting, data assimilation scheme and quality control. We mainly reference to MED REA manual for users and to NEMO manual.

2.1.1 Model system description

NEMO-OPA code (Nucleus for European Modelling of the Ocean-Ocean Parallelise) is the ocean general circulation model used by Mediterranean reanalysis. In particular, NEMO 3.2 is an hydrodynamic model which describes the ocean using spherical coordinates. It solves the Navier-Stokes in the primitive equations approximation along with a nonlinear equation of state which couples the two active tracers (temperature and salinity) to the momentum and mass-conservation. The vector invariant form of the primitive equations is:

$$\frac{\partial \mathbf{U}_h}{\partial t} = -\left[(\nabla \times \mathbf{U})] \times \mathbf{U} + \frac{1}{2}\nabla(\mathbf{U}^2) \right]_u - f\mathbf{k} \times \mathbf{U}_h - \frac{1}{\rho_0}\nabla_h p + \mathbf{D^U} + \mathbf{F^U} \,, \quad (2.1)$$

$$\frac{\partial p}{\partial z} = -\rho g \,, \quad (2.2)$$

$$\nabla \cdot \mathbf{U} = 0 \,, \quad (2.3)$$

$$\frac{\partial T}{\partial t} = -\nabla \cdot (T\,\mathbf{U}) + D^T + F^T \,, \quad (2.4)$$

$$\frac{\partial S}{\partial t} = -\nabla \cdot (S\,\mathbf{U}) + D^S + F^S \,, \quad (2.5)$$

$$\rho = \rho\,(T, S, p) \,, \quad (2.6)$$

where $\mathbf{U} = (u, v, w)$ is the three-dimensional velocity field, $\mathbf{U_h}$ is the horizontal velocity field, T, S, p are the in situ temperature, salinity and pressure respectively, $f = 2\mathbf{\Omega} \cdot \mathbf{k}$ is the Coriolis parameter, $\mathbf{\Omega}$ is the Earth angular velocity and g the gravitational acceleration. $\mathbf{D^U}$, D^T and D^S are terms parametrising small-scale processes for momentum, temperature and salinity, and $\mathbf{F^U}$, F^T and F^S are surface forcing terms. The fundamental assumptions that underpin (2.2) through (2.6) can be summarized as follows:

1. **the Boussinesq hypothesis** assumes that the influence of density variations is confined to the buoyancy force on the right side of (2.2);

2. **the hydrostatic hypothesis** assumes that in vertical momentum equation the vertical pressure gradient balances with the buoyancy force;

3. **the spherical earth approximation** allows gravity to be parallel to the Earth radius;

4. **the thin-shell approximation** assumes that the ocean depth is negligible compared to the Earth radius;

5. **the turbulent closure hypothesis** parametrises turbulent fluxes in terms of the largescale features.

The horizontal grid has a resolution of $1/16° \times 1/16°$, describing an *eddy-permitting* model, while the vertical grid has 72 unevenly spaced vertical levels from the surface to a maximum depth of 5000 m. Using *partial cell parameterization*, the thickness of the bottom layer is allowed to vary as a function of geographical location to yield a better representation of bathymetry. NEMO model arranges the spatial distribution of variables using the Akarawa C-type grid (Mesinger and Arakawa, 1976) which defines scalar quantities at the center of each grid volume, and shifts vectorial fields by half a grid width in the three directions so that they are defined at the edges of the grid volumes (Figure 2.1).
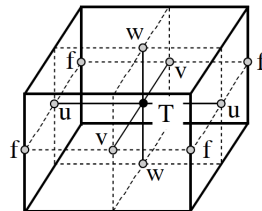

Figure 2.1: Arrangement of variables using Akarawa C-type grid. T indicates scalar points where scalar quantities (temperature, salinity, pressure, density and horizontal divergence) are defined. (u,v,w) indicates vector points, and f indicates vorticity points where both relative and planetary vorticities are defined. Reproduced from NEMO manual v.3.4.

The model domain covers the entire Mediterranean Sea and a portion of the Atlantic Ocean in order to better resolve salinity and heat exchanges through the Gibraltar Strait. In particular, the geographical location is from 18.125°W to 36.25°E in longitude and 30.1875°N to 45.9375°N in latitude. Nevertheless, in the following chapters we do not discuss the ocean box in order to focus on the Mediterranean Sea from the Gibraltar Strait to its eastern side (Figure 2.2).

Figure 2.2 presents six vertical transects along the Mediterranean Sea useful to explain the vertical structure across the basin of scalar fields:

- meridional transects along 5.5°E, 19°E and 28°E;

- zonal transects along 35°N anf 40°N;

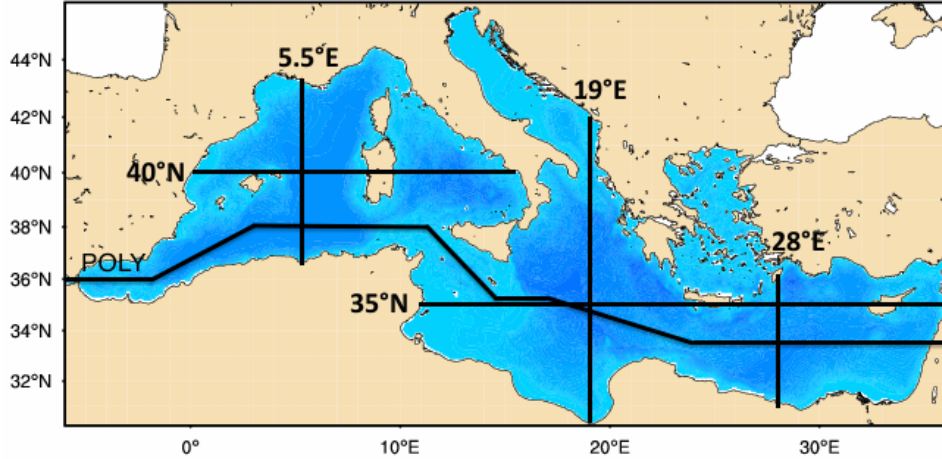- polyline transect in zonal direction along the whole basin.

Figure 2.2: Map of the reanlysis domain we focus on, vertical transects described hereafter are shown. Spatial extension from 6°W to 36.25°E in longitude and 30.1875°N to 45.9375°N in latitude.

NEMO encloses the Atlantic box into a frame of land points and imposes no-slip condition on horizontal solid boundaries of the entire domain. Vertical boundaries, instead, require different expressions depending on the type of interface involved. At the bottom, $(z = -\mathbf{H})$, vertical and horizontal velocity expressions are summarize in (2.7) and (2.8), whereas heat and salinity fluxes are negligible:

$$w\Big|_{z=-H} = -\mathbf{u}_h^b \cdot \nabla \mathbf{H}, \tag{2.7}$$

$$A^{vm}\frac{\partial \mathbf{u}_h}{\partial z}\Big|_{z=-H} = C_D\sqrt{u_b^2 + v_b^2 + e_b}\mathbf{u}_h^b, \tag{2.8}$$

$$A^{vT}\frac{\partial T}{\partial z}\Big|_{z=-H} = 0, \tag{2.9}$$

$$A^{vS}\frac{\partial S}{\partial z}\Big|_{z=-H} = 0, \tag{2.10}$$

where $\mathbf{u}_h^b$ is the latitudinal and zonal component of the bottom velocity, C_D is the drag coefficient, e_b is the bottom kinetic energy resulting from processes of short temporal and spatial scales, A^{vm} is the vertical eddy viscosity, and A^{vT} A^{vS} are the vertical diffusivity coefficients.

Many factors contribute to define vertical boundary conditions at the surface $(z = \eta)$, as both heat and fresh water fluxes need to be involved. As for the bottom case, the equations can be summarized as follow:

$$w\Big|_{z=0} = -\frac{D\eta}{Dt} - WF, \tag{2.11}$$

$$A^{vm}\frac{\partial \mathbf{u}_h}{\partial z}\Big|_{z=0} = \frac{\tau}{\rho_0}, \tag{2.12}$$

$$A^{vT} \frac{\partial T}{\partial z}\Big|_{z=0} = \frac{Q_c}{\rho_0 \, C_p} \,, \tag{2.13}$$

$$A^{vS} \frac{\partial S}{\partial z}\Big|_{z=0} = WF \, S_{z=0} \, \rho_0 \,, \tag{2.14}$$

where τ is the wind stress, ρ_0 is the reference density, C_p is the specific heat capacity, WF is the imposed water flux and Q_c is the corrected heat flux.

The model is forced by momentum, heat, and water fluxes interactively computed using ERAInterim reanalysis fields (Dee et al., 2011) from the European Centre for Medium-Range Weather Forecasts (ECMWF). The two WF and Q_c variables are here parametrized as:

$$Q_c = Q_0 + \frac{DQ}{Dt}(T_m - T_0) \,, \tag{2.15}$$

$$WF = E - P - R/A \,. \tag{2.16}$$

In heat flux formula (2.15) Q_0 is the mean heat exchanged with the atmosphere, DQ/Dt the relaxation term equal to $-60 \, W/m^2 K$, T_m is the model Sea Surface Temperature (SST) and T_0 is the satellite SST. The water flux formula (2.16) includes the evaporation E, the precipitation P and the river runoff per unit of cell area R/A.

The model provides, as outputs, daily and monthly mean fields of 9 variables: salinity, potential temperature, sea surface height, zonal and meridional currents, wind stress, heat flux, water flux and shortwave radiation.

2.1.2 Data assimilation scheme

MED REA data assimilation system is a three-dimensional variational method developed by Dobricic and Pinardi (2008), which integrates in-situ observations along with altimetry data. The background error correlation matrix used is estimated from an historical model simulation and varies seasonally in 13 regions of the Mediterranean Sea each having different characteristics (Dobricic et al., 2005). Then, by this scheme the system evaluates for each model variable the minimum value of a cost function, using an iterative method (Adani et al., 2011), and assimilating the data of:

- **in situ temperature and salinity profiles**. These are available from the historical data archive of MedAtlas with information coming from different instrumental data type (CTD sensors, XBTs, mechanical bathythermographs, bottles, and ARGO floats);

- **satellite Sea Level Anomaly (SLA) from altimetry**, as maps containing time series interpolated on the model grid.

SST satellite data are not directly assimilated by the system but they are used for iteratively correcting the heat flux at air-sea interface as in (2.15).

Finally, MED REA is initialized by temperature and salinity monthly climatological fields. Such fields have been produced from a dataset of historical in situ data

collected from 1900 to the beginning of the reanalysis. This information is applied from January 1st 1985, the first day of model run onwards. The following two years of integration are considered as the spin-up period for the model, and are not used.

2.1.3 Data quality control

The validation scheme for MED REA consist of a defined sequence of diagnostic controls agreed by all global and regional reanalysis producers. This procedure studies the entire period spanned by reanalysis from 1987 to 2013 and, in particular, it defines estimate accuracy numbers BIAS and RMSE for the following variables:

- Sea Surface Temperature,

- water column Temperature,

- water column Salinity,

- Sae Level Anomaly.

Table 2.1 summarizes the skill of each parameter. For the first parameter the verification compares daily reanalysis SST maps with daily satellite maps, and the result is used to correct the surface heat flux formula (2.15). Elsewhere, MED REA statistical computation uses the following misfits, m, for the T, S and SLA parameters (Adani et al., 2011; Tonani et al., 2009):

$$m \equiv [y_0 - H(x)] , \qquad (2.17)$$

where y_0 is the observation, H is the linearized observational operator, and x is the model solution. Misfits are computed for the background model fields before the data assimilation, and background fields are considered unaffected by correlation between previous observations, due to data distances both in time and space.

Parameter	BIAS	RMSE
SST $[°C]$	0.19 $\pm$0.26	0.56 $\pm$0.14
T $[°C]$	-0.02 $\pm$0.05	0.35 $\pm$0.02
S $[psu]$	-0.01 $\pm$0.05	0.10 $\pm$0.02
SLA $[cm]$	0.10 $\pm$0.13	3.48 $\pm$0.54

Table 2.1: Summary of MED REA skill, Estimate Accuracy Numbers for different parameters computed on the entire basin over the entire time period (1987-2013). Taken from MED REA Quality Information Document.

In the following, we describe the differences of results between model and observation data. For temperature and salinity case, monthly mean BIAS and RMSE are computed separately over five layers up to 1000 m in order to uncover possibly different behaviors, while layers deeper than 1000 m have been neglected because the lack of data does not allow any meaningful comparison.

Sea Surface Temperature. Figure 2.3 shows differences between monthly estimates computed by reanalysis and satellite data. MED REA reproduces well observed maps, even if we recognize the largest errors along coastlines due to problems of atmospheric forcing resolution and coastal processes reconstruction.

Daily statistics over the entire basin are illustrated on Figure 2.4. Oscillations of mean values reflect the seasonal variability of temperature, which reaches the top in spring-summertime and the minimum in wintertime. In summertime the BIAS is always positive, meaning that reanalysis data at the surface are warmer than observations.
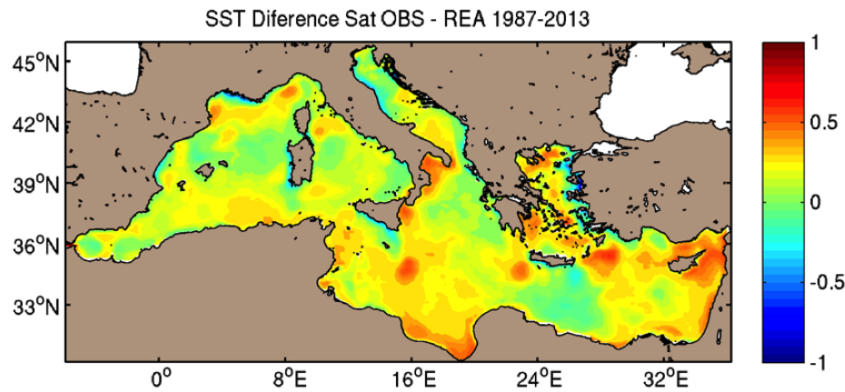
Figure 2.3: Maps of long-term annual mean of difference between MED REA *SST* and *SST* reference data set. Taken from MED REA Quality Information Document.
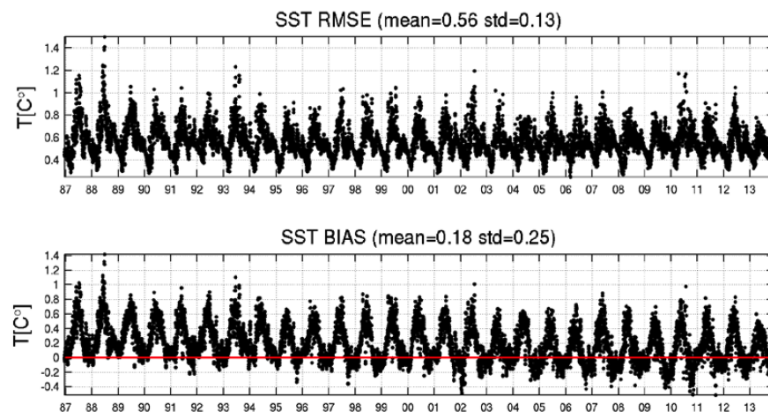

Figure 2.4: *SST* RMSE (*top*) and BIAS (*bottom*) computed from MED REA and the satellite reference *SST* on a daily basis. Taken from MED REA Quality Information Document.

Water column Temperature. In temperature validation five vertical layers are compared with 1900-2009 climatological data. As in *SST* case, the greatest differences occur near coastal boundaries, where climatologies are not able to reproduce short-lived events, e.g. one day, changing with depth. In particular, the upper layers are influenced by atmospheric forcing that varies seasonally, whereas the lower layers show a slowly and smooth variation during the reanalysis time period. Table 2.2 summarizes BIAS and RMSE values referred to each layer.

23

Temperature [$°C$]	BIAS	RMSE
0 - 30 m	0.01 ±0.29	0.66 ±0.36
30 - 150 m	0.05 ±0.17	0.48 ±0.20
150 - 300 m	0.05 ±0.09	0.23 ±0.08
300 - 600 m	0.07 ±0.08	0.17 ±0.06
600 - 1000 m	0.08 ±0.08	0.13 ±0.05
Total	-0.02 ±0.05	0.35 ±0.02

Table 2.2: Temperature estimate accuracy numbers computed for different vertical layers and total. Total BIAS and RMSE were computed over the whole domain (up to 1000m of depth) over the entire time period. Taken from MED REA Quality information document.

Water column Salinity. Five layers are considered for the annual mean of MED REA salinity field, and their results are compared with 1900-2009 climatology field. The largest differences appear at the surface near rivers runoff and in deep layers near straits. Positive BIAS values down to 300 m (Table 2.3) show that this reanalysis dataset is saltier than observed data climatology, with anomalies increasing with depth up to 0.1 psu at 1000 m.

Salinity [psu]	BIAS	RMSE
0 - 30 m	-0.02 ±0.09	0.20 ±0.10
30 - 150 m	-0.04 ±0.05	0.12 ±0.05
150 - 300 m	-0.01 ±0.02	0.06 ±0.02
300 - 600 m	0.01 ±0.02	0.04 ±0.02
600 - 1000 m	0.03 ±0.03	0.05 ±0.02
Total	-0.01 ±0.05	0.10 ±0.02

Table 2.3: Salinity estimate accuracy numbers computed in different vertical layers and total. Total BIAS and RMSE were computed over the whole domain (up to 1000m of depth) over the entire time period. Taken from MED REA Quality information document.

2.2 Salinity

In this section we consider space and time variability of reanalysis salinity field.

Salinity gives the total amount of dissolved solids in seawater, and it is measured using conductivity instruments. Its units are given in *practical salinity units (psu)* using an opportune table of conversion from conductivity measures. Its vertical distribution contributes to the seasonal variability of water stratification: between the surface and 150 m depth, diffusive and turbulent processes maintain the thermocline salinity gradient, while in deep layers salinity values is homogeneous in time and space.

In order to describe the climatological distribution of salinity data we use (2.2) where S_m is the monthly average of fields during the reanalysis period, and τ_m is the total number of days occurred in the chosen month.

Thus we have:

$$S_m(\overrightarrow{x}) = \frac{1}{\tau_m} \int_0^{\tau_m} S(\overrightarrow{x}, t)\, dt\,. \tag{2.18}$$

The horizontal distribution of salinity near the surface is controlled by heat and fresh-water fluxes at the interface with the atmosphere (2.15) and (2.16), whereas interior water columns behave differently as their structure depends on intermediate depth currents. A key role in salinity distribution is played by an *antiestuarine* (anticyclonic) circulation cell which moves along the whole basin extension. It is forced by a two-layer exchange of water flux through the Strait of Gibraltar, where in the upper layer slightly saline Atlantic Water enters and moves through the Strait of Sicily into the EMED, while in the lower layer more saline waters flows out of the Mediterranean. Flowing along the upper branch, this Atlantic Water (AW) is exposed to evaporation and mixing with the underlying waters, causing a progressive growth of salinity (Zavatarelli and Mellor, 1995); in fact, the surface value increases from 36.4 psu in the Gibraltar area to 37.6 psu in the Strait of Sicily and to values higher than 38.6 psu in the Levantine Sea (Figure 2.5).

Here, during winter, the synergic effect of low temperatures and high salinities induces convection processes that allow surface water to sink down and to form Levantine Intermediate Water (LIW) (Pisacane et al., 2006). These processes occur in the Rhodes-Cyprus area, and probably in other sectors of the Levantine Sea (Morcos, 1972). Then, the LIW circulates across the EMED and the WMED before reaching the Atlantic Ocean through the lower layer of the Gibraltar Strait. The salinity value of outflowing fluxes is less than 37.5 psu but higher than than surface values. Many observations have analyzed this two-layer-flow structure across the Gibraltar Strait: the presence of fresh and superficial water inflows and salty deep water outflows can be considered as a crucial demonstration of the antiestuarine cell.

In 1961 for the first time Wüst used salinity, oxygen and temperature distributions to study the mean steady state of the deep circulation for the whole Mediterranean. Using the *"core method"* he was able to follow the vertical spreading and mixing of main water masses, by following the intermediate maxima and minima positions of the scalars previously mentioned. His results were in the form of handmade figures that have been considered until today a reliable qualitative representation of the Mediterranean circulation. In particular, some of these figures show longitudinal sections of salinity, and they are comparable to the ones we obtain today using climatological reanalysis data (upper panels of Figures 2.6 and 2.7). Looking at the new and the old images, first we notice the same vertical structure with strong gradient up to 300 m both in winter and summer sections, and then we recognize a zonal variability between the WMED and the EMED sub-basins along the entire water column. The Eastern Mediterranean contains saltier water respect to the Western part since evaporation processes are more efficient. Moreover, the majority of salty deep waters remain in the
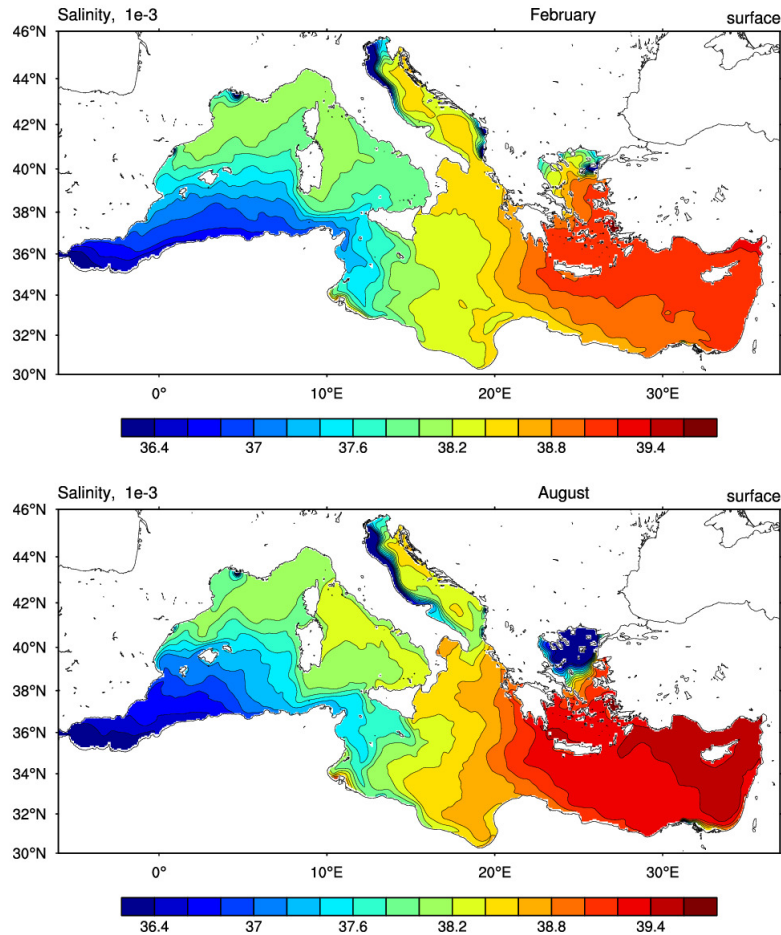
Figure 2.5: Map of surface salinity from reanalysis data, February and August are taken as the most representative month of winter period (*top*) and summer period (*bottom*) respectively. River run-off effect is evident near the outlet of Rhone and Po rivers, and near the Dardanelli Strait.

Levantine Sea because of the Sicily Sill is only 300 m depth. Nevertheless a narrow strip of salty water flows over the Sicily Sill and enters in the WMED at intermediate depths reaching different longitudes depending on seasons. This intrusion is visible both on Wüst and reanalysis sections, and quoting Wüst: "the near surface Atlantic undercurrent to the east and the Levantine intermediate current to the west represent the most important branches of the Mediterranean deep circulation".

Looking at the reanalysis section (lower panels of Figures 2.6 and 2.7), the contour line referred to 38.54 psu represents the Levantine intrusion spreading inside the WMED more evident in wintertime (until 0°E) than during summer (3°E). Analogous features are visible in Wüst section if we consider 38.5 psu contour lines; recalling that Wüst section are based on observational data, this difference of 0.1 psu agrees with BIAS values we mentioned in the previous section and confirms that reanalysis dataset is saltier than observations.
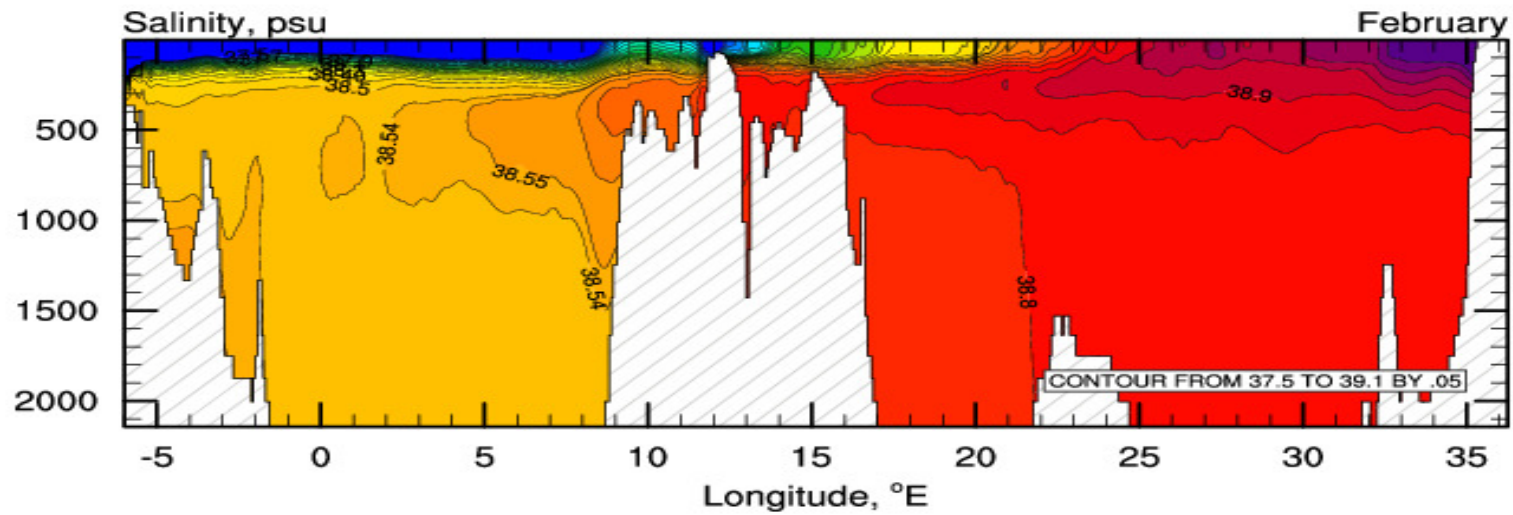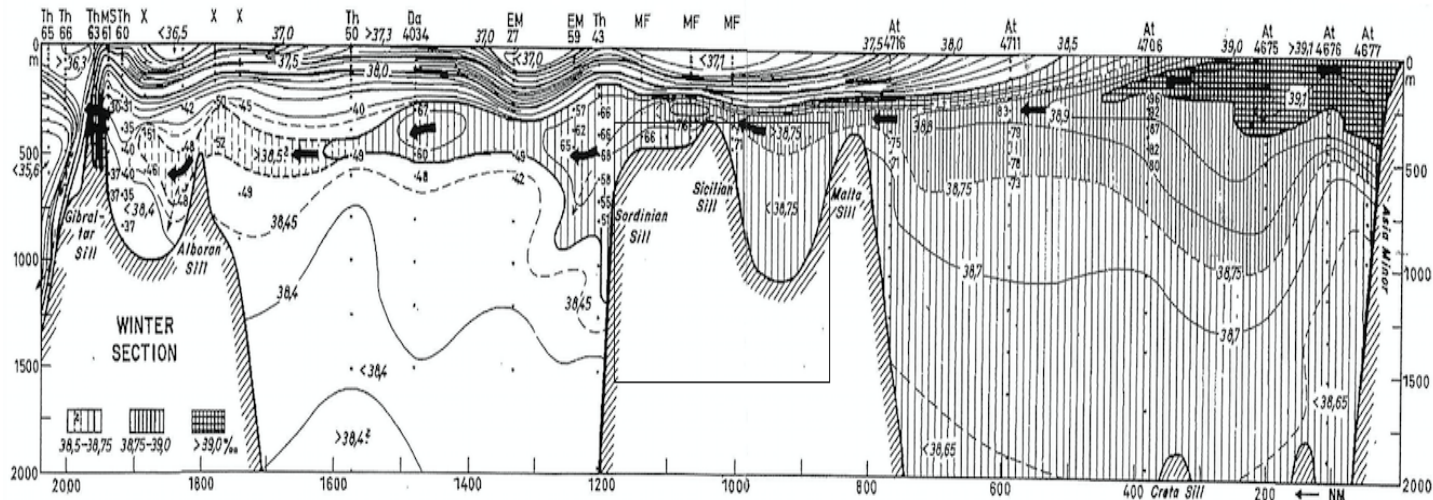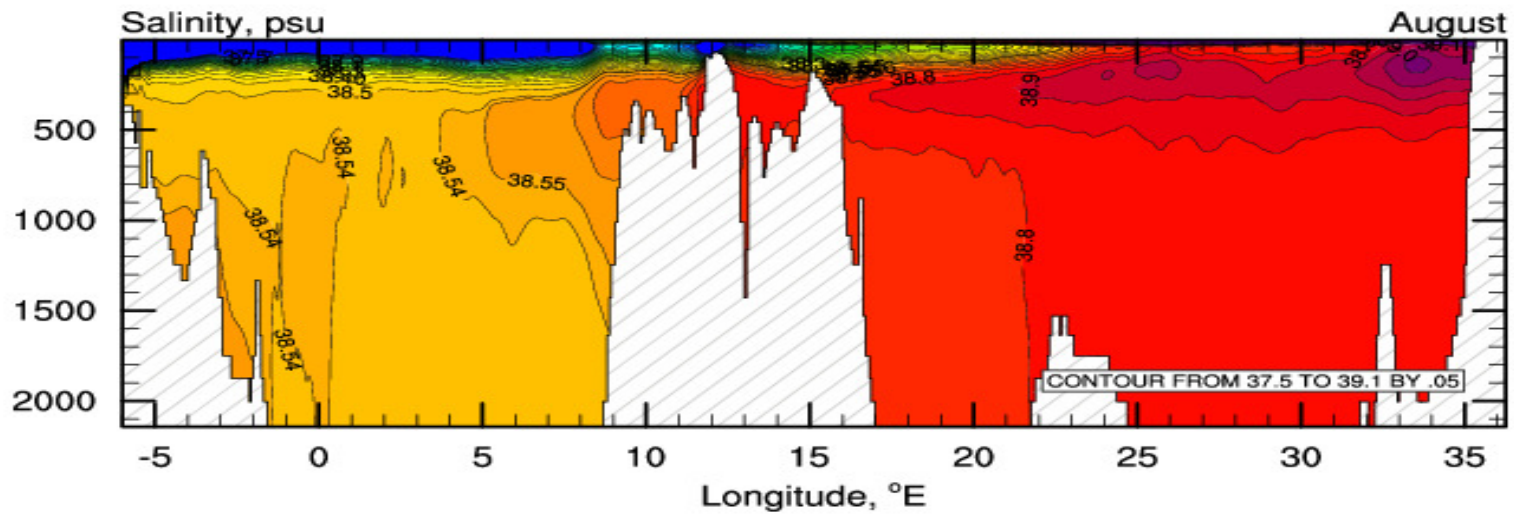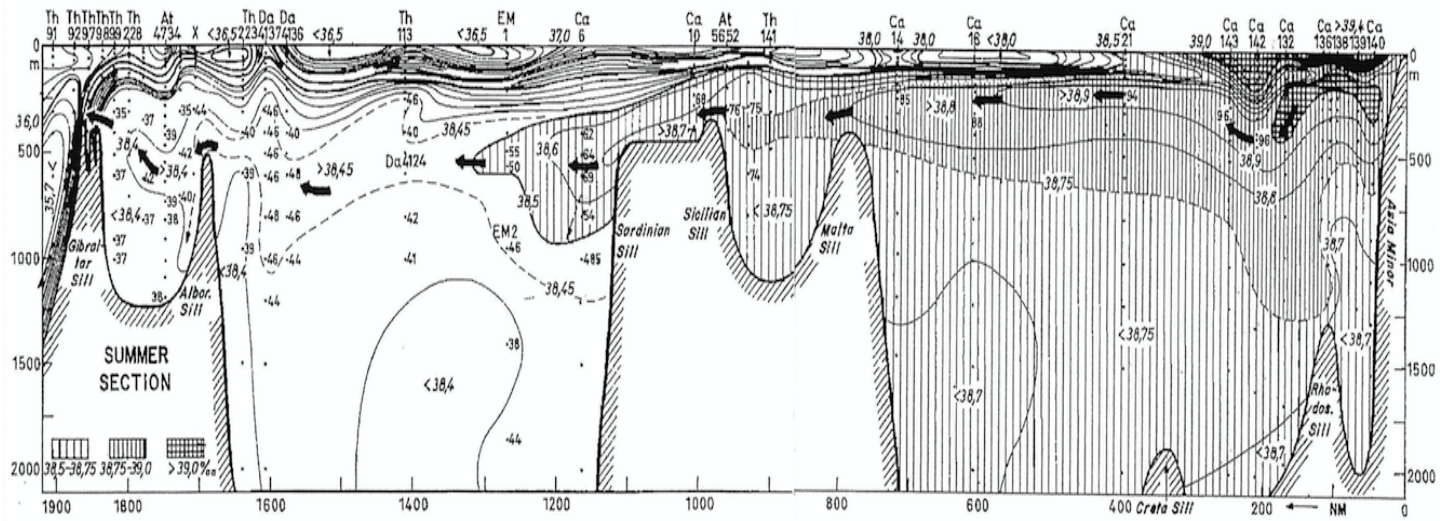
Figure 2.6: (*top*) Longitudinal section of salinity along the axis of the Levantine intermediate current for winter season. Reproduced from Wüst (1961). (*bottom*) Polyline longitudinal section of salinity from reanalysis climatology of February. The location of polyline is shown in Figure 2.2.

Figure 2.7: (*top*) Longitudinal section of salinity along the axis of the Levantine intermediate current for summer season. Reproduced from Wüst (1961). (*bottom*) Polyline longitudinal section of salinity from reanalysis climatology of August. The location of polyline is shown in Figure 2.2.

2.3 Potential temperature

In this section we consider space and time variability of potential temperature θ, defined as the temperature that a water sample would attain if raised adiabatically to the sea surface. Recalling the Boussinesq approximation, this type of data differs from in situ temperature because the hydrostatic pressure heating effect is neglected. As for salinity, we analyze potential temperature distribution using monthly averages of daily fields, T_m, defined as:

$$T_m(\overrightarrow{x}) = \frac{1}{\tau_m} \int_0^{\tau_m} T(\overrightarrow{x}, t) \, dt \,. \tag{2.19}$$

Temperature distribution at the surface (Figure 2.8) is influenced by a negative annual-average heat budget of about $7W/m^2$ (Castellari et al., 1998), as well as by air-sea temperature difference and wind intensity. These effects determine seasonal and spatial changes in surface potential temperature, which varies from $13°C$ to $18°C$ in February, and from $21°C$ to $29.5°C$ in August. Vertical profiles show strong gradient in the thermocline and low variability in deep and cooler layers.
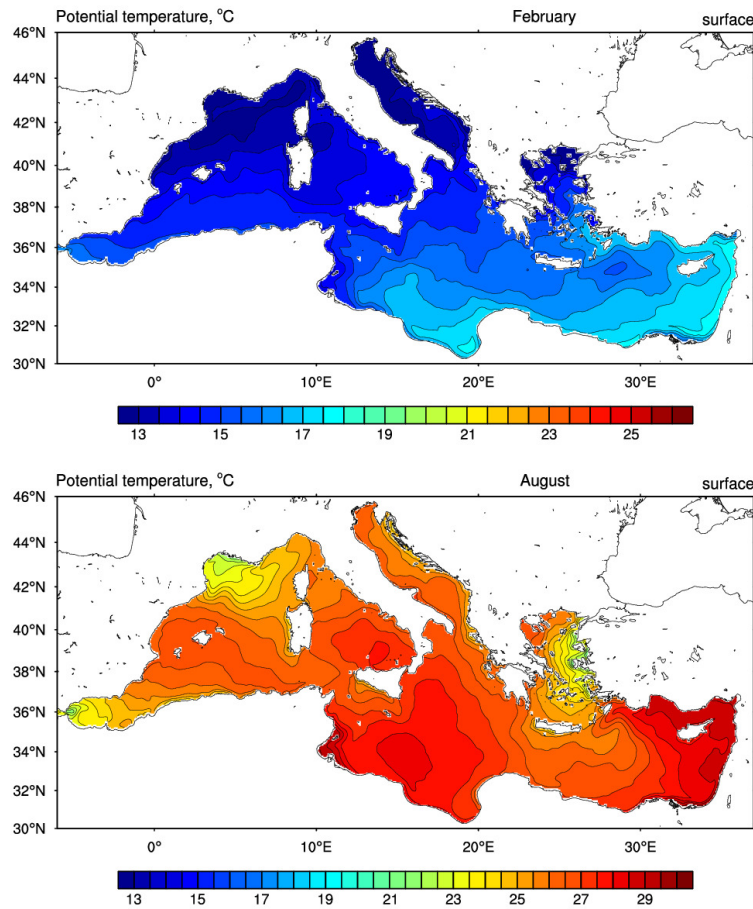

Figure 2.8: Map of surface potential temperature from reanalysis data, February and August are taken as the most representative months of winter period (*top*) and summer period (*bottom*) respectively.

2.4 Density

When a parcel of seawater is forced by different pressure gradients moving around the ocean, its in situ density changes continually because of the compressibility of seawater. Defining the in situ density, ρ, as the water mass quantity contained in a defined volume unit, ρ is described by a nonlinear function of temperature, salinity and pressure.

Although in model simulations surfaces of equal density (*isopycnals*) often coincide with isothermals, the international equation of state is defined by the Joint Panel on Oceanographic Tables and Standards which quotes the corresponding equation published by Millero and Poisson in 1981. The in situ density, ρ, is given by the polynomial function of pressure, p, in situ temperature, T, and practical salinity S:

$$\rho = \rho_0 \left[1 - \alpha(T - T_0) + \beta(S - S_0) \right] . \tag{2.20}$$

The definition of thermal expansion, α, and saline contraction, β, involves density gradients with respect to potential temperature θ and salinity S at constant θ and p, respectively. Thus, for this calculation to be done numerically, a conversion between θ and the input data T is necessary. Jackett and Mc Dougall (1996) have proposed an alternative seawater equation of state in terms of potential temperature, therefore improving its computational efficiency, given by

$$\rho(S, \theta, p) = \frac{\rho(S, \theta, 0)}{1 - p/K(S, \theta, p)} . \tag{2.21}$$

Here $\rho(S, \theta, 0)$ is a 15-term equation in powers of S and θ, with coefficients related to α and β in (2.20), while $K(S, \theta, p)$ the secant bulk modulus, is a 26-term equation in powers of S, θ and p, the coefficients being determined as in the Appendix A.

Potential density

In order to better reproduce ocean dynamics and to reduce the variation of density, Wüst (1933) and Montgomery (1938) defined a new variable, *potential density σ*, which is the density that a fluid would have if it were moved isoentropically and adiabatically to an arbitrary chosen, but fixed, reference pressure (McDougall, 1987). In literature we have found three different reference values namely 0, 2000, 4000 db: the first value represents sea surface pressure, while the second and third ones refer to deep ocean pressure measures below 2000 m and 4000 m .

Because the reanalysis outputs potential temperature, we use (2.21) as written in NEMO code to define potential density field referred to the surface pressure, σ_0, in the Mediterranean Sea.

Considering that Mediterranean depths are rarely deeper than 3000 m, we imposed the pressure $p = 0$ as a reference value; therefore we removed the pressure effect on

saline concentration coefficient, and we fixed $\rho_0 = 1.028 \, kg/m^3$ as reference density value. Finally, in order to have climatological monthly data, we applied (2.21) to θ and S daily fields, and then averaged the results over the entire time period, to obtain the monthly average $\sigma_{0,m}$ defined as

$$\sigma_{0,m}\left(\overrightarrow{x}\right) = \frac{1}{\tau_m} \int_0^{\tau_m} \rho(S, \theta, 0, \overrightarrow{x}, t) \, dt \, . \tag{2.22}$$
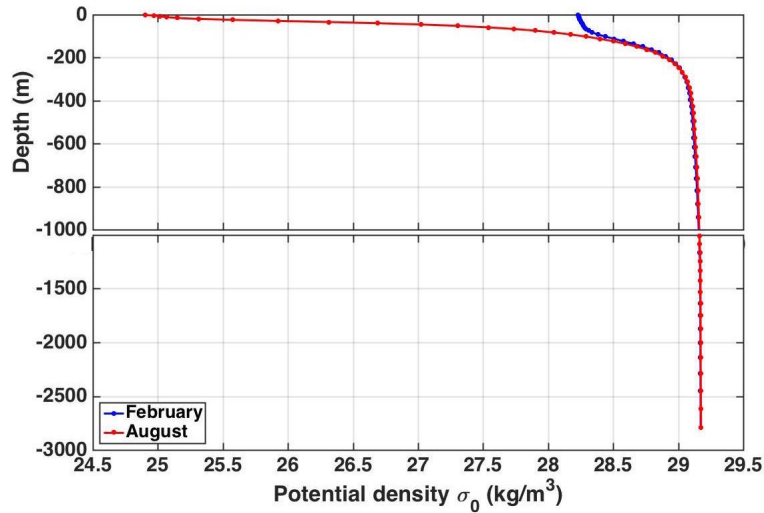
Figure 2.9: Potential density profile at longitude $6°$E and latitude $40°$N. The shape varies seasonally depending on density variability in the upper layer, which reaches its maximum during summer (August, *red line*) and its minimum during winter (February, *blue line*).

Figure 2.9, shows the seasonal variation of the vertical profile of potential density from the surface to 200 m depth. Summer climatological data show water column stratification, due to the negative heat flux at surface over the entire basin with maximum values around 180 W/m^2 that improves water column stability (Cessi and Pinardi, 2014). During winter potential density profile changes, and its vertical distribution can be divided in three regions:

1. the upper part, with low variability because of mixed layer processes;

2. the intermediate region from 50 m to 250 m, characterized by a well defined gradient of density (thermocline layer), which slowly decreases until 1000 m;

3. deeper layers with potential density greater than 29.15 kg/m^3.

Figure 2.9 describes a typical vertical profile, but during the coldest days of the year, in some regions this feature changes: the thermocline becomes thinner and isopycnal surfaces denser than 28.8 kg/m^3 reach the air-sea interface surface (*outcrop* events). Typically this phenomenon occurs in February when sea water is cooler, otherwise in the following months these surfaces restore to their typical depth allowing deep water mass formation.

In the following, we discuss wintertime plots in order to focus on water mass formation events.

Meridional transects in Figure 2.10 show the *outcrops* during February in the WMED, Adriatic Sea and Levantine Sea. Every plot defines a particular isopycnal that rises up to the top in the northern part of the section, even if it is deeper than 200 m in the southern part. Values of potential density outcrop are higher in the Levantine than in the WMED and the Adriatic Sea, 29.0 kg/m^3 and 28.8 kg/m^3 respectively.

Zonal transects in Figure 2.11 define a fundamental difference between the WMED and the EMED: in the first image, deep isopycnals lay under 150 m and intermediate isopycnals reach the surface only near Sardinia and Spain east coasts, while in the latter one, 29.0 kg/m^3 outcrops in a wide area between Cretan and Cyprus islands. This observation demonstrates that the WMED is not involved in the deep zonal circulation directly driven by water mass formation, while the EMED is. In particular, the geographical location of the Levantine $28.7 kg/m^3$ isopycnal outcrop in Figure 2.11 is different from the bottom plot of Figure 2.10, meaning that every year a large area of the Levantine Sea is involved in this phenomenon.

The polyline transect (Figure 2.12) shows potential density changes from the EMED to the WMED. In the Alboran Sea's upper layers the contour colour is saturated under 27.3 kg/m^3 to represent fresh water flowing from the Atlantic Ocean, while bottom layer in the Levantine Sea contains water heavier than 29.2 kg/m^3.

Comparing this transect with the ones presented in Figure 2.6 and 2.7 illustrates how salinity information is crucial to reproduce density distribution in the Mediterranean Sea.
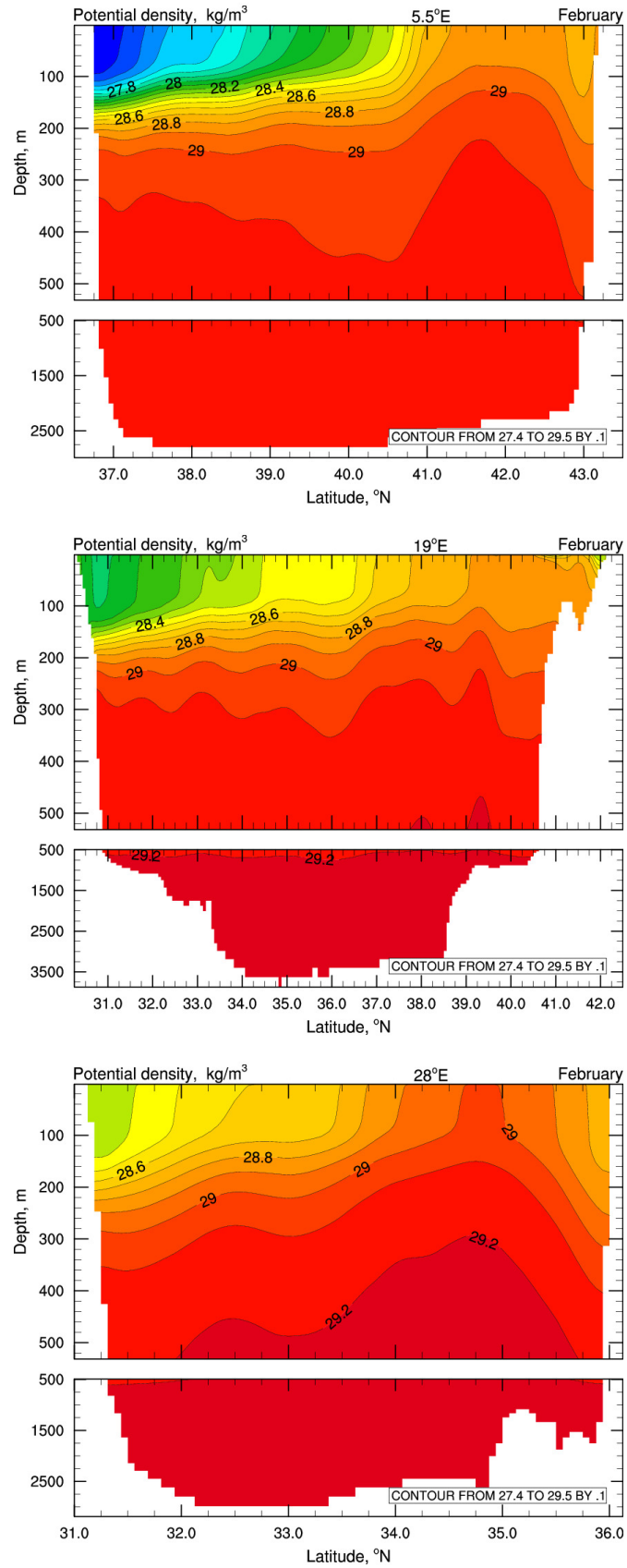
Figure 2.10: Meridional sections of potential density during climatological February along 5.5°E (*top*), 19°E (*centre*) and 28°E (*bottom*).
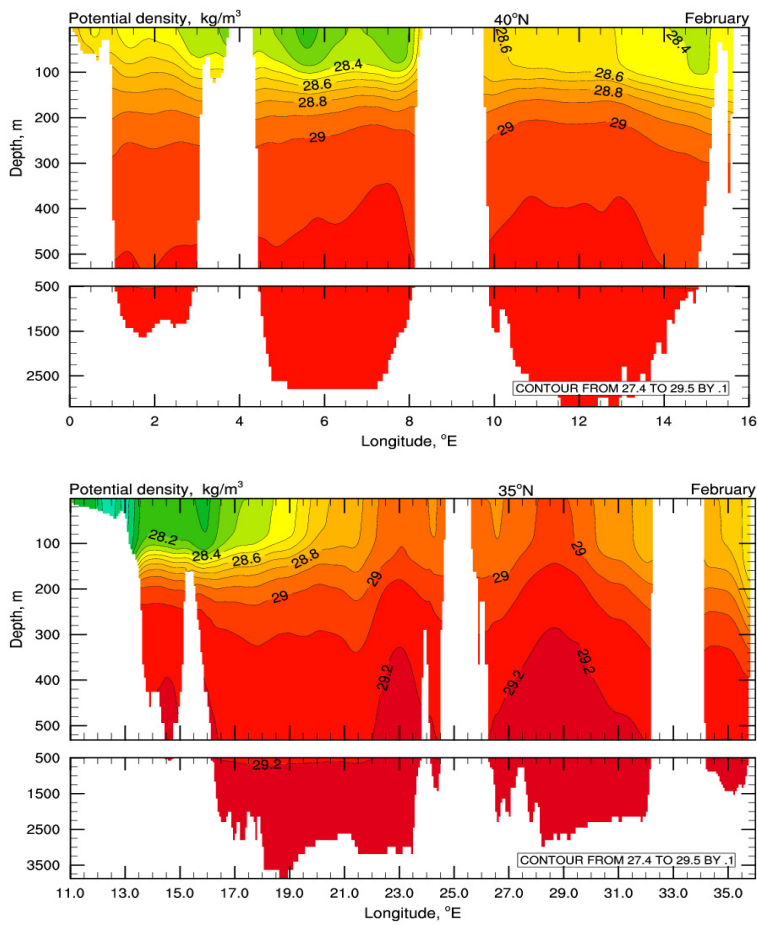
Figure 2.11: Zonal sections of potential density during climatological February along the WMED at 40°N (*top*), and the EMED at 35°N (*bottom*).
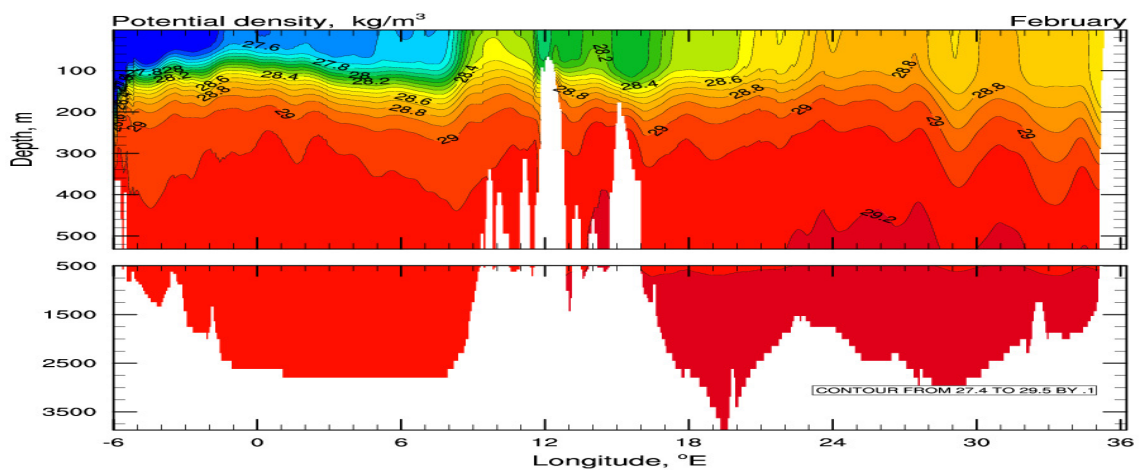

Figure 2.12: Polyline longitudinal section of potential density in climatological February average. West of longitude 6°E, Atlantic fresher water enters in the Mediterranean Sea, while east of longitude 20°E deep isopycnals rise to the surface in the Levantine Sea.

Chapter 3

Diagnostic studies of the Mediterranean Conveyor Belt System

Water properties inside a specific volume change in time according to different physical phenomena. Near-surface thermodynamics and biochemical variables are controlled by heat fluxes as well as diffusion processes, though if we look at the whole water column, the main contribution to properties modification comes from water transport. This chapter aims at analyzing the regions which are most affected by water transport processes across the Mediterranean, through to velocity streamfunctions in the vertical plane. We assume that the Mediterranean circulation forms a unique conveyor belt moving along longitudinal and latitudinal directions, similarly to the global ocean case. Therefore we analyze the regions of connection between zonal and meridional transports. This system conveys large amounts of water, heat, salt, carbon, nutrients and other tracers around the entire basin, and connects the sea surface and atmosphere with the reservoir of the deep sea. Furthermore the Mediterranean has a specific controlling mechanism that is the Gibraltar heat and water inflow/outflow system that maintains the circulation and its energy in a quasi-steady state.

Vertical circulation elements are cyclonic and anticyclonic cells combined together in a complex arrangement controlled by bathymetry, internal dynamical processes and multiple driving forces. The latter ones can be represented by four main factors:

- Gibraltar heat and water inflow that is in a net positive contribution for the Mediterranean Sea and that regulates the entrance/exit of the zonal conveyor belt;

- wind stress, which forces water motion up to 100 m (depending on the stress intensity) and provides upwelling or downwelling according to Ekman theory;

- eddies drift, which transport water masses across frontal structures along their pathway;

- deep water mass formation and buoyancy fluxes.

Hereafter we neglect the direct response to wind forcing, and we focus on the vertical circulation present in the intermediate and deep layers.

As for eddy-fluxes, they are included in the oceanic model because NEMO resolution of 1/16° covers distances of about 6 km at mid latitudes, i.e. the reanalysis is in the *eddy-permitting* regime. This assumption underpins the entire work, since dynamical structures at this scale are supposed to be very energetics and important (Demirov and Pinardi, 2007).

Besides eddies fluxes, in order to define the complete dynamic environment involved in the Mediterranean, we have to consider boundary currents, jets, meanders, permanent and recurrent subbasin-scale cyclonic and anticyclonic gyres. The way these structures interact together is still a complex topic, whereas the key issue is to identify which driving forces mainly control their motion.

Considering the system peculiarities described above, the present study has included two different methods to discuss the overturning circulation in the Mediterranean Sea: the first one, so-called *eulerian*, in the Eulerian frame, i.e. at a fixed point in space, allowed us to observe structures that were already reported in the literature, while the second, called *residual*, considers the eddies and gyres influence in the isopycnal vertical circulation. Recent studies in the Atlantic Ocean have shown the importance of such component, and the *residual circulation* is computed in this study for the first time on the Mediterranean basin.

3.1 Eulerian streamfunction

The first method used for studying the overturning circulation considers velocity fields as described in the model reference system, where the vertical dimension is depth; therefore, water circulation is depicted in terms of *volume transport*. This type of transport is considered as a measure of water motion. The eulerian computation integrates the continuity equation (2.3) along the appropriate directions,

$$\int_{y_{B1}}^{y_{B2}} \frac{\partial}{\partial x} u(x,y,z,t) \, dy = -\int_{y_{B1}}^{y_{B2}} \frac{\partial}{\partial z} w(x,y,z,t) \, dy \, , \qquad (3.1)$$

$$\int_{x_{B1}}^{x_{B2}} \frac{\partial}{\partial y} v(x,y,z,t) \, dx = -\int_{x_{B1}}^{x_{B2}} \frac{\partial}{\partial z} w(x,y,z,t) \, dx \, , \qquad (3.2)$$

where y_{B1} and y_{B2} are meridional boundaries, while x_{B1} and x_{B2} zonal boundaries.

To obtain meridional and zonal streamfunctions we integrate in the vertical direction and average over the reanalysis period, so the resulting formulas are:

$$\psi_{zon}(x,z) = -\frac{1}{T} \int_{t_0}^{t_1} \int_{-H}^{z} \int_{y_{B1}}^{y_{B2}} u(x,y,\tilde{z},t) \, dy \, d\tilde{z} \, dt \, , \qquad (3.3)$$

$$\psi_{mer}(y,z) = -\frac{1}{T}\int_{t_0}^{t_1}\int_{-H}^{z}\int_{x_{B1}}^{x_{B2}} v(x,y,\tilde{z},t)\, dx\, d\tilde{z}\, dt\,, \tag{3.4}$$

where $T = t_1 - t_2$ is the temporal interval, and H the bathymetry.

The volume transport thus obtained is tangent to streamfunction isolines and its intensity increases according to streamfunction gradient; negative values represent a region of cyclonic circulation, while positive values define anticyclonic motions.

Equations 3.3 and 3.4 provide just a partial representation of water transport because they neglect all dynamical processes which have zero average along one spatial direction. As consequence, volume transport ignores contributions due to eddies, gyres and some baroclinic structures.

3.2 Residual streamfunction

Previous studies of the global ocean circulation demonstrate that mesoscales eddies mostly flux buoyancy and passive scalars along (but not through) mean buoyancy surfaces. Thus, eddy transport of buoyancy can be represented by a velocity function (Wolfe and Cessi, 2010). So far, as we know, no one has published quantitative analysis of the eddy-induced circulation in the Mediterranean Sea: this study aims at filling this gap by quantifying the significance of eddy fluxes in the Mediterranean conveyor belt.

The buoyancy force b depends on gravity acceleration and density, and its expression is given by

$$b = -g\frac{\rho - \rho_0}{\rho_0}\,, \tag{3.5}$$

denser fluid parcel has a less buoyancy than a lighter one. In order to quantify zonal and meridional vertical transport along the buoyancy surfaces, we have to remap horizontal velocities, defined in the model on a finite volume grid, into a different co-ordinate system. Since buoyancy is usually gravitationally stable, it is monotonic in the vertical direction, hence suitable as an alternative vertical coordinate. Assuming that gravity acceleration is constant (the *thin-shell* approximation), buoyancy properties are analyzed through potential density (σ). Assuming stability of the density field with a monotonic increase from the top to the bottom, we interpolate the σ vertical coordinate to the z coordinate and vice versa. This mapping defines for each σ a correspondent depth value $\zeta(\sigma)$ (details are available in the Appendix B).

The following equations represent the overturning streamfunctions, ψ^*, using the new coordinate:

$$\psi^*_{zon}(x,\sigma) = -\frac{1}{T}\int_{t_0}^{t_1}\int_{\sigma_H}^{\sigma}\int_{y_{B1}}^{y_{B2}} u^*(x,y,\tilde{\sigma},t)\, dy\, d\tilde{\sigma}\, dt\,, \tag{3.6}$$

$$\psi^*_{mer}(y,\sigma) = -\frac{1}{T}\int_{t_0}^{t_1}\int_{\sigma_H}^{\sigma}\int_{x_{B1}}^{x_{B2}} v^*(x,y,\tilde{\sigma},t)\, dx\, d\tilde{\sigma}\, dt\,, \tag{3.7}$$

where u^* and v^* are velocity components along isopycnals, and σ_H is the bottom potential density. The alternative vertical coordinate is chosen to have 200 evenly spaced layers from a minimum value of $27.0\,kg/m^3$ at the top of the water column to a maximum of $\sigma = 29.9\,kg/m^3$ at the bottom.

In the level (z) coordinate system, (3.6) and (3.7) can be written as:

$$\psi^*_{zon}(x,\sigma) = -\frac{1}{T}\int_{t_0}^{t_1}\int_{-H}^{\zeta(\sigma)}\int_{y_{B1}}^{y_{B2}}\frac{d\sigma}{d\tilde{z}}\,u(x,y,\tilde{z},t)\,dy\,d\tilde{z}\,dt\,,$$

$$\psi^*_{mer}(y,\sigma) = -\frac{1}{T}\int_{t_0}^{t_1}\int_{-H}^{\zeta(\sigma)}\int_{x_{B1}}^{x_{B2}}\frac{d\sigma}{d\tilde{z}}\,v(x,y,\tilde{z},t)\,dx\,d\tilde{z}\,dt\,.$$

Unlike the mean flow described by (3.3) and (3.4), the flow described by ψ^* is not constrained by geostrophy, and therefore it contains the transport contribution also from structure which has meridional (and zonal) zero average. The sum of mean and eddy-induced velocities gives the so-called *residual* velocity (Wolfe and Cessi, 2010); the *residual* streamfunction, ψ^*, defines the buoyancy transport across the Mediterranean, and it can be considered representative of tracers transport. Each tracer has its own equation, which differs from the bathymetry balance, so the residual transport of tracers might differ in detail.

In conclusion, eddy flow is fundamental to describe the conveyor belt in the Mediterranean Sea, since the eddy contribution could reinforce or weaken the mean transport.

3.3 Meridional overturning circulation

In this section we compute the meridional-vertical streamfunction on the WMED and the EMED separately, the latter one further divided in Adriatic-Northern Ionian and Aegean-Levantine regions. This partition has been supported by many studies in the literature which place there well identified meridional transport cells (Pinardi and Masetti, 2000).

The regional description firstly presents eulerian streamfunction figures as the climatological mean over the entire reanalysis period, and then we complete the diagnostic study with residual streamfunction information referred to the same period. Within the residual framework, we show both representations in σ and $\zeta(\sigma)$ coordinate systems.

3.3.1 Western Mediterranean

Figure 3.1 presents the eulerian meridional vertical streamfunction (3.4) computed in the WMED. Surface transport has a cyclonic pattern up to 100 m depth, while it slowly decreases northward until 42°N, where strong deep convection areas are observed (Demirov and Pinardi, 2007).
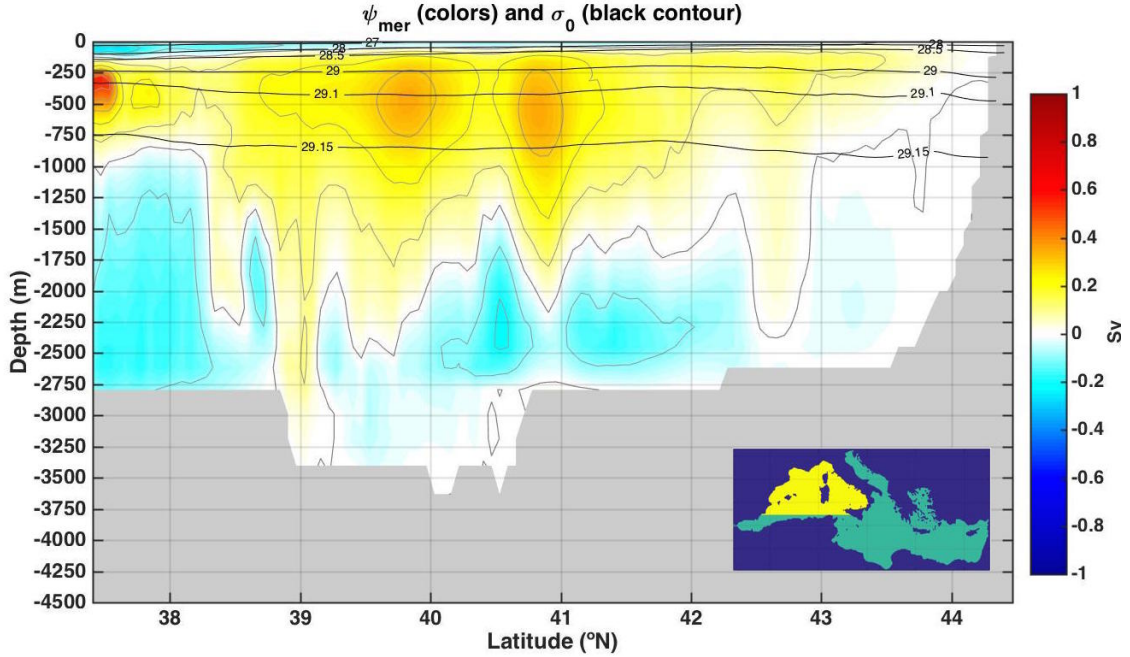
Figure 3.1: Eulerian meridional streamfunction of the WMED averaged over the 1987-2013 period. Grey contour lines represent streamfunction values with 0.1 Sv intervals, while black contours define isopycnal surfaces (expressed in kg/m^3). The grey area reveals the deepest bathymetry level for each longitudinal section of the basin. The map on the bottom shows the spatial domain over the streamfunction has been computed (*yellow area*).

The principal structure is a wide positive cell spread over the entire subbasin down to 2000 m which can be considered the meridional overturning circulation cell of the WMED; this cell is forced by the deep water mass formation typical of winter in the Gulf of Lyon (see Section 1.2), and influenced by the presence of LIW that composes the zonal overturning circulation described below (Wu and Haines, 1996).

In particular, deep convection events are visible in Figure 3.1 from 42°N to 43°N, where a narrow tongue sinks down to 2000 m according to MEDOC Group observation (1970). In our reanalysis, the water transport in this area is less than 0.2 Sv, while it is 1.6 Sv according to Castellari et al. (2000) during the *violent mixing* phase occurring during a few weeks in the wintertime (Demirov and Pinardi, 2007). This difference could be ascribed to the multidecadal average.

Previous studies have shown that the mesoscale variability in the Ligurian-Provencal basin strongly influences the processes of the WMED deep water formation and spreading, thus revealing a strong interaction between the basin scale and subbasin scale circulation (Swallow and Caston, 1973; Gascard, 1978; Madec et al., 1996). It's interesting to note what Legg and McWilliams (2001) demonstrated: deep convection area tends to have relatively small horizontal extensions and localize in the central part of the mesoscale vortices (Figure 3.2). Moving southward, two regions of 0.3 Sv define meridional transport intensification at 40°N and 41°N: the northern one, in addition to the weak cell around 42.6°N, corresponds to the deep water formation area

in the Gulf of Lyon, while the other is centered along a well known eddies pathway moving southward (Leaman and Schott, 1991).
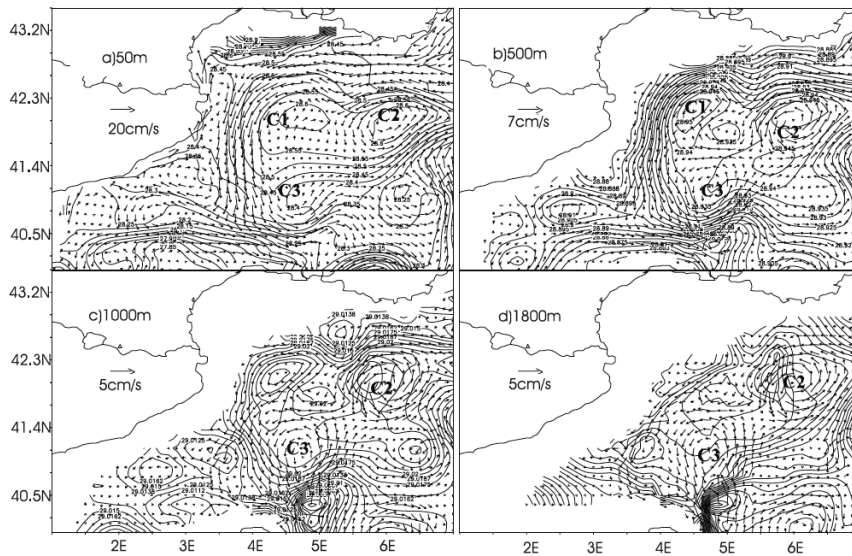

Figure 3.2: Mean velocity and density distribution in the Gulf of Lyon for the period 1-3 January 1987 at (a) 50 m; (b) 500 m; (c) 1000 m; (d) 1800 m. Taken from Demirov and Pinardi (2007).

An intense maximum of 0.6 Sv occurs in the southest part of the section between 200 m and 500 m, indeed, it could define the connection between meridional and zonal overturning circulation in the WMED. The zonal average leading to ψ_{mer} does not allow to identify the geographical area where the connection occurs. A different diagnostic, presented in section 3.5 will illustrate this connection.

Figure 3.3 shows the residual meridional streamfunction in the WMED, interpolated along $\zeta(\sigma)$ or $\sigma(z)$ respectively; hereafter we focus on the upper figure in order to compare ψ^*_{mer} and ψ_{mer} consistently. In this figure the widespread overturning cell is still present, but its shape is different from the eulerian case. Around 41°N two areas of intense transport occur on different depths: the first one is a narrow cell confined up to 200 m, and if we move downward, the same cell interacts with a deeper one down to 2000 m. This area is well described by Demirov and Pinardi (2007): they observed three wintertime eddies to 1800 m depth driving WMDW formation and spreading. This process is confirmed in our study by a buoyancy transport value of 0.8 Sv. On the contrary, the second maximum area obtained in Figure 3.3 around 40°N has little correspondence in the residual framework: in this case the residual flow is stronger down to 200 m and weaker than the eulerian case in deeper layers, suggesting that near the surface wind and eddy induced velocities add together, while down to 500 m they oppose.

From a general point of view, if we compare the eulerian and residual flows we note that the former is weaker than the latter, therefore during the period of interest the eddy-induced transport reinforces the eulerian flow.

In conclusion, unlike the eulerian streamfunction, the possible connection between

40

the meridional and zonal overturning circulations is in the form of a strong negative cell deeper than 300 m.
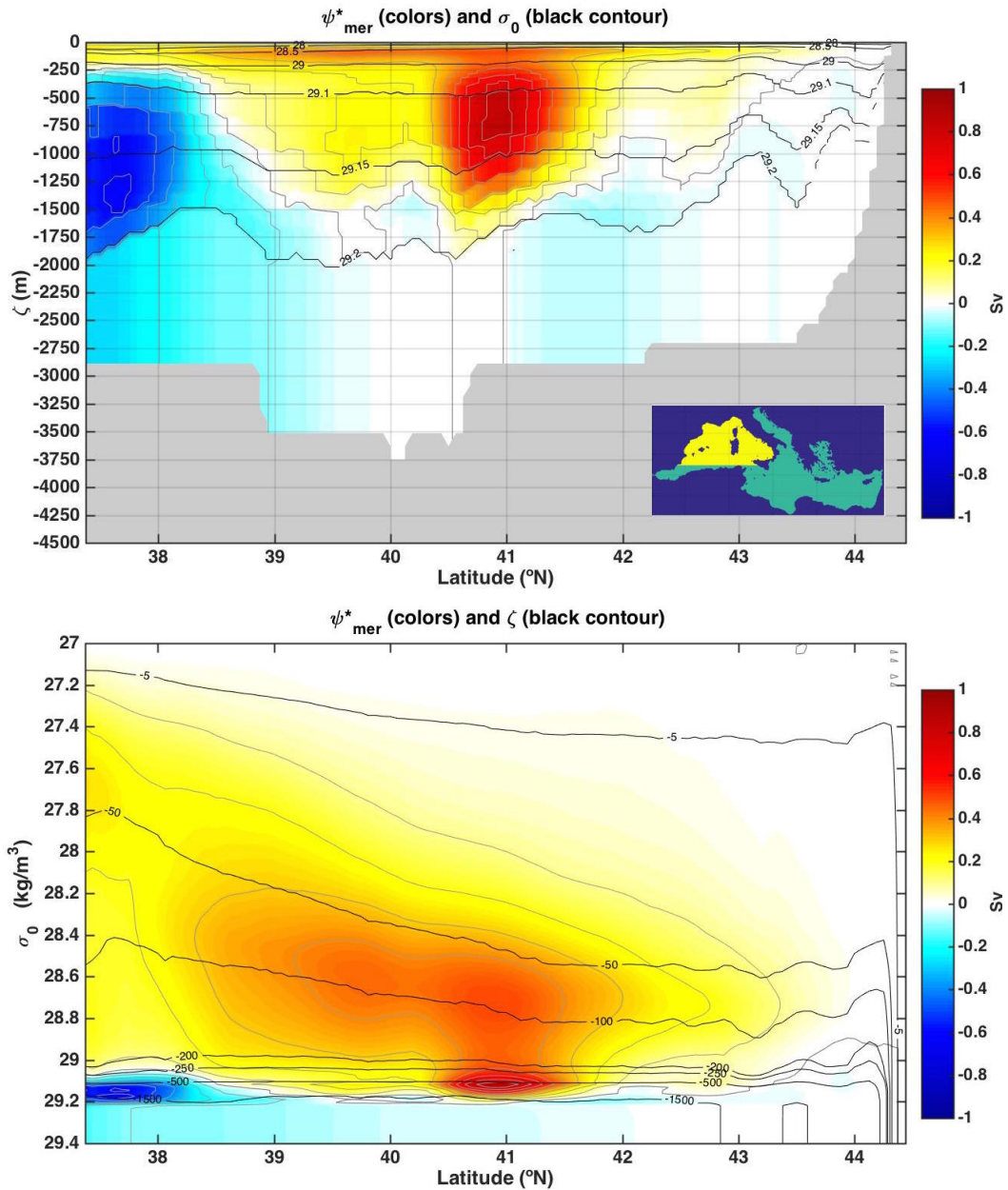

Figure 3.3: Residual meridional streamfunction of the WMED averaged over the 1987-2013 period. Grey contour lines represent streamfunction values with 0.1 Sv intervals. In the *upper figure*, ψ^*_{mer} is interpolated in depth coordinates and black contours define surfaces with equal potential density values σ_0, while the grey area reveals the deepest bathymetry level for each longitudinal section of the basin. In the *lower figure*, ψ^*_{mer} is interpolated on density coordinates and black contours define surfaces with equal depth values $\zeta(\sigma)$. Since bottom waters are homogeneous in density, using the residual streamfunction the bottom circulation is not reliable.

3.3.2   Adriatic - Northern Ionian region

The southern Adriatic Sea is considered as the principal area of Eastern Mediterranean Deep Waters formation, thanks to the cooling and evaporative processes acting on the shelf waters of the northern Adriatic, which sink along the continental slope (Zavatarelli and Mellor, 1995). Many studies have so far observed and simulated the volume transport across the Otranto Strait in order to quantify the outflow of deep waters in the Ionian Sea; according to several authors this process occurs yearly with a climatological value of 0.3 Sv (Artegiani et al., 1989; Lascaratos, 1993; Roether and Schlitzer, 1991; Briand, 2000).
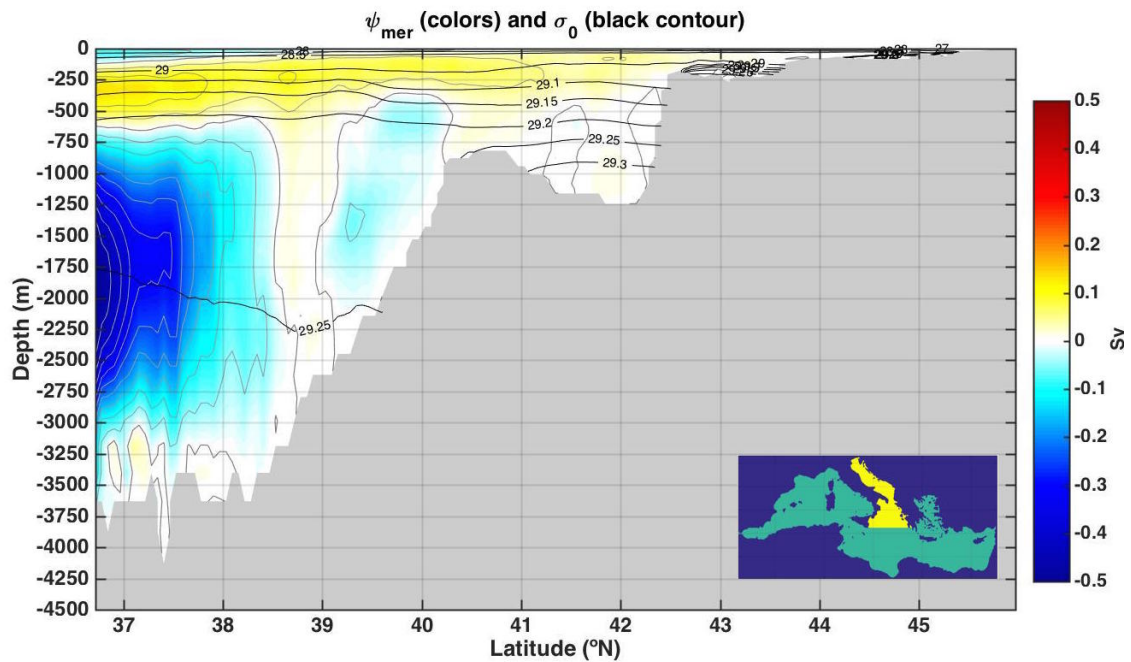

Figure 3.4: Eulerian meridional streamfunction of the Adriatic and Ionian Seas averaged over the 1987-2013 period. Grey contour lines represent streamfunction values with 0.05 Sv intervals, while black contours define isopycnal surfaces (expressed in kg/m^3). The grey area reveals the deepest bathymetry level for each longitudinal section of the basin; in the middle we recognize the Otranto Strait 800 m deep, which near 40.5°N separates the Adriatic Sea to the Ionian Sea. The map on the bottom shows the spatial domain over the streamfunction has been computed (*yellow area*).

Figure 3.4 shows a lightly defined anticyclonic cell in the Adriatic Sea of 0.1 Sv, underestimating the commonly quoted value of 0.3 Sv. This underestimate could be the consequence of the Eastern Mediterranean Transient (EMT) event occurred during the reanalysis period, which modified the LIW properties and then affects the Adriatic outflow (Theocharis et al., 2002). The anticyclonic cell extends out of the Otranto Strait and involves the intermediate layers of the northern Ionian Sea. Meanwhile, as in the WMED, the surface circulation moves southward due to a narrow vertical cyclonic cell weakening with latitude. Then, looking at deeper layers, another negative cell interests the Ionian Sea and reinforces the southward circulation at intermediate depths, from 300 m to 1500 m.
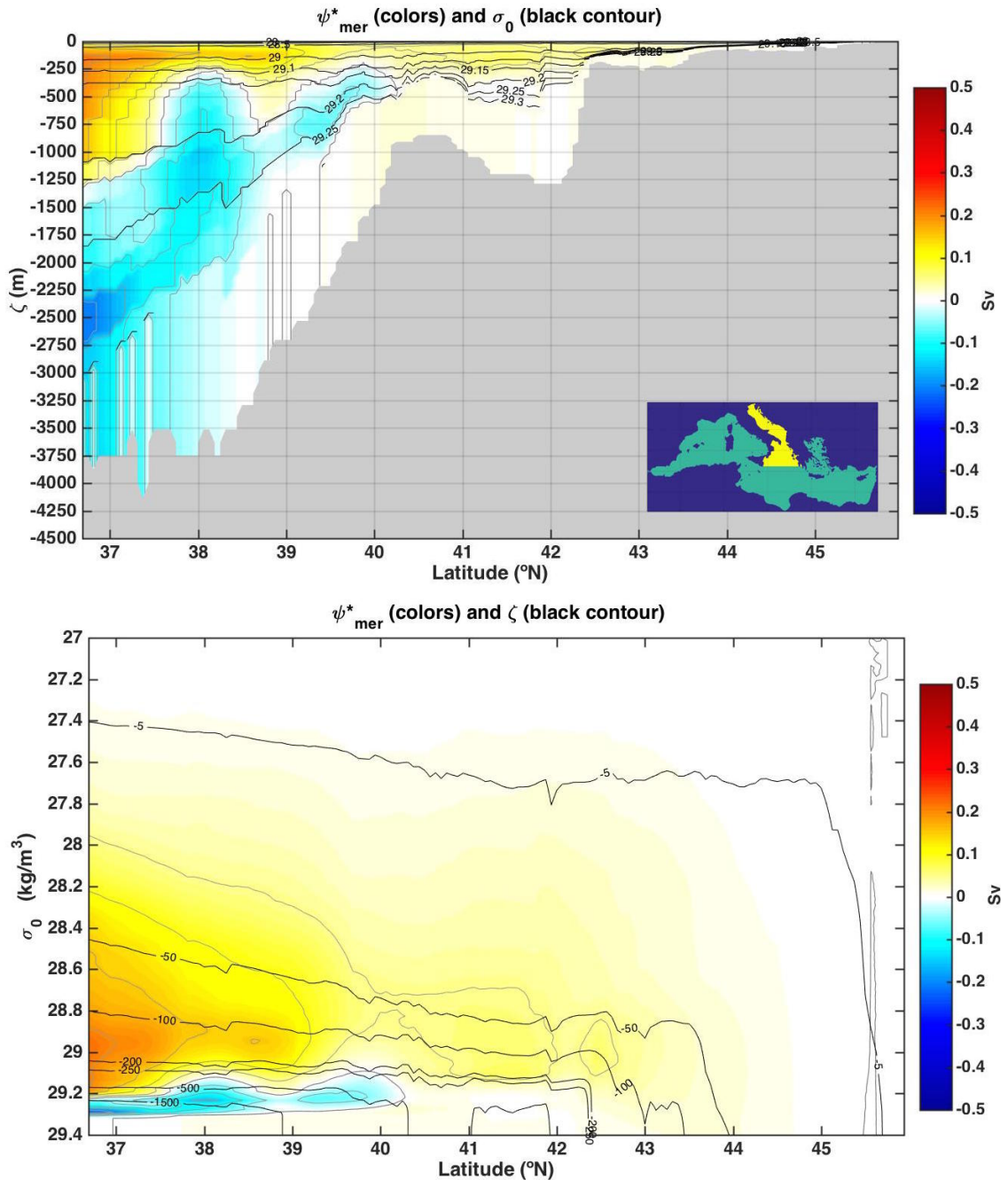
Figure 3.5: Residual meridional streamfunction of the Adriatic and Ionian seas averaged over the 1987-2013 period. Grey contour lines represent streamfunction values with 0.1 Sv intervals. In the *upper figure*, ψ^*_{mer} is interpolated in depth coordinates and black contours define surfaces with equal potential density values σ_0, while the grey area reveals the deepest bathymetry level for each longitudinal section of the basin. In the *lower figure*, ψ^*_{mer} is interpolated on density coordinates and black contours define surfaces with equal depth values $\zeta(\sigma)$. Since bottom waters are homogeneous in density, using residual streamfunction the bottom circulation is little reliable.

Figure 3.5 demonstrates that eddy-induced flow acts differently depending on the area we are considering: in the Adriatic Sea, the residual flow seems to be equal to the mean flow, i.e. eddies do not partecipate in the net transport. Instead, if we move southward, the residual transport has a maximum values of 0.4 Sv from the

surface to 1000 m depth. These values are higher than eulerian transport, suggesting that eddies play an important role on active tracers transport across the EMED in general, and the northern Ionian Sea in particular.

In this region we should consider also the Northern Ionian Reversal event (NIR) with decadal variability (Pinardi et al., 2015), because the reanalysis average might mask higher values of eddy transport.

Last but not least, deep residual circulation increases moving southward even if the cyclonic cell is weaker than the eulerian transport and it shows a non-uniform structure with a negative dome at 38°N down to 300 m depth (Figure 3.5). This structure develops down to the isopycnal of 29.2 kg/m^3 and it demonstrates the efficiency of buoyancy transport even in deep layers.

3.3.3 Aegean - Levantine region

This section describes the eulerian meridional vertical streamfunctions computed on a domain which is not compact and has discontinuous lateral boundaries. In particular, we consider a spatial domain limited in zonal direction by the Middle East coast and the Tunisian coast, whereas along the meridional direction we propose two extension cases, including first the Northern Ionian and Adriatic Seas (Figure 3.6), and then the Aegean Sea (Figure 3.7).
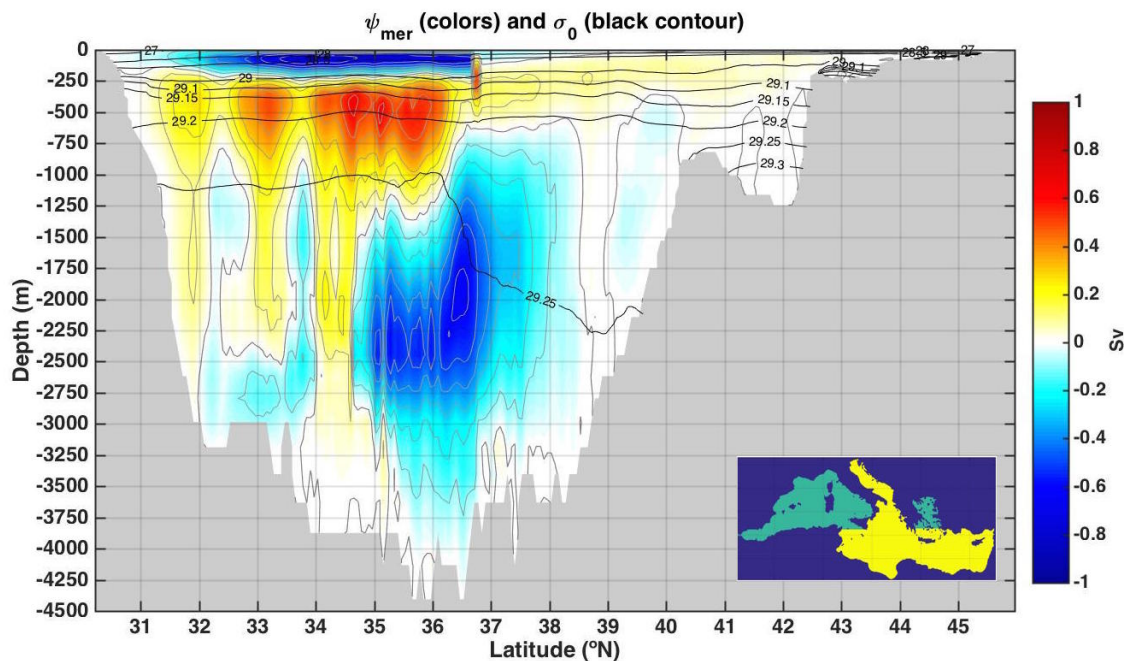

Figure 3.6: Eulerian meridional streamfunction of the Adriatic, Ionian and Levantine seas averaged over the 1987-2013 period. Grey contour lines represent streamfunction values with 0.1 Sv intervals, while black contours define isopycnal surfaces (expressed in kg/m^3). The grey area reveals the deepest bathymetry level for each longitudinal section of the basin. The map on the bottom shows the spatial domain over which the streamfunction has been zonally integrated (*yellow area*).
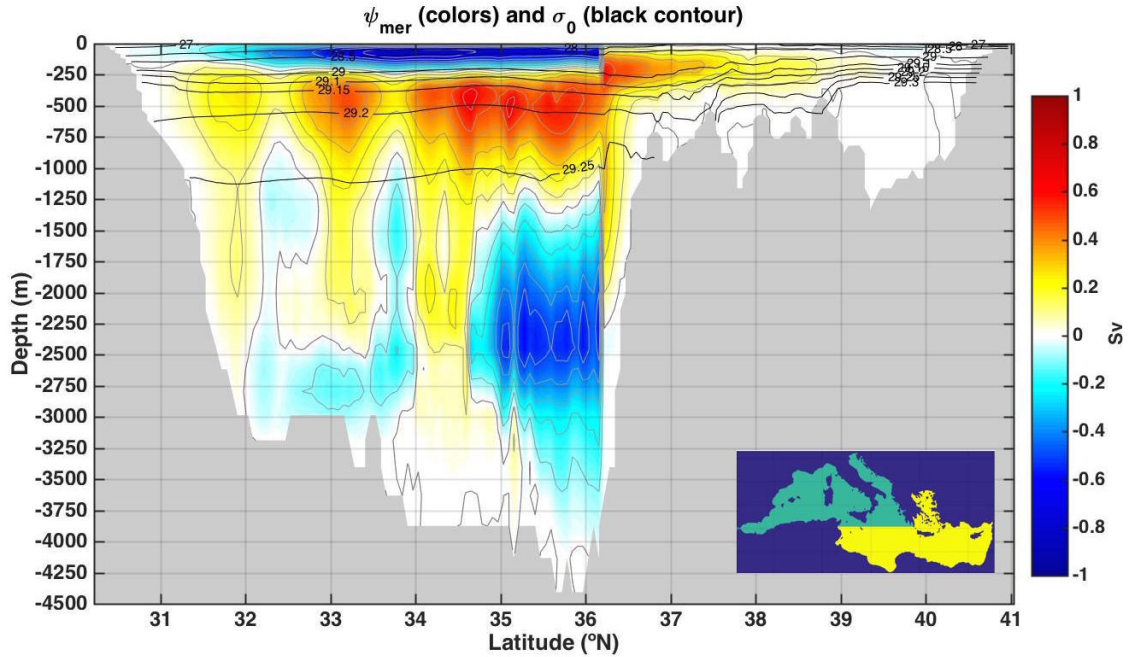
Figure 3.7: Eulerian meridional streamfunction of the Aegean, southern Ionian and Levantine seas averaged over the 1987-2013 period. Grey contour lines represent streamfunction values with 0.1 Sv intervals, while black contours define isopycnal surfaces (expressed in kg/m^3). The grey area reveals the deepest bathymetry level for each longitudinal section of the basin. The map on the bottom shows the spatial domain over which the streamfunction has been zonally integrated (*yellow area*).

This multiple visualization highlights the differential contribution of the marginal seas to deep water mass formation, and the consequent meridional overturning circulation in the entire EMED (Lascaratos et al., 1999).

In the Levantine and Southern Ionian seas there are three principal structures at different depths:

- a surface cyclonic cell, which describes an intense water motion in the upper layer;

- an intermediate multi-centered anticyclonic cell;

- a deep cyclonic cell, pushed down by the above anticyclonic cell.

The deep cell contour continuity in Figure 3.6 demonstrate that this structure is mainly displaced in the Ionian Sea, always lying down to the isopycnal surface of $29.20 \, kg/m^3$. On the other hand, the anticyclonic cell represents the mean meridional Levantine circulation; the weak connection to the Adriatic cell might suggest that the majority of the meridional transport during the reanalysis period occurs in the Eastern part of the Levantine Sea, and the multi-centered patter might depict the meandering around the mesoscale eddies typical of this region.

The Aegean-Levantine region has been affected by the EMT event from 1989 to 1995, when an influx of Aegean Sea water has replaced 20% of the deep and bottom waters of the Levantine Sea (Roether et al., 1996). Before this climatic event,

the only source of deep waters was the Adriatic Sea, and the waters of the Eastern Mediterranean were in near-steady state.

This reanalysis confirms that meridional overturning circulation in the Levantine Sea strictly interacts with the flow of Aegean waters. Figure 3.7 depicts the connection between the intense anticyclonic cells in the two areas: at first dense waters sink down in the Aegean, then flow out of the Cretan Sea, and finally they move southward across the Levantine Sea down to 700 m depth. In addition, the continuity of 29.2 kg/m^3 isopycnal along the whole section agrees with Theocharis et al. interpretation (1999), where net transport from the Aegean Sea is forced by two factors: the increase of deep water density in the southern Aegean ($\sigma_0 > 29.20 \, kg/m^3$) and the subsequent rise of the isopycnal surface 29.20 above the sill of the Cretan Arc straits. According to this interpretation, the distinctive element of the EMT role in the overturning pattern is its efficiency on deep water formation, which is four times greater than deep-water formation in the Adriatic (0.4 Sv versus 0.1 Sv) during the 1987-2013 period.

Note that in Figure 3.7 the Cretan Sea seems to be unaffected by the EMT from 35.7°N to 36.2°N, but this could be just a consequence of the zonal average where the strongest Ionian cyclonic circulation shadows the Cretan positive cell. For completeness, in Appendix C are shown figures describing the meridional overturning circulation referred to the years before, during and after the EMT event in the Levantine Sea.

Figure 3.8 represents the intermediate and deep horizontal currents in the Mediterranean Sea, showing a complex arrangement of gyres and meanders in the Levantine and Ionian Seas, and describing the main horizontal LIW pathway, typical of these layers.
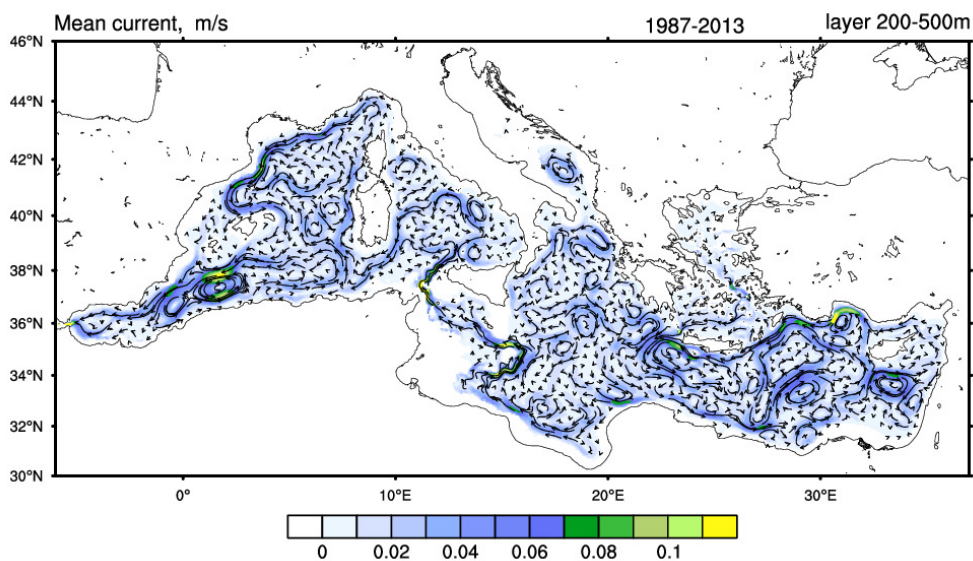

Figure 3.8: The 1987-2013 time-mean circulation from the reanalysis, averaged in the layer between 200 and 500 m.

Looking at this map, the main LIW meridional direction is unclear because of cyclonic and anticyclonic structures, but we can define the main way from Figures 3.6 and 3.7, where the streamfunction gradient defines an intense northward flux between 200 m and 500 m depth.

Below this layer the so-called *transition waters* moves southward, apparently forced by the Aegean outflow and the opposite motion of the LIW above. Even in this case, the horizontal deep water propagation pattern can be observed on a map, as shown in Figure 3.9.
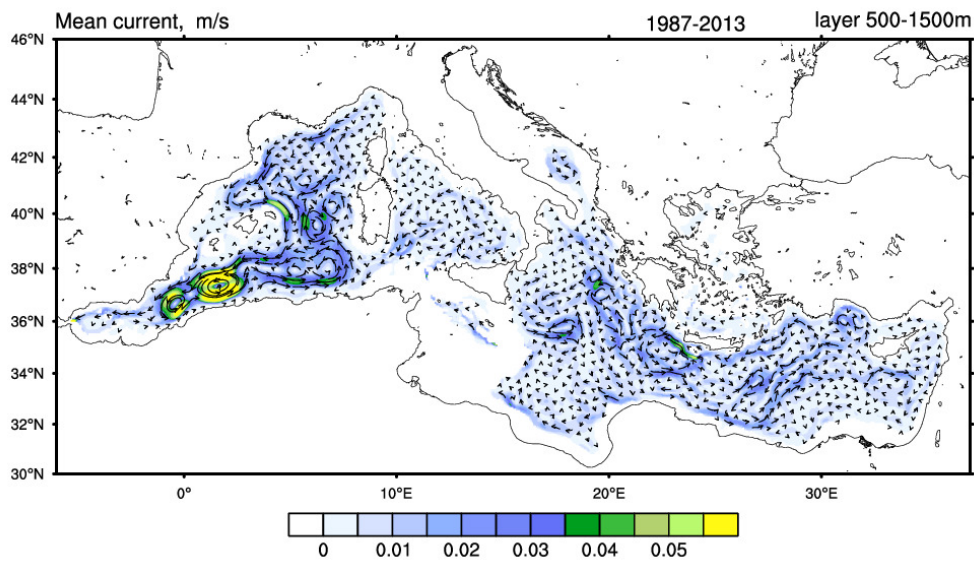

Figure 3.9: The 1987-2013 time-mean circulation from the reanalysis, averaged in the layer between 500 and 1500 m.

3.4 Zonal overturning circulation

The zonal overturning circulation is the specific vertical circulation of the Mediterranean Sea connected to the semi-enclosed nature of the basin. In the WMED the fresher Atlantic Water enters from the Gibraltar Strait and the upper branch moves eastward up to the Levantine Sea. Water masses are formed near the Rhodes basin (northern Levantine Sea, south of Rhodes) and move then westward, back to Gibraltar. LIW transport defines the lower branch of the overturning cell spreading saltier waters across the EMED and passing across the Strait of Sicily; LIW meanders in the WMED and finally closes the cell flowing out in the Atlantic Ocean (Lascaratos et al., 1999).

The eulerian zonal streamfunction has been discussed by Zavatarelli and Mellor (1995) and Pisacane et al. (2006) and our results are shown in Figure 3.10. A single *antiestuarine* (anticyclonic) cell connects the whole basin from the Gibraltar Strait to the eastern part of the Levantine Sea including upper and intermediate layers (Cessi

and Pinardi, 2014). On the contrary, the deep layers circulation has different features in the two subbasins:

- deep waters in the WMED move along a weak vertical cyclonic cell limited eastward by the Sicilian cell,

- while in the EMED the vertical deep circulation is anticyclonic, forming several subsurface meridional overturning cells probably connected to different deep water mass formation processes (Zavatarelli and Mellor, 1995).
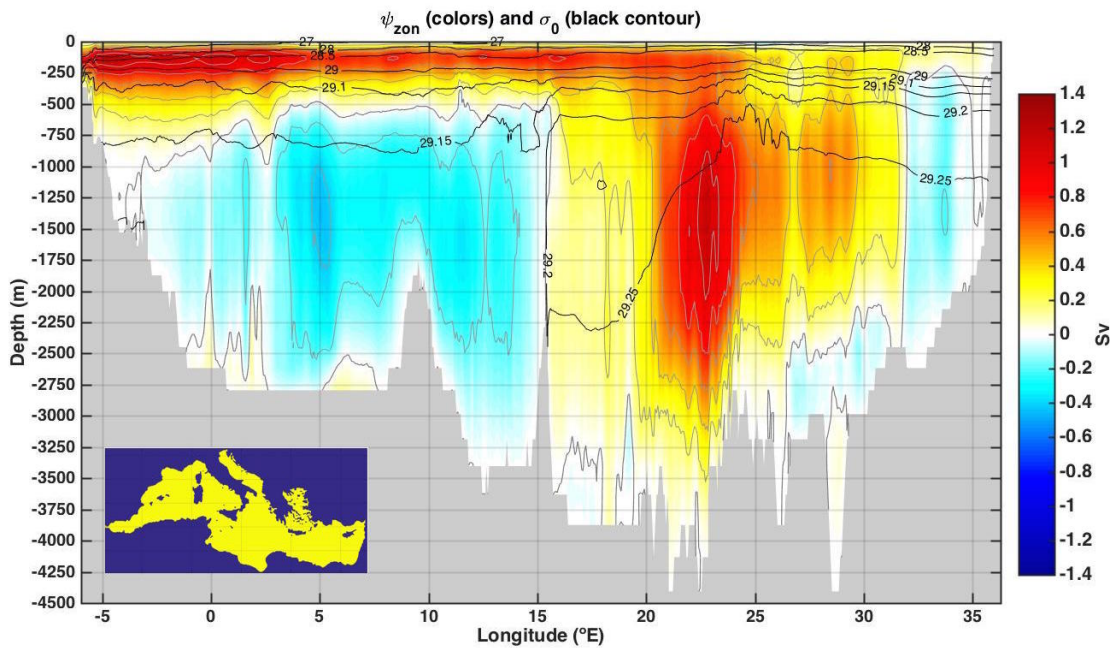

Figure 3.10: Eulerian zonal streamfunction of the Mediterranean Sea averaged over the 1987-2013 period. Grey contour lines represent streamfunction values with 0.2 Sv intervals, while black contours define isopycnal surfaces (expressed in kg/m^3). The grey area reveals the deepest bathymetry level for each latitudinal section of the basin; in the middle we recognize the Sicily Sill, which separates the EMED to WMED near 15°E. The map on the bottom shows the spatial domain over which the streamfunction has been integrated (*yellow area*).

The zonal antiestuarine cell changes intensity and thickness moving eastward. The upper branch is characterized by a rather homogeneous volume transport, which decreases from the west (1.1 Sv of AW) to the east (0.6 Sv), where MAW enters in the Ionian Sea and it spreads to the Levantine Sea. In this region, the surface anticyclonic cell merges with two deep anticyclonic cells. Going back westward, the LIW moves across the Ionian Sea and passes the Sicily Strait with 0.7 Sv transport rate (Zavatarelli and Mellor, 1995); then spreads across the Tyrrhenian and the Algerian Seas (Pinardi et al., 2015). In the Alboran Sea, the antiestuarine lower branch finally moves downward to 600 m and then rises up to 300 m flowing out into the Atlantic Ocean with 1.1 Sv rate. Such transport rate seems to be equal to the AW inflow at Gibraltar, but accurate studies demonstrated that the net flow has not a zero average.

In fact, the amount of fresh water deficit of the Mediterranean Sea, i.e. 0.7 m/y, is compensated by a net water influx at Gibraltar of 0.05 Sv (Mariotti et al., 2001).
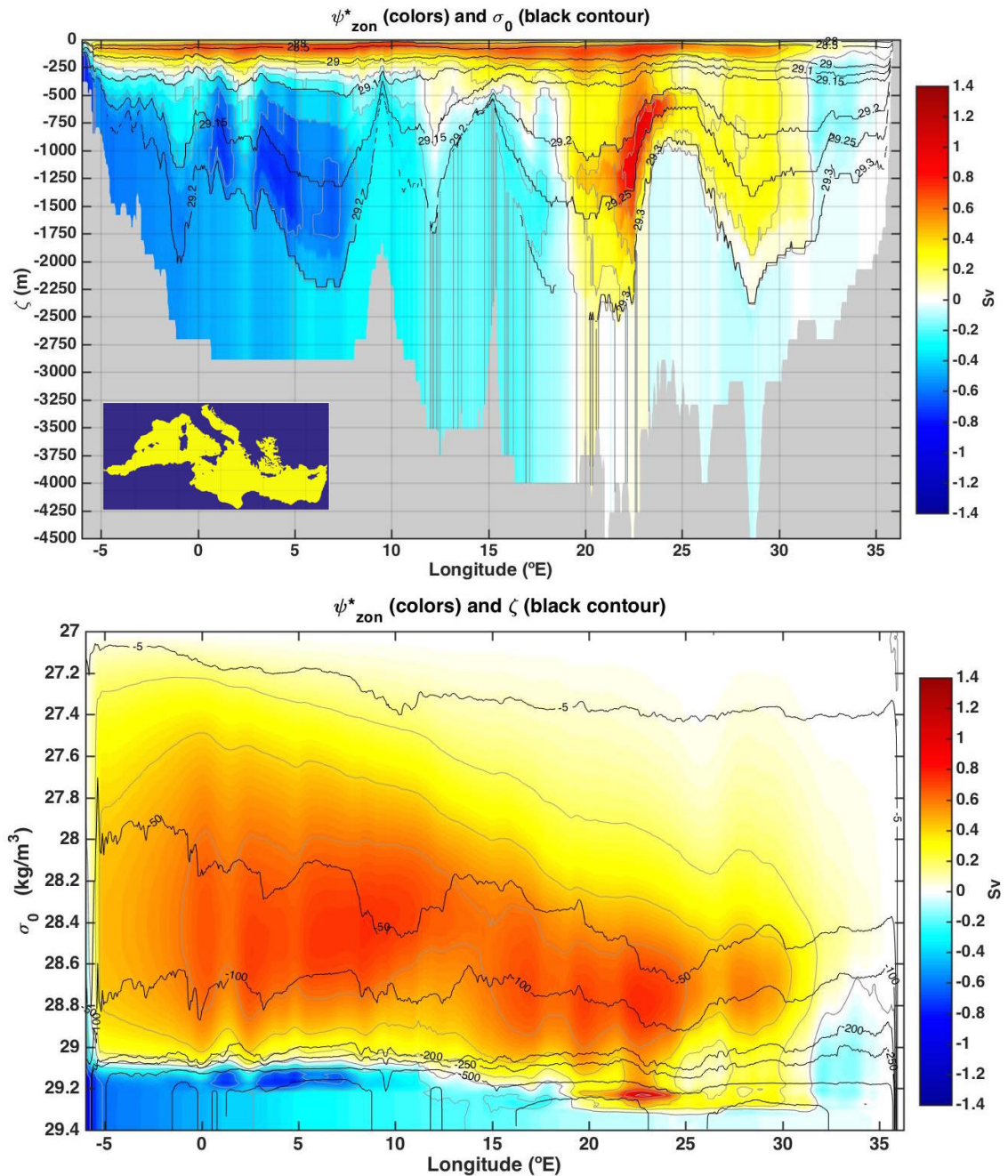

Figure 3.11: Residual zonal streamfunction of the Mediterranean Sea averaged over the 1987-2013 period. Grey contour lines represent streamfunction values with 0.2 Sv intervals. In the *upper figure*, ψ^*_{mer} is interpolated in depth coordinates and black contours define surfaces with equal potential density values σ_0, while the grey area reveals the deepest bathymetry level for each latitudinal section of the basin. In the *lower figure*, ψ^*_{mer} is interpolated on density coordinates and black contours define surfaces with equal depth values $\zeta(\sigma)$. Since bottom waters are homogeneous in density, using residual streamfunction the bottom circulation is little reliable.

Focussing on the EMED circulation and on the water patterns that occur in the Levantine Sea, in Figure 3.11 we can set three different areas, characterized by similar structures but different intensities:

- in the region from 26°E to 32°E, the cell centered at 28°E corresponds to a site of yearly water formation at the centre of the Rhodes gyre, with 0.5 Sv transport rate (Pinardi et al., 2015);

- in the region between 20°E and 26°E, the cell centered close to 23°E is the strongest deep zonal cell and its location coincides with the area of the intense EMT climatical event. In fact, this cell shows the Aegean Sea contribution to the EMED deep waters formation. The corresponding intensity of 1.0 Sv is weaker than the estimates rate of 1.2 Sv during the 1989-1995 period (Roether et al., 1996; Lascaratos et al., 1999), but this difference could be justified by the fact that the reanalysis period is longer. It must be noted that this cell shows a maximum value corresponding to the longitude of Antikithira Strait, and that the positive extension represents the Kassos Strait outflow. The effect of the EMT event is highlighted in Figure 3.12, where the intense deep water formation is not present until 1989, is very strong during the 1989-1995 decade, and finally detaches from the surface in the 1996-2013 period due to dissipation occurred in the thermocline;

- the region of positive values between 15°E and 20°E corresponds to the Adriatic and Ionian seas area, where water mass formation is weak relative to the EMT event and the overturning circulation could be influenced by the NIR.

Last but not least, in the EMED the interface between deep waters and the LIW is deeper than in the Sicily Sill, so the two main Mediterranean subbasins do not exchange deep-water masses with each other (Zavatarelli and Mellor, 1995).

Looking at the western deep cyclonic circulation, the two streamfunction minima, located at 5°E and 12°E, represent an internal subdivision of the WMED: shallow bathymetries in Figure 3.10 control the positions of Sardinia and Corsica islands, which are between the Algerian Sea and the Tyrrhenian Sea.

Note that the meridional average does not compromise zonal streamfunction values between 11°E and 15°E. In this region, in fact, we sum together information from the Tyrrhenian Sea and the Sicily Sea, but since the latter is deep only 500 m, the lower layers in the figure describe just the Tyrrhenian circulation.

Analogous structures are defined in Figure 3.11 by the residual zonal circulation. The antiestuarine cell is shallower than in the eulerian case, but in the eastern side it better illustrate the intermediate water formation in the Rhodes Gyre, around 30°. Moreover, it seems that up to 200 m residual transport moves along a reference depth rather than along isopycnals, implying strong diabatic effects.
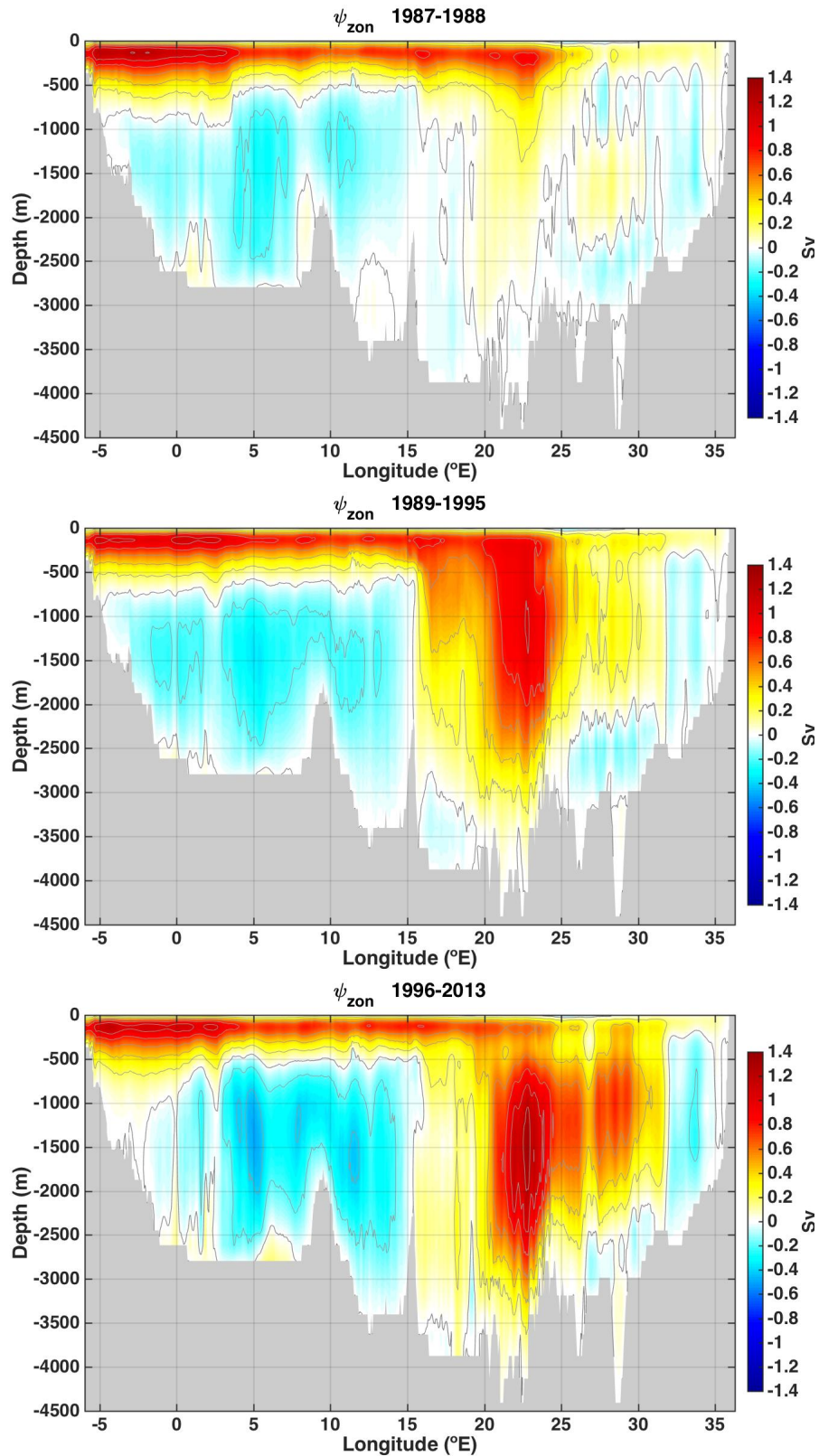
Figure 3.12: Eulerian zonal streamfunction of the Mediterranean Sea averaged over different period: (*top*) from 1987 to 1990, (*centre*) from 1991 to 1999, (*bottom*) from 2000 to 2013.

Volume and buoyancy transport follow different behaviors in deep layers, since the latter does not move along surfaces of equal depth both in the EMED and in the WMED. Particularly in the Levantine Sea, the general circulation appears to be dominated by subbasin gyres interconnected by jets whose presence is important to drive the active tracers transport. This is the case of the Rhodes gyre located at 28°E that contributes to the LIW mass formation as mentioned above (Lascaratos et al., 1999). In the WMED the deep eddy-induced circulation reinforces the mean flow since the transport reaches -0.7 Sv which should be compared to the traditional value of -0.4 Sv (see Figure 3.10).

On the other hand, the Ionian Sea in Figures 3.10 and 3.11 is characterized by opposite streamfunction signs, suggesting that the eddy-induced transport acts in opposition to the main flow in deep layers, therefore determining a net cyclonic deep circulation.

Up to now, meridional and zonal overturning circulations have been compared with the eulerian and residual framework for each of the three regions of interest: the Western Mediterranean, the Adriatic-Northern Ionian region, and the entire Mediterranean domain. Hereafter we analyse the connection between these overturning cells comparing the different figures related to the same traditional (or residual) computation. In fact, the domain used to calculate zonal streamfunction contains meridional domains too. The WMED meridional streamfunction illustrated in Figures 3.1 should be consistent with the results shown in the correspondent areas of the zonal streamfunction in Figure 3.10. For the same reason, the EMED meridional streamfunction should be consistent with the zonal streamfunction between 15°E and 20°E.

Quantifying the coherence is impossible because the meridional and zonal integrations (for ψ_{zon} and ψ_{mer} respectively) have lost the necessary data resolution: though, qualitative similarities are hereby commented.

Eulerian streamfunction. In the WMED we recognize the same anticyclonic cell both in the meridional and in the zonal circulation, which reaches its maximum depth around 600 m. In deep layers, instead, cyclonic cell in the zonal streamfunction seems to be stronger than the meridional case. The EMED on the contrary is characterized by strongly different features, i.e. an intense negative cell in the meridional circulation compared to a weakly positive transport in the zonal representation.

Residual streamfunction. In this case intensity and thickness of cyclonic and anticyclonic structures match with each other both in meridional and zonal transports. The case of EMED is particularly interesting, since the positive cell described in the meridional vertical streamfunction up to 1000 m (Figure 3.5) is perfectly visible also in the zonal streamfunction, and moreover the lower cyclonic cell is centered at 1500 m depth for both cases.

3.5 Horizontal circulation

Vertical streamfunctions have so far described the Mediterranean conveyor belt system and how it meanders across the Mediterranean Sea. Deep water mass formation events are expected to be the main forcing factors, but the zonal antiestuarine cell is the only apparent connection between the Mediterranean subbasins. To conclude this diagnostic study, we have computed the horizontal streamfunction as the best representation of the transport horizontal distribution.

The antiestuarine zonal circulation cell always remains shallower than 500 m, therefore we integrate the continuity equation (2.3) from the surface down to 500 m depth ($\bar{h}$):

$$\int_{-\bar{h}}^{0} \frac{\partial u}{\partial x} dz + \int_{-\bar{h}}^{0} \frac{\partial v}{\partial y} dz = w(-\bar{h}) - w(0) = w(-\bar{h}) \,. \tag{3.8}$$

Since vertical velocity does not vanish, the resulting horizontal field is divergent, so we couldn't compute a perfect horizontal streamfunction. Nevertheless we calculate it to have a qualitative information about the conveyor belt pattern. We define

$$\psi_h(x,y) = \frac{1}{T} \int_{t_0}^{t_1} \int_{-\bar{h}}^{0} \int_{x_{B1}}^{x} v(\tilde{x}, y, z, t) \, d\tilde{x} \, dz \, dt \,. \tag{3.9}$$
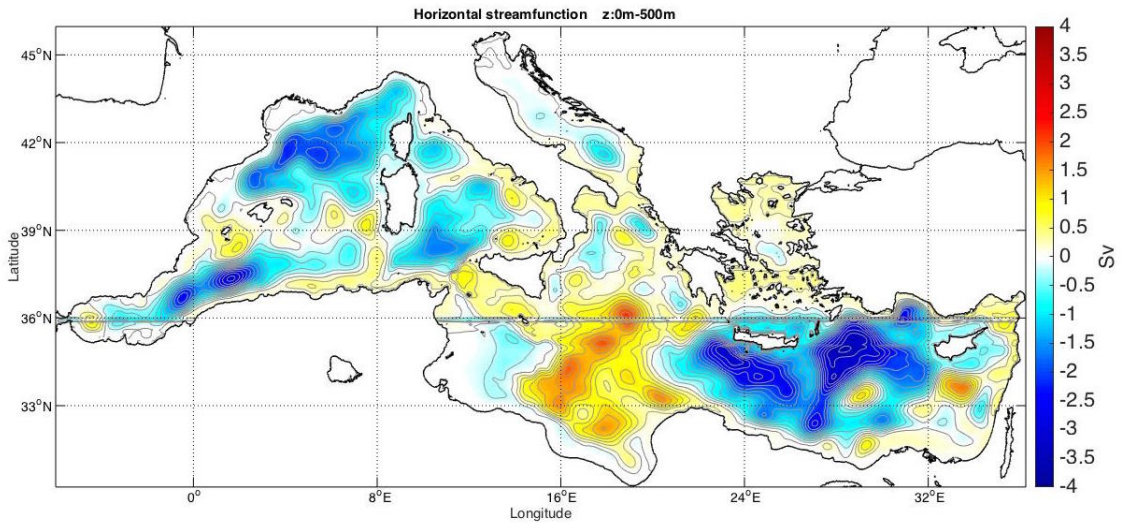

Figure 3.13: Eulerian horizontal streamfunction of the Mediterranean Sea averaged over the reanalysis period. The horizontal velocity field integrated from the surface to 500 m is slightly divergent because of small vertical velocity at the bottom of the layer considered.

Figure 3.13 shows surface and intermediate waters pathway moving across the Mediterranean Sea. The 500 depth average circulation, considered as a streamfunction, gives us the direction of flows in the horizontal that contribute to the zonal and meridional vertical circulations. Figure 3.10 showed the zonal and Figure 3.7 the meridional vertical cells that compose the Mediterranean Conveyor system. Together with 3.13 we can attempt to draw a three dimensional picture of the Mediterranean

circulation.

The Atlantic water moves around the 3.13 streamfunction poles until it reaches the Rhodes Gyre where it is transformed by the intense air-sea fluxes and downwells at intermediate depths, going back toward the Gibraltar Strait. At intermediate depths in the Levantine basin, the circulation is forced to move along the northern boundary, enter into the Cretan Sea and then move southward following the Syrte anticyclonic Gyre. South of Malta, the northward flow on the Syrte Gyre branches and enters the Sicily Strait so that LIW enters in the WMED.

Intermediate water circulation continues in the Tyrrhenian Sea as a coastal current along the eastern coast (Pinardi and Navarra, 1993); when getting to the Ligurian-Provencal Sea, the modified LIW interacts with local waters and contributes to the WMED Deep Water formation (Demirov and Pinardi, 2007). Hereby, the conveyor belt flows across the Alboran sea, it moves along the northern Spanish coasts and it finally flows out to the Strait of Gibraltar.

The schematic of the surface (blue arrows) and intermediate circulation (green arrows) is depicted in Figure 3.14.
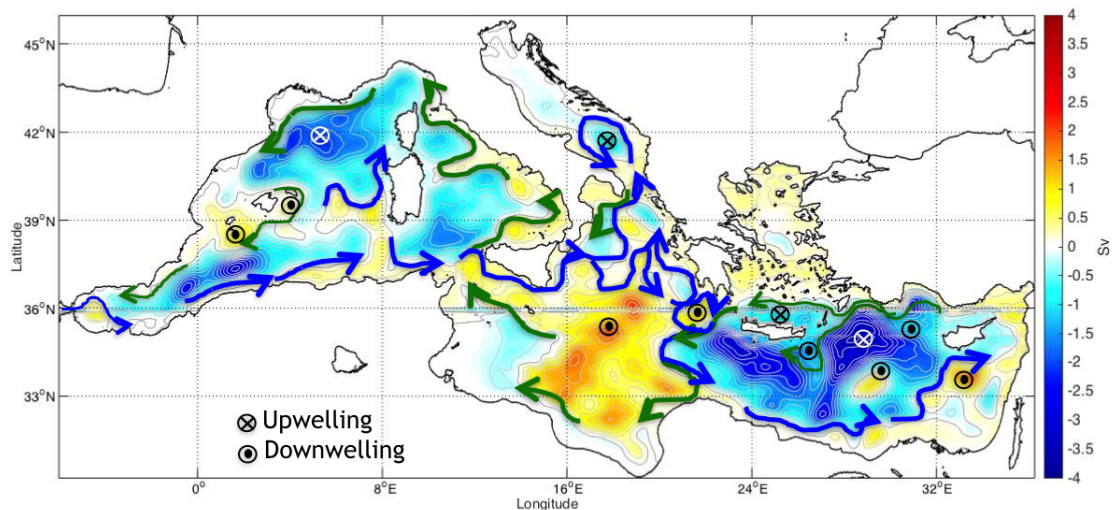

Figure 3.14: The 3D general circulation depicted over the 0-500 meter depth averaged streamfunction, considering the meridional and zonal overturning cells directions. The *blue* arrows indicate the prevailing direction of flow in the zonal and meridional cells at the surface, while the *green* at 500 meters. The prevailing flow directions depicted consider that zonal (meridional) cells integrate in the meridional (zonal) directions.

In order to map a three dimensional circulation we have chosen to overlay on the streamfunction field of 3.14 the pathways of surface and intermediate flow that prevail at the different depths. In other words the different color arrows indicate the prevailing depth dependent flow field that concur to the vertical circulation cells of Figures 3.1, 3.4 and 3.6.

One interpretation of this is that for the zonal cell the eastward branch of the vertical circulation is dominated by the Algerian current, the Atlantic-Ionian Stream

and the southern Levantine current, as well as the Mid-Mediterranean jet.

The westward branch of the circulation is instead dominated by the northern flow in the Northern Levantine and the Cretan Sea, the southern Lybian anticyclone rim current and the northward flow field along the Tyrrhenian coasts and the return flow along the Liguro-Provencal basin, the Balearic islands and the cyclonic circulation in the Algerian basin. This schematic is a preliminary synthesis of the Mediterranean Conveyor Belt system.

Chapter 4

Prognostic studies

The previous chapters have analyzed the Mediterranean Sea vertical circulation describing climatological reanalysis data and illustrating the main meridional and zonal structures. It has been shown that many factors contribute to maintain the overturning circulation on different time and spatial scales, but diagnostic studies do not distinguish processes responsibility for overturning variability. This crucial information could be investigated with model simulations, setting different bathymetry, surface and lateral boundary conditions, atmospheric forcing, diffusive and turbulent coefficients.

This chapter describes a model set-up useful to simulate the vertical circulation. We use the University of Bologna SURF model with the NEMO code, to maintain the same physical equations as in the reanalysis. Once parameters are fixed, it is possible to study different Mediterranean regimes of circulation by changing two fundamental conditions: the Gibraltar Strait open boundary condition and the atmospheric forcing structure.

4.1 SURF model

The relocatable ocean model SURF (Structured and Unstructured Relocatable ocean model for Forecast) is devoted to produce a relocatable ocean modeling system characterized by rapid implementation in any Mediterranean region. If the user wants to include waves information in a specific experiment, then NEMO ocean circulation model is coupled with wind-wave model SWAN (Simulating WAves Nearshore) developed by Delft University of Technology.

In order to retain the high frequency variability of atmospheric forcing and boundary conditions during the numerical experiment time interval, the model uploads ocean fields from the operational Mediterranean Forecasting System (MFS) model, and atmospheric surface fields from the European Centre Medium-Range Weather Forecast (ECMWF) products. Figure 4.1 shows the SURF model work-flow. The next sections describe the input-data phase requires to set model configuration.
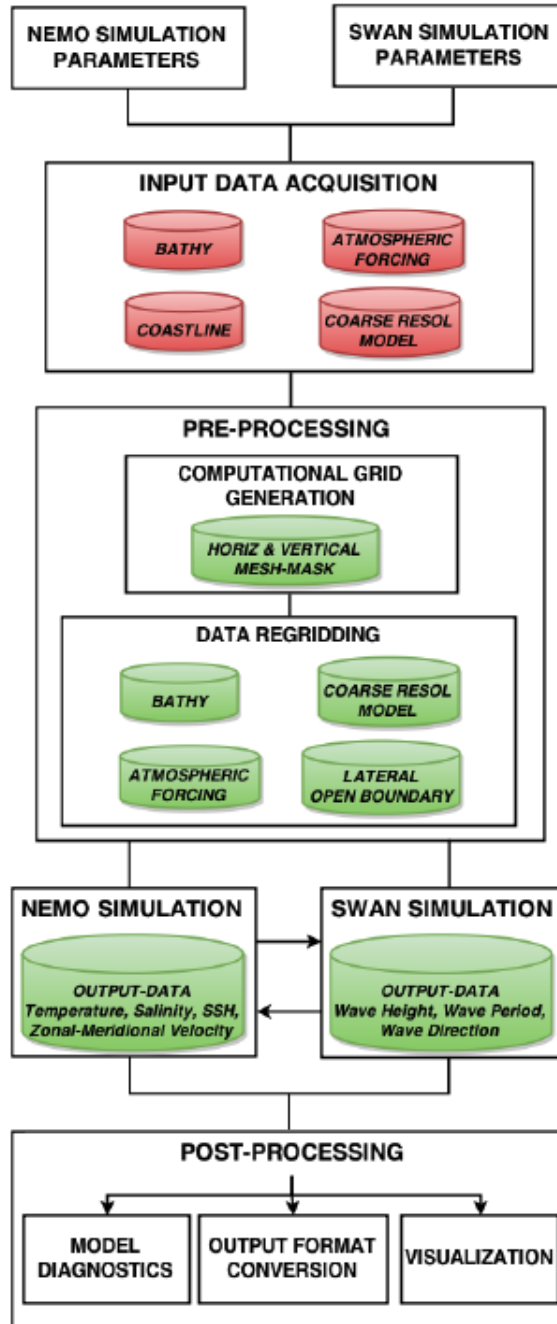
Figure 4.1: Work-flow of the Relocatable ocean model SURF based on NEMO-SWAN Model. Taken from SURF manual.

4.2 Spatial domain

The geographical domain covers the entire Mediterranean Sea and a portion of the Atlantic Ocean, where an Atlantic box is designed to parametrize coupling between the semienclosed basin and the open ocean. The total extension has coordinates from 17.5°W to 36.125°E, and from 30.25°N to 45.875°N.

The horizontal resolution is 1/8° in both latitude and longitude directions, so we

define an *eddy-permitting* regime. This choice is essential to limit computational time required in each simulation, even if it means to increase distances between grid points with respect to MFS *father* fields (equal to 1/16° grid).

We impose 50 vertical levels from the surface to a maximum depth of 6000 m, and the corresponding thickness varyes from 4 m at the top to 430 m in the deepest layer of the Atlantic box (Figure 4.2). The vertical grid generation is managed in NEMO by a set of non-uniform z-coordinate levels, given by the definition of the following analytic expression:

$$z(k) = h_{sur} - h_0\, k - h_1\, log[cosh((k - h_{th})\, h_{cr})]\,, \tag{4.1}$$

where the coefficients h_{sur}, h_0, h_1, h_{th} and h_{cr} are parameters specified as in MFS system; h_{cr} denotes the stretching factor of the grid and h_{th} is the approximate model level at which maximum stretching occurs.
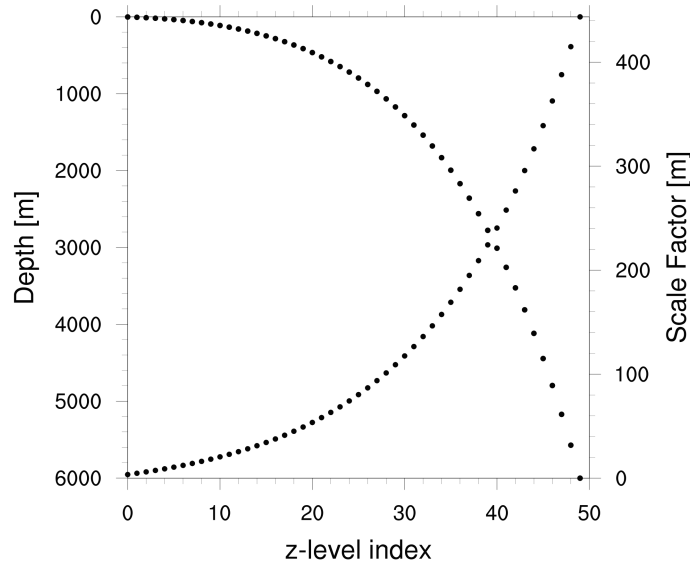

Figure 4.2: Vertical grid description according to model set-up. There are 50 levels, each of them identified by a reference depth (left scale) and a reference thickness (scale factor, right scale). According to the *partial cell* representation, the bottom layer thickness varies as a function of position in order to fit the input bathymetry.

4.3   Bathymetry and coastline

Bathymetry in the Mediterranean Sea is crucial to reproduce the correct geographical distribution of deep water formation. We know that the basin is subdivided in two regions by the Sicily Sill with maximum depth of 500 m. The Adriatic is a marginal sea bouded by the Otranto Strait 800 m deep, and large areas shallower than 300 m. We use an idealized coastline with a realistic bathymetry because with a realistic coastline it would be impossible to understand the key parameters responsible for the observed circulation.

In our idealization, we remove all islands in the Mediterranean Sea except:

- Cyprus,

- Crete,

- Sardinia and Corsica (here regarded as a single island),

- the greatest Balearic island,

- Sicily.

Except for Sicily, we approximate all islands using rectangular shapes; then we straighten every continental coast.

However, we keep a realistic bathymetry smoothing small-scale variability; our point of departure is the bathymetry file downloaded from GEBCO website (General Bathymetric Chart of the Oceans), containing the entire domain with $1/120°$ resolution grid, which is smoothed until the deepest point of the Mediterranean basin is less than 4000 m. The smoothing procedure uses a Gaussian filter function that associates to each cell the 25-nearest points weighted-average.

Finally, in order to merge bathymetry and coastline information consistently, we apply the *sea over land* procedure that extrapolates iteratively the ocean depths on the land grid-points. The difference between the original GEBCO bathymetry and the model one is shown in Figure 4.3 and 4.4.

During the pre-processing phase, the model applies the last adjustment to bathymetry file defining a *minimum depth* value, which imposes that shallow water regions must be at least 10 m deep to better simulate the dynamic structures of that regions.
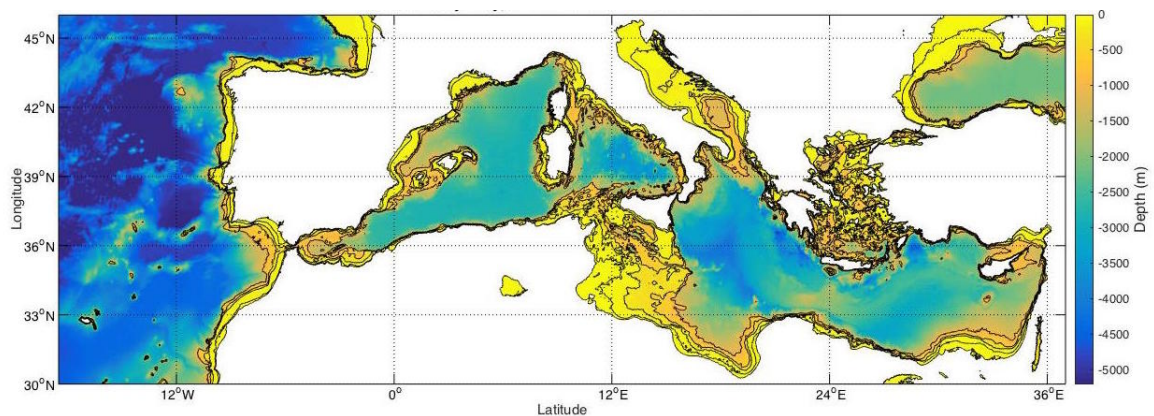

Figure 4.3: GEBCO bathymetry in the model domain. The resolution grid is $1/120°$ and positive values are showm as white regions. Contour lines define surfaces at 0 m, 50 m, 200 m, 500 m and 1000 m.
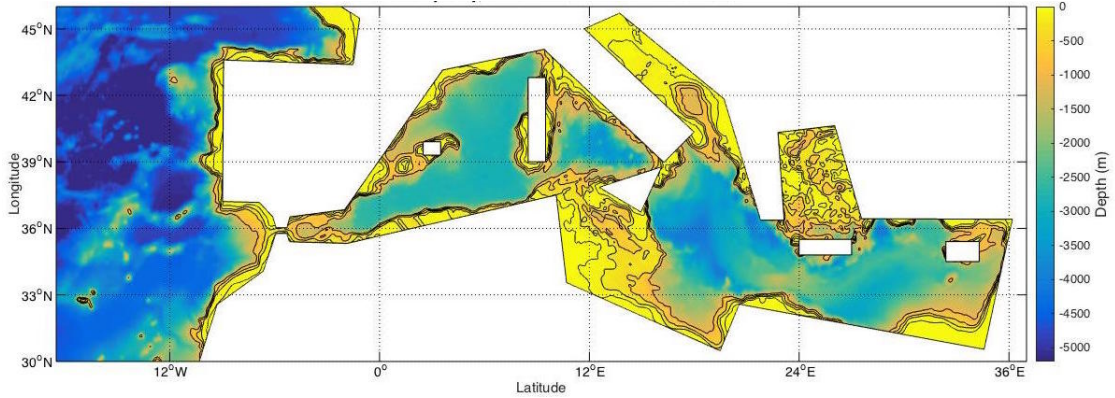
Figure 4.4: Smoothed model bathymetry with idealized coastline. Contour lines define surfaces at 0 m, 50 m, 200 m, 500 m and 1000 m.

4.4 Boundary conditions

Boundary conditions available on SURF model are suitable for forecasting studies, because the model requires daily atmospheric and oceanic fields and compute relaxation bulk formulas on air-sea interface. Our purpose, instead, is to reproduce dynamical structures with decadal timescales and basin-like spatial scale, so we have changed some input requirements in order to use monthly climatologies instead of daily data.

We plan to run the model with perpetual monthly-mean forcing in order to reproduce the seasonal cycle in the basin, setting a *perpetual-year* time evolution. These monthly-mean climatological data come from the reanalysis dataset, so we are going to simulate the same circulation observed during the reanalysis decades from 1987 to 2013. In this case transient climatological events are included in the temporal average although smoothed for the entire period.

Output files are provided by the model at intervals of 10 days of simulation, and they contain the average scalar and vectorial fields from the previous output.

Taking into consideration climatological forcing, we change vertical boundary conditions, describing air-sea interaction at the surface as fluxes of heat and fresh water. The heat exchange at the surface is described by flux-formulation:

$$Q = Q_0 + \frac{dQ}{dT} \left(T|_{k=1} - SST_{clim,m} \right) , \tag{4.2}$$

where Q_0 is the mean heat budget imposed equal to zero, $T|_{k=1}$ is the temperature on the model surface layer, $SST_{clim,m}$ is the climatological sea surface temperature different in each month, and dQ/dT is the relaxation coefficient.

Similarly, the net surface fresh water flux is set to zero ($emp_0 = 0$), and the relaxation equation is:

$$emp = emp_0 + \gamma_S^{-1} \, e_{3t} \, \frac{\left(S|_{k=1} - SSS_{clim,m} \right)}{S|_{k=1}} , \tag{4.3}$$

61

where $S|_{k=1}$ is the salinity on the model surface layer, e_{3t} is its thickness, $SSS_{clim,m}$ is the climatological monthly mean of sea surface salinity and γ_S is the relaxation coefficient.

On the other hand, at the bottom level, friction is modeled by a quadratic function with the additional coefficient of a turbulent kinetic energy due to tides and other unresolved processes (Lyard et al., 2006).

No-slip conditions are applied on closed lateral boundaries, while on the Atlantic box frame we impose open-boundary conditions settled by monthly mean climatological oceanic fields.

The following figures illustrate the first test simulation results, showing the input velocity field of October climatology (Figure 4.5) and the output mean velocity field for 30 days of simulation (Figure 4.6).

In Figure 4.5 the difference between coastline and points where the velocity field is defined in Figure is due to the fact that input files are taken from the reanalysis climatology, with realistic coastline. This inconsistency is taken care of with the *sea over land* procedure application during pre-processing phase. In conclusion, Figure 4.6 shows that the model maintains the same pattern of input current, describing an intense flow in the Alboran Sea, and northern intensifications typical of Mediterranean gyres in the Gulf of Lyon, the Sicily Sea and the Levantine Sea.
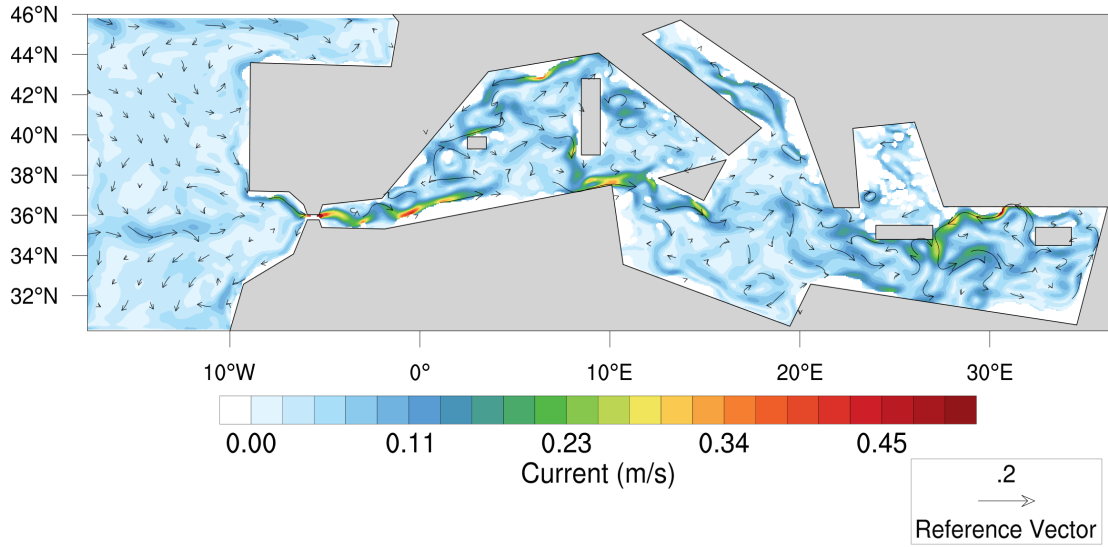
Figure 4.5: Map of input surface velocity field referred to October climatology. Colours describe current intensity, while arrows define moving direction. Plot obtained using SURF model.
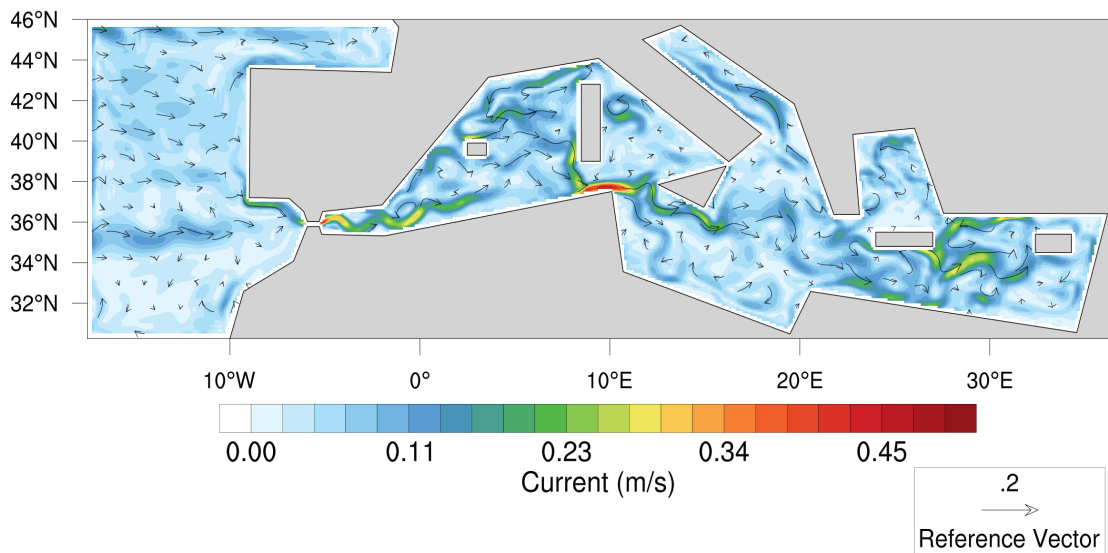

Figure 4.6: Map of output surface velocity field plotted by SURF model, as temporal average over 30 days of simulation. Colours describe current intensity, while arrows define moving direction.

4. Prognostic studies

Chapter 5

Conclusions and outlooks

In this thesis, the the Copernicus Marine Environment Monitoring Service reanalysis dataset has been used to characterize the Mediterranean conveyor belt and its general pathway in the basin. First of all the diagnostic studies have reproduced with modern observations the Wüst vertical water mass structure. A detailed investigation of the basin density characteristics has followed which allowed to detect the critical isopycnals for the streamfunction calculations. To get a more realistic representation of water masses transport, our analysis has considered two different vertical streamfunctions computed along different vertical coordinates.

This study confirms the presence of three deep convection sites in the Mediterranean basin, located in the Gulf of Lyon, the southern Adriatic Sea and the Aegean Sea; the deep water formation rate values obtained in these regions are coherent with observations and numerical simulations proposed in the literature. Intermediate water mass formation in the Levantine Sea is illustrated by the residual zonal vertical streamfunction. This cell, not visible in the eulerian framework, confirms the correspondence between the LIW formation site and the Rhodes Gyre at 30°E.

Our study highlights the dependence of overturning circulation on atmospheric and oceanic transient events, which affect water transport not only at the time of their occurrence, but also in the following decades. This behavior might be associated to the EMT climatic event that caused deep water formation in the Aegean and Cretan Sea during the 1989-1995 period, but has also generated a deep convection cell still present in the Levantine Sea, both in meridional and zonal directions.

We could assume that the meridional and zonal deep cells in the EMED are connected between them because of they have the same source. Other connections occurs in deep water mass formation sites, where the LIW presence contributes to trigger the formation process.

The residual streamfunction allows to evaluate the contribution of eddies and gyres to general transport along the Mediterranean Sea, showing different behaviors depending on regions:

- in the southern Adriatic Sea eddies participation is negligible to deep water

formation;

- in the Ionian Sea as well as in the Gulf of Lyon, the meridional eddy-induced velocity reinforces the mean transport;

- in the Gulf of Syrte and the Ionian Sea eddies and gyres oppose the mean zonal circulation.

Moreover, where residual transport does not move along isopycnal surfaces diabatic effects must be important.

After the vertical overturning circulation description in the meridional and zonal directions, the Mediterranean conveyor belt has been evaluated considering the horizontal streamfunction. The vertical integration down to 500 m demonstrates that Levantine Intermediate Waters meander from their formation area to other deep water formation sites, joining meridional overturning cells of the eastern Mediterranean with the western ones.

A notable observation regards LIW currents intensification along the boundaries, which can be visible at the surface (the Italian coastline) or detected along continental shelfs (offshore Tunisia).

A final schematic of the three dimensional circulation has been depicted that shows for the first time how different current segments of sub-basin scale gyres contribute to the vertical overturning circulation of the Mediterranean Sea.

In conclusion, the above mentioned considerations are crucial to understand Mediterranean conveyor belt system. A first step could be to investigate the Mediterranean response to coastline modification, studying whether the LIW still reaches deep water formation sites, or whether these waters are forced to follow the Atlantic Water pathway in a different direction.

Then, we could change boundary conditions at Gibraltar Strait, studying the meridional overturning circulation response and its behavior during long timescale.

Finally, we could study the Mediterranean conveyor belt without any transient climatological event, trying to understand if temporal variability weakens or reinforces the overturning circulation mean intensity. Each of these questions corresponds to a specific set of boundary and geographical conditions which could be applied to numerical simulations using the SURF model.

Appendix A

Seawater equation of state

Jackett and Mc Dougall (1996) have proposed the following equation of state:

$$\rho(S, \theta, p) = \frac{\rho(S, \theta, 0)}{1 - p/K(S, \theta, p)} \ .$$

Here $K(S, \theta, p)$ is a 26-term equation in powers of S, θ and p, the coefficients being determined as in the following table:

$K(S,\theta,p)$ terms	$K(S,\theta,p)$ coefficients	$\hat{K}(S,\theta,p)$ terms	$\hat{K}(S,\theta,p)$ coefficients
constant	1.965933×10^4	constant	1.965221×10^4
θ	1.444304×10^2	T	1.4842066×10^2
θ^2	-1.706103×10^0	T^2	-2.327105×10^0
θ^3	9.648704×10^{-3}	T^3	1.360477×10^{-2}
θ^4	-4.190253×10^{-5}	T^4	-5.155288×10^{-5}
S	5.284855×10^1	S	5.46746×10^1
$S\theta$	-3.101089×10^{-1}	ST	-0.604359×10^0
$S\theta^2$	6.283263×10^{-3}	ST^2	1.09987×10^{-2}
$S\theta^3$	-5.084188×10^{-5}	ST^3	-6.1670×10^{-5}
$S^{3/2}$	3.886640×10^{-1}	$S^{3/2}$	7.944×10^{-2}
$S^{3/2}\theta$	9.085835×10^{-3}	$S^{3/2}T$	1.6483×10^{-2}
$S^{3/2}\theta^2$	-4.619924×10^{-4}	$S^{3/2}T^2$	-5.3009×10^{-4}
p	3.186519×10^0	p	3.239908×10^0
$p\theta$	2.211176×10^{-2}	pT	1.43713×10^{-3}
$p\theta^2$	-2.984642×10^{-4}	pT^2	1.16092×10^{-4}
$p\theta^3$	1.956415×10^{-6}	pT^3	-5.77905×10^{-7}
pS	6.704388×10^{-3}	pS	2.2838×10^{-3}
$pS\theta$	-1.847318×10^{-4}	pST	-1.0981×10^{-5}
$pS\theta^2$	2.059331×10^{-7}	pST^2	-1.6078×10^{-6}
$pS^{3/2}$	1.480266×10^{-4}	$pS3/2$	1.91075×10^{-4}
p^2	2.102898×10^{-4}	p^2	8.50935×10^{-5}
$p^2\theta$	-1.202016×10^{-5}	p^2T	-6.12293×10^{-6}
$p^2\theta^2$	1.394680×10^{-7}	p^2T^2	5.2787×10^{-8}
$p^2 S$	-2.040237×10^{-6}	$p^2 S$	-9.9348×10^{-7}
$p^2 S\theta$	6.128773×10^{-8}	$p^2 ST$	2.0816×10^{-8}
$p^2 S\theta^2$	6.207323×10^{-10}	$p^2 ST^2$	9.1697×10^{-10}

Table A.1: Terms and coefficients of the bulk secant modulus $K(S, \theta, p)$ for the Jackett and Mc Dougall modified equation of state, and $\hat{K}(S, T, p)$ for the original Millero and Poisson equation of state. Salinity S is espressed in psu, pressure p in bars, and both temperatures T and θ are in degrees Celsius. Taken from Jackett and McDougall (1995).

A. Seawater equation of state

Appendix B

Conservative remapping of level-coordinate models

Hereafter is presented the procedure used by C. L. Wolfe of the Stony Brook University, School of Marine and Atmospheric Sciences, New York. This procedure considers a vertical profile where a depth value and a density value corresponds to each point.

We use conventions for variable names and grid layers similar to those used in the MITgcm (Marshall et al., 1997a,b). The vertical index k is 1-based and increases *downward*, so the cell boundaries (faces) are located at z_k^f, where $k_1^f = 0$ is the surface. There are K cells and $K+1$ faces. The distance between the faces of the kth cell faces is $\Delta z_k^f = z_k^f - z_{k+1}^f > 0$. The fraction of grid cell occupied by water is h_{ck}, where $h_{ck} = 1$ represents a cell full of water, $h_{ck} = 0$ a cell totally inside the topography and $0 < h_{ck} \leq 1$ a cell near the bottom boundary.

The value of buoyancy carried by the model is the average of b over the kth grid cell:

$$b_k = \frac{1}{h_{ck}\Delta z_k^f} \int_{z_k^f - \delta z_k^f}^{z_k^f} b \, dz \,, \tag{B.1}$$

where

$$\delta z_k^f = (\Delta z_k^f - \Delta z_{k+1}^f)h_{ck} > 0 \,. \tag{B.2}$$

Hereafter we propose the remapping technique via the piecewise parabolic method (PPM).

B. Conservative remapping of level-coordinate models

Building the interpolator

To specify uniquely a parabola to describe the variable distribution $\hat{b}_k(z)$ over the kth volume cell $z_{k+1}^f \leq z \leq z_k^f$ we need three conditions:

- the average of b over the entire cell,

- the values on the top b_{Tk},

- the value on the bottom b_{Bk}.

Using notation similar to that of Colella and Woodward (1984) and Carpenter et al. (1990), this parabola is

$$\hat{b}_k(\zeta_k) = \langle b \rangle_k + \Delta b_k \zeta_k + b_{6k} \left(\frac{1}{12} - \zeta_k^2 \right) , \tag{B.3}$$

where

$$\zeta_k = \frac{z - z_k^f}{\delta z_k^f} + \frac{1}{2} ,$$

$$\langle b \rangle_k = \frac{\Delta z_k^f}{z_k^f - z_{k+1}^f} b_k ,$$

$$\Delta b_k = b_{Tk} - b_{Bk} ,$$

$$b_{6k} = 6 \left(\langle b \rangle_k - \frac{b_{Tk} + b_{Bk}}{2} \right) .$$

Note that $-\frac{1}{2} \leq \zeta_k \leq \frac{1}{2}$. An equivalent formulation is:

$$\hat{b}_k(z) = b_{Tk} + 2 \left(b_{Bk} + 2b_{Tk} - 6 \langle b \rangle_k \right) \frac{z - z_k^f}{\delta z_k^f} + 6 \left(\frac{b_{Bk} + b_{Tk}}{2} - \langle b \rangle_k \right) \left(\frac{z - z_k^f}{\delta z_k^f} \right)^2 . \tag{B.4}$$

Unfortunately this solution is not complete, because b_{Bk} and b_{Tk} are not variables carried by the model. A commonly used second-order accurate estimate of face quantities is the average of the adjacent cell averages:

$$b_{Bk} = \frac{b_k + b_{k+1}}{2} , \tag{B.5}$$

$$b_{Tk} = \frac{b_{k-1} + b_k}{2} . \tag{B.6}$$

When these are used,

$$\Delta b_k = \frac{b_{k-1} - b_{k+1}}{2} ,$$

$$b_{6k} = 6 \left(\langle b \rangle_k - \frac{b_{k-1} + 2b_k + b_{k+1}}{4} \right) ,$$

and the resulting interpolator is a second order accurate and continuous. More information is required at the upper and lower boundaries; we assume insulating boundary conditions so that $b_{T1} = b_1$ and $b_{BK} = b_K$. In these cases,

$$
\begin{aligned}
\Delta b_1 &= \frac{b_1 - b_2}{2}, \\
\Delta b_K &= \frac{b_{K-1} - b_K}{2}, \\
b_{6,1} &= 6\left(\langle b \rangle_1 - \frac{3b_1 + b_2}{4}\right), \\
b_{6K} &= 6\left(\langle b \rangle_K - \frac{b_{K-1} + 3b_K}{4}\right).
\end{aligned}
$$

Monotonicity

It is important for many tracers that the interpolation scheme not produce values which are outside the range of the original values. In this case, if the data to be interpolated is monotonic, than the interpolator should be monotonic as well. The PPM interpolation scheme will be monotonic if the first derivative of $\hat{b}_k(\zeta_k)$ does not change sign in the interval $-\frac{1}{2} \le \zeta_k \le \frac{1}{2}$. If $\hat{b}_k(\zeta_k)$ does happen to change sign, we can adjust b_T and b_B to restore monotonicity., although we loose continuity and second-order accuracy. There are several cases to consider:

1. If $b_{6k} = 0$, the interpolator is linear and thus monotonic.

2. If $b_{6k} \ne 0$, then the $\hat{b}'_k(\zeta_k)$ changes sign at $\zeta_* = \Delta b_k / 2b_{6k}$.

   If $\zeta_* \ge 1/2$ or $\zeta_* \le 1 - /2$, the interpolator is monotonic in $-\frac{1}{2} \le \zeta_k \le \frac{1}{2}$. Otherwise,

   (a) If $\zeta_* > 0$, we can move the zero in $\hat{b}'_k(\zeta_k)$ upwards to $\zeta = 1/2$ by adjusting b_{Tk}. We find
   $$ b_{Tk} = \frac{3\langle b \rangle_k - b_{Bk}}{2}. \tag{B.7} $$

   (b) If $\zeta_* < 0$, we can move the zero in $\hat{b}'_k(\zeta_k)$ downwards to $\zeta = -1/2$ by adjusting b_{Bk}. We find
   $$ b_{Bk} = \frac{3\langle b \rangle_k - b_{Tk}}{2}. \tag{B.8} $$

   (c) If $\zeta_* = 0$, we split the difference and adjust both face values to $b_{Bk} = b_{Tk} = \langle b \rangle_k$. Then $\Delta b_k = b_{6k} = 0$ and the interpolator is constant.

Transforming into buoyancy coordinates

Once an interpolator is constructed for buoyancy b and some other field ϕ, the ϕ can be binned into to buoyancy coordinates by analytically integrating the interpolator. The buoyancy coordinate is defined by specifying the edges of the buoyancy grid

B. Conservative remapping of level-coordinate models

b_n^f, the integrated buoyancy, B_n, and the integrate of field ϕ_n in the n_{th} buoyancy bin; that is,

$$\sigma_n = \int_{b_n^f \leq b(z) \leq b_{n+1}^f} dz \,, \tag{B.9}$$

$$B_n = \int_{b_n^f \leq b(z) \leq b_{n+1}^f} b \, dz \,, \tag{B.10}$$

$$\phi_n = \int_{b_n^f \leq b(z) \leq b_{n+1}^f} \phi \, dz \,. \tag{B.11}$$

Each vertical cell k can be handled independently, so we work through a single example with fixed k and n. In terms of the interpolation variable, the three integrals are:

$$\sigma_n = \delta z_k^f \int_{b_n^f \leq b_k(\zeta) \leq b_{n+1}^f} d\zeta \,, \tag{B.12}$$

$$B_n = \delta z_k^f \int_{b_n^f \leq b_k(\zeta) \leq b_{n+1}^f} b \, d\zeta \,, \tag{B.13}$$

$$\phi_n = \delta z_k^f \int_{b_n^f \leq b_k(\zeta) \leq b_{n+1}^f} \phi \, d\zeta \,. \tag{B.14}$$

Evaluating these integrals amounts to finding the values of ζ for which $-1/2 \leq \zeta < 1/2$ and $b_n^f \leq b_k(\zeta) \leq b_{n+1}^f$.
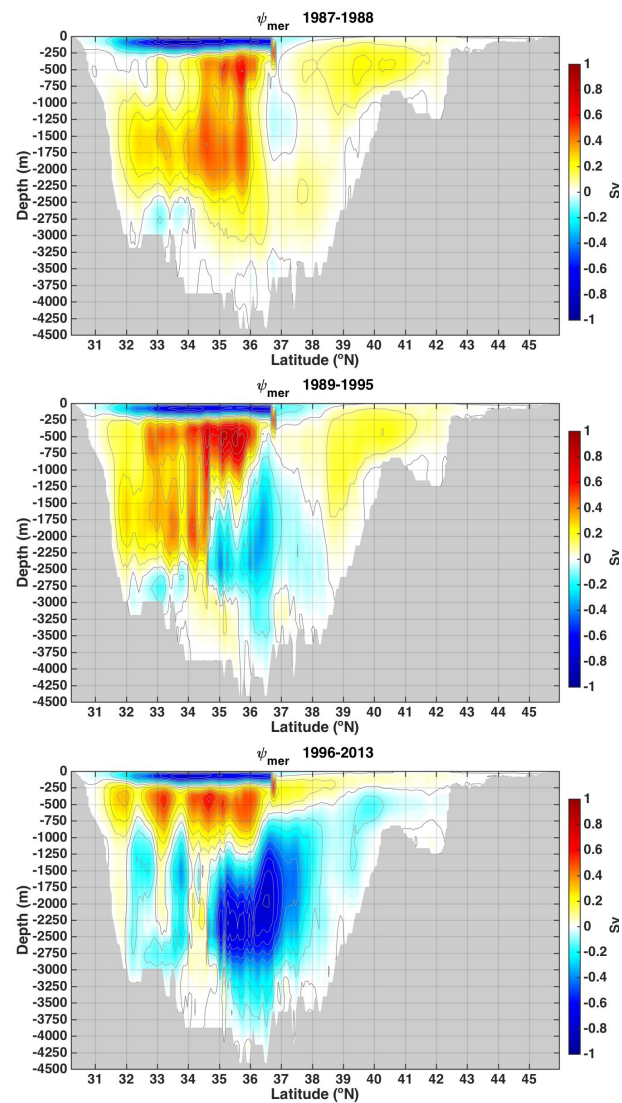
Appendix C

Figures integration

Figure C.1: Eulerian meridional streamfunction of the Adriatic, Ionian and Levantine Seas averaged over different period: (*top*) from 1987 to 1988, (*centre*) from 1989 to 1995, (*bottom*) from 1996 to 2013.
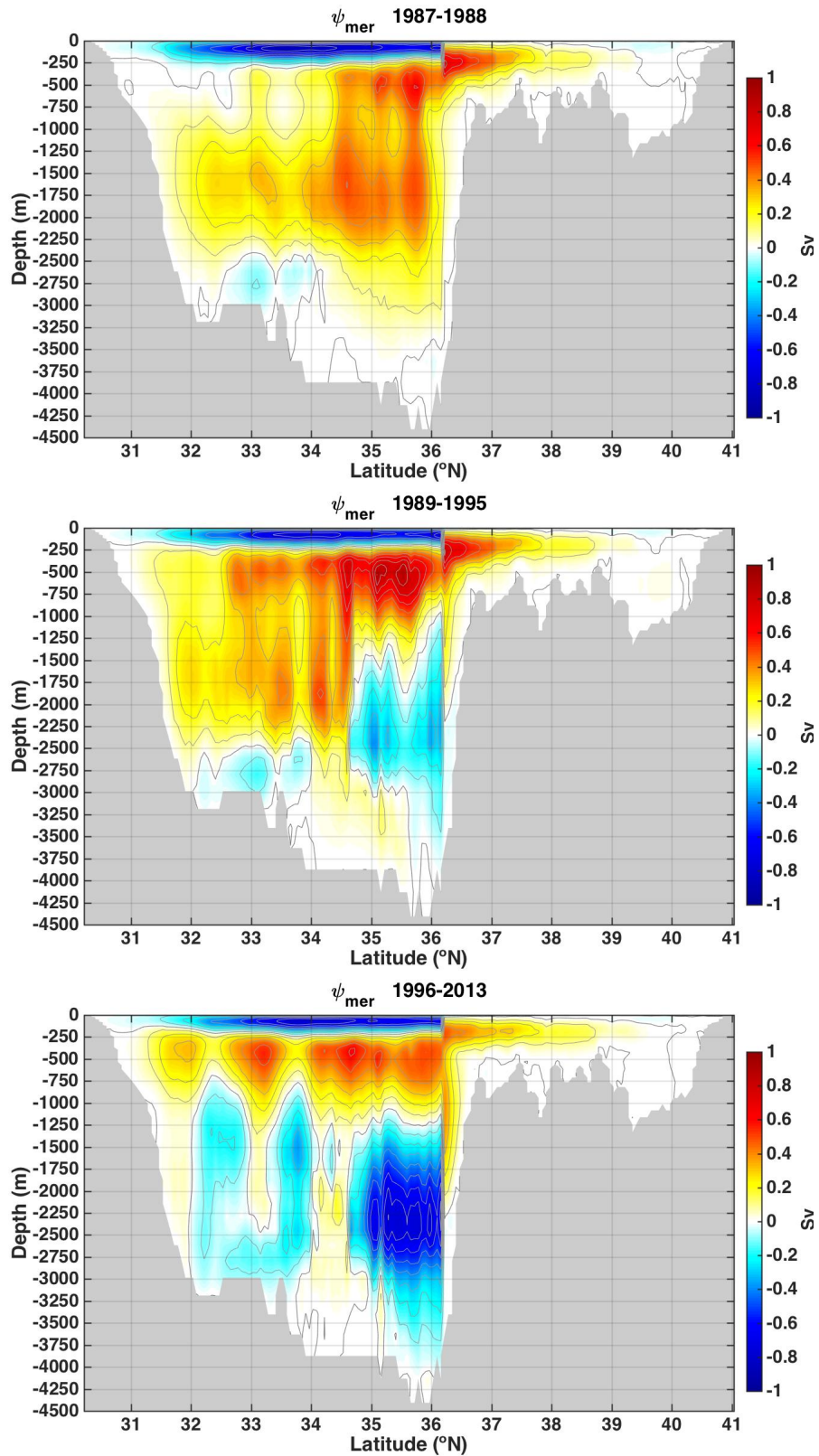
Figure C.2: Eulerian meridional streamfunction of the Aegean, southern Ionian and Levantine Seas averaged over different period: (*top*) from 1987 to 1988, (*centre*) from 1989 to 1995, (*bottom*) from 1996 to 2013.

Acknowledgments

Bibliography

Adani, M. et al. (2011). Quality Assessment of a 1985–2007 Mediterranean Sea Re-analysis. *Journal of Atmospheric and Oceanic Technology*, 28:569–589.

Alhammoud, B., Meijer, P. T., and Dijkstra, H. A. (2010). Sensitivity of Mediterranean thermohaline circulation to gateway depth: A model investigation. *Paleooceanography*, 25.

Artale, V., Astraldi, M., Buffoni, G., and Gasparini, G. P. (1994). Seasonal variability of the gyre-scale circulation in the northern Tyrrhenian Sea. *Journal of Geophysical Research*, 99:14127–14137.

Artegiani, A., Azzolini, R., and Salusti, E. (1989). On the dense water in the Adriatic Sea. *Oceanologica Acta*, 12:151–160.

Artegiani, A. et al. (1997). The Adriatic Sea general circulation. Part I: Air-sea interactions and water mass structure. *Journal of Physical Oceanography*, 27:1492–1514.

Astraldi, M., Bianchi, C. N., Gasparini, G. P., and Morri, C. (1995). Climatic fluctuations, current variability and marine species distribution: a case study in the Ligurian Sea (north-west Mediterranean). *Oceanologica Acta*, 18.

Ayoub, N., Le Traon, P.-Y., and De Mey, P. (1998). A description of the Mediterranean surface variable circulation from combined ers-1 and topex/poseidon altimetric data. *Journal of Marine Systems*, 18:3–40.

Brenner, S., Rozentraub, Z., Bishop, J., and Krom, M. (1991). The mixed layer/thermocline cycle of a persistent warm core eddy in the eastern Mediterranean. *Dynamics of Atmospheres and Oceans*, 15:455–476.

Briand, F. (2000). The Eastern Mediterranean Climatic Transient: its origin, evolution and impact on the ecosystem. *CIEMS Workshop Series, Monaco*, 10:86.

Bryden, H. L. and Stommel, H. M. (1982). Origin of the Mediterranean outflow. *Journal of Marine Research*, 40:55–71.

BIBLIOGRAPHY

Carpenter, R. L. J., Droegemeier, K. K., Woodward, P. R., and Hane, C. E. (1990). Application of the piecewise parabolic method (PPM) to meteorological modeling. *Monthly Weather Review*, 118:586–612.

Castellari, S., Pinardi, N., and Leaman, K. (1998). A model study of air-sea interactions in the Mediterranean Sea. *Journal of Marine Sciences*, 18:89–114.

Castellari, S., Pinardi, N., and Leaman, K. (2000). Simulation of Water Mass Formation Processes in the Mediterranean Sea: influence of the time frequency of the atmospheric forcing. *Journal of Geophysical Research*, 105:24157–24181.

Cessi, P. and Pinardi, N. (2014). Energetics of the semienclosed basins with two-layer flows at the strait. *Journal of Physical Oceanography*, 44:967–979.

Cessi, P. and Wolfe, C. (2009). Eddy-Driven Buoyancy Gradients on Eastern Boundaries and Their Role in the Thermocline. *Journal of Physical Oceanography*, 39:1595–1614.

Cessi, P. and Wolfe, C. (2013). Adiabatic Eastern Boundary Currents. *Journal of Physical Oceanography*, 43:1127–1149.

Colella, P. and Woodward, P. R. (1984). The piecewise parabolic method (PPM) for gas-dynamical simulations. *Journal of Computational Physics*, 54:174–201.

Dee, D. P. et al. (2011). The ERA-Interim reanalysis: configuration and performance of the data assimilation system. *Quarterly Journal of the Royal Meteorological Society*, 137.

Demirov, E. and Pinardi, N. (2002). Simulation of the Mediterranean Sea circulation from 1979 to 1993: Part i. The interannual variability. *Journal of Marine Systems*, 33-34:23–50.

Demirov, E. and Pinardi, N. (2007). On the relationship between the water mass pathways and eddy variability in the Western Mediterranean Sea. *Journal of Geophysical Research*, 112.

Dobricic, S. and Pinardi, N. (2008). An oceanographic three-dimensional variational data assimilation scheme. *Ocean Modeling*, 22:89–105.

Dobricic, S., Pinardi, N., Adani, M., Bonazzi, A., Fratianni, C., and Tonani, M. (2005). Mediterranean Forecasting System: An improved assimilation scheme for sea-level anomaly and its validation. *Quarterly Journal of the Royal Meteorological Society*, 31:3627–3642.

Fu, L.-L., Christensen, E. J., et al. (1994). TOPEX/POSEIDON mission overview. *Journal of Geophysical Research*, 99:24369–24381.

Garrett, C., Outerbridge, R., and Thompson, K. (1993). Interannual variability in meterrancan heat and buoyancy fluxes. *Journal of Climate*, 6:900–910.

Gascard, S. C. J. (1978). Mediterranean deep water formation, baroclinic eddies and ocean eddies. *Oceanologica Acta*, 1:313–315.

Gertman, I., Pinardi, N., Popov, Y., and Hecht, A. (2006). Aegean Sea Water Masses during the Early Stages of the Eastern Mediterranean Climatic Transient (1988–90). *Journal of Physical Oceanography*, 36:1841–1859.

Gleizon, P., Chabert D'Hiéres, G., and Renouard, D. (1996). Experimental study of the Alboran Sea gyres. *Oceanologica Acta*, 12:499–511.

Grandi, A., Drudi, M., Fratianni, C., Girardi, G., Simoncelli, S., and Tonani, M. (2015). Product user manual for Mediterranean Sea physical reanalysis product. *Copernicus Marine Environment Monitoring Service*.

Hallberg, R. (2013). Using a resolution function to regulate parameterizations of oceanic mesoscale eddy effects. *Ocean Modeling*, 72:92–103.

Hecht, A. (1992). Abrupt changes in the characteristics of Atlantic and Levantine intermediate waters in the Southeastern Levantine basin. *Oceanologica Acta*, 15:25–42.

Hecht, A. Z., Pinardi, N., and Robinson, A. R. (1988). Currents, water masses, eddies and jets in the Mediterranean Levantine Basin. *Journal of Physical Oceanography*, 8:1320–1353.

Jackett, D. R. and McDougall, T. J. (1995). Minimal Adjustment of Hydrographic Profiles to Achieve Static Stability. *Journal of Atmospheric and Oceanic Technology*, 12:381–389.

Klein, B., Roether, G., Manca, B. B., Bregant, D., Beitzel, V., Kovancevic, V., and Luchetta, A. (1999). The large deep water transient in the eastern Mediterranean. *Deep Sea Research, Part 1*, 46:371.414.

Klein, B., Roether, W., Civitarese, G., Gačić, M., Manca, B. B., and d'Alcala, M. R. (2000). Is the Adriatic returning to dominate the production of Eastern Mediterranean Deep Water? *Geophysical Research Letters*, 27:3377–3380.

Korres, G., Pinardi, N., and Lascaratos, A. (2000). The ocean response to low-frequency interannual atmospheric variability in the Mediterranean Sea. Part I: sensitivity experiments and energy analysis. *Journal of Climate*, 13:705–731.

Larnicol, G., Ayoub, N., and Le Traon, P. Y. (2002). Major changes in Mediterranean Sea level variability from 7 years of TOPEX/Poseidon and ERS-1/2 data. *Journal of Marine Systems*, 33-34:63–89.

Lascaratos, A. (1993). Estimation of deep and intermediate water mass formation rates in the Mediterranean Sea. *Deep Sea Research Part II: Topical Studies in Oceanography*, 40:1327–1332.

Lascaratos, A. and Nittis, K. (1998). A high-resolution three-dimensional numerical study of intermediate water formation in the Levantine Sea. *Journal of Geophysical Research*, 103:18497–18511.

Lascaratos, A., Roether, W., Nittis, K., and Klein, B. (1999). Recent changes in deep water formation and spreading in the Mediterranean Sea: A review. *Progress in Oceanography*, 44:5–36.

Leaman, K. d. and Schott, F. A. (1991). Hydrographic structure of the convective regime in the Gulf of Lions: Winter 1987. *Geophysical Reseach Ogeanography*, 21:575–598.

Lenderink, G. and Haarsma, R. J. (1994). Variability and multiple equilibra of the thermohaline circulation associated with deep-water formation. *Journal of Physical Oceanography*, 24:1480–1493.

Lyard, F., Lefevre, F., Letellier, T., and Francis, O. (2006). Modelling the global ocean tides: modern insights from FES2004. *Ocean Dynamics*, 56:394–415.

Madec, G., Lott, F., Delecluse, P., and Crepon, M. (1996). Large scale preconditioning of deep-water formation in the northwestern Mediterranean Sea. *Physical Oceanography*, 26:1393–1408.

Madec, G. and the NEMO team (2012). *NEMO ocean engine*, 3.4 edition.

Manca, B. B., Budillon, G., Scarazzato, P., and Ursella, L. (2003). Evolution of dynamics in the eastern Mediterranean affecting water mass structures and properties in the Ionian and Adriatic Sea. *Journal of Geophysical Research*, 108(C9).

Manca, B. B., Kovancevic, V., et al. (2002). Dense water formation in the Southern Adriatic Sea and spreading into the Ionian Sea in the period 1997–1999. *Journal of Marine Systems*, 33-34:1674–1690.

Mariotti, A., Struglia, M. V., Zeng, N., and Lau, K.-M. (2001). The Hydrological Cycle in the Mediterranean Region and Implications for the Water Budget of the Mediterranean Sea. *Journal of Climate*, 15:133–154.

Marshall, J., Adcroft, A., Hill, C., Perelman, L., and Heisey, C. (1997a). A finite-volume, incompressible Navier-Stokes model for studies of the ocean on parallel computers. *Journal of Geophysical Research*, 102:5753–5766.

Marshall, J., Hill, C., Perelman, L., and Adcroft, A. (1997b). Hydrostatic, quasi-hydrostatic, and nonhydrostatic ocean modeling. *Journal of Geophysical Research*, 102:5733–5752.

Marshall, J. and Schott, F. (1999). Open-ocean convection: observations, theory,and models. *Reviews of Goephysic*, 37:1–64.

McDougall, T. J. (1987). Neutral Surfaces. *Journal of Physical Oceanography*, 17:1950–1964.

Merckelbach, L., Smeed, D., and Griffiths, G. (2010). Vertical Water Velocities from Underwater Gliders. *Journal of Atmospheric and Oceanic Technology*, 27:547–563.

Mesinger, F. and Arakawa, A. (1976). Numerical methods used in atmospheric models, volume 1. *Global Atmospheric Research Program World Meteorological Organization*, 1.

Millero, F. J. and Poisson, A. (1981). International one-atmosphere equation of state of seawater. *Deep Sea Research*, 28A(6):625–629.

Molcard, A., Pinardi, N., Iskandaranic, M., and Haidvogeld, D. (2002). Wind driven general circulation of the Mediterranean Sea simulated with spectral element ocean model. *Dynamics of Atmospheres and Oceans*, 35:97–130.

Morcos, S. A. (1972). Sources of Mediterranean Intermediate Water in the Levantine Sea. *Studies in Physical Oceanography: A Tribute to G. Wüst in his 80th birthday*, 2:185–206.

Nittis, K. and Lascaratos, A. (1998). Diagnostic and prognostic numerical studies of LIW formation. *Journal of Marine Systems*, 18:179–195.

Ovchinnikov, I. M. (1984). The formation of intermediate water in the Mediterranean. *Oceanology*, 24:168–173.

Pinardi, N. and Masetti, E. (2000). Variability of the large scale general circulation of the Mediterranean Sea from observations and modelling: a review. *Palaeogeography, Palaeoclimatology, Palaeoecology*, 15:153–173.

Pinardi, N. and Navarra, A. (1993). Baroclinic wind adjustment processes in the Mediterranean Sea. *Deep Sea Research Part II: Topical Studies in Oceanography*, 40:1299–1326.

Pinardi, N., Zavatarelli, M., Adani, M., Coppini, G., Fratianni, C., Oddo, P., Simoncelli, S., Tonani, M., Lyubartsev, V., Dobricic, S., and Bonaduce, A. (2015). Mediterranean Sea large-scale low-frequency ocean variability and water mass formation rates from 1987 to 2007: A retrospective analysis. *Progress in Oceanograpgy*, 132:318–332.

Pisacane, G., Artale, V., Calmanti, S., and Rupolo, V. (2006). Decadal oscillations in the Mediterranean Sea: a result of the overturning circulation variability in the eastern basin? *Climate Research*, 31:257–271.

Poulain, P.-M., Menna, M., and Mauri, E. (2012). Surface geostrophic circulation of the Mediterranean Sea derived from drifter and satellite altimeter data. *Journal of Physical Oceanography*, 42:973–990.

Rahmstorf, S. (1996). On the freshwater forcing and transport of the Atlantic thermohaline circulation. *Climate Dynamics*, 12:799–811.

Roether, W., Manca, B. B., Klein, B., Bregant, D., et al. (1996). Recent changes in the Eastern Mediterranean Deep Waters. *Science*, 271:333–335.

Roether, W. and Schlitzer, R. (1991). Eastern Mediterranean deep water renewal on the basis of chlorofluoromethane and tritium data. *Dynamics of Atmosphere and Oceans*, 15:333–354.

Rohling, E. J. (1996). Review and new aspects concerning the formation of eastern Mediterranean sapropels. *Marine Geology*, 122:1–28.

Schott, F. and Leaman, K. D. (1991). Observation with moored acoustic Doppler current profilers in the convection regime in the Golfe du Lion. *Journal of Physical Oceanography*, 21:558–574.

Simoncelli, S., Bonaduce, A., and Tonani, M. (2015). Quality information document for Mediterranean Sea physical reanalysis product. *Copernicus Marine Environment Monitoring Service*.

Speich, S., Madec, G., and Crépon, M. (1996). A strait outflow circulation process study: the case of the Alboran Sea. *Journal of Physical Oceanography*, 26:320–340.

Stammer, D., Wunsch, C., Giering, R., et al. (1991). Global ocean circulation during 1992-1997, estimated from ocean observations and a general circulation model. *Journal of Geophysical Research*, 107:1–27.

Swallow, J. C. and Caston, G. F. (1973). The preconditioning phase of MEDOC 1969, 1, Observations. *Deep Sea Research*, 20:429–448.

Testor, P. and Gascard, J. C. (2006). Post-convection spreading phase in the Northwestern Mediterranean Sea. *Deep Sea Research Part I: Oceanographic Research Papers*, 53:869–893.

Theocharis, A., Klein, B., Nittis, K., and Roether, W. (2002). Evolution and status of the Eastern Mediterranean Transient. *Journal of Marine Systems*, 33-34:91–116.

Theocharis, A., Nittis, K., Kontoyiannis, H., Papageorggiou, E., and Balopoulos, E. (1999). Climatic changes inthe Aegean Sea influence the Eastern Mediterranean thermohaline circulation (1986-1997). *Geophysical Research Letters*, 26:1617–1620.

Tonani, M., Pinardi, N., Fratianni, C., Pistoia, J., Dobricic, S., Pensieri, S., de Alfonso, M., and Nittis, K. (2009). Mediterranean Forecasting System: forecast and analysis assessment through skill scores. *Ocean Science.*

Trotta, F., Fenu, E., Zavatarelli, M., and Giacomelli, L. (2015). Redazione della documentazione tecnica e del manuale d'uso del sistema rilocabile basato sul modello NEMO e interfaccia grafica. *Dipartimento di Fisica e Astronomia dell'Università di Bologna Laboratorio SiNCEM.*

Tziperman, E. and Malanotte-Rizzoli, P. (1991). The climatological circulation of the Mediterranean Sea. *Journal of Marine Research*, 49:411–434.

Vallis, G. K. (2006). Atmospheric and Oceanic Fluid Dynamics. *Cambridge University Press.*

Welander, P. (1982). A simple heat seal oscillator. *Dynamics of Atmosphere and Oceans*, 6:233–242.

Wolfe, C. and Cessi, P. (2010). What Sets the Strength of the Middepth Stratification and Overturning Circulation in Eddying Ocean Models? *Journal of Physical Oceanography*, 40:1520–1538.

Wu, P. and Haines, K. (1996). Modelling the dispersal of Levantine Intermediate Water and its role in Mediterranean deep water formation. *Journal of Geophysical Research*, 101:6591–6607.

Wüst, G. (1961). On the Vertical Circulation of theMediterranean Sea. *Journal of Geophysical Research*, 66:3261–3271.

Yari, S., Kovacevic, V., et al. (2012). Direct estimate of water, heat, and salt transport through the Strait of Otranto. *Journal of Geophisical Research*, 117.

Yin, F. and Sarachik, E. (1995). Interdecadal thermohaline oscillations in a sector ocean general circulation model: advective and convective processes. *Journal of Physical Oceanography*, 25:2465–2484.

Young, W. R. (2012). An Exact Thickness-Weighted Average Formulation of the Boussinesq Equations. *Journal of Physical Oceanography*, 42:692–707.

Zavatarelli, M. and Mellor, G. (1995). A numerical study of the Mediterranean Sea circulation. *Journal of Physical Oceanography*, 25:1348–1414.